Design and implementation of micro-structures with refractive index contrast for optical interconnects and sensing applications

by

Muhammad Umar Khan

111220485

Thesis submitted to

The National University of Ireland, Cork

for the degree of

Doctor of Philosophy

Tyndall National Institute

The Department of Electrical and Electronics Engineering

University College Cork

Supervisors: Dr. Brian Corbett

Prof. Peter Parbrook

Head of Department/School: Prof. Nabeel A. Riza

Table of Contents

List of Figures

List of Tables

List of Acronyms

WG	Waveguide
PhC	Photonic Crystals
1D	One Dimensional
2D	Two Dimensional
3D	Three Dimensional
PBG	Photonic Band-gap
TE	Transverse Electric
TM	Transverse Magnetic
FDTD	Finite Difference Time Domain
FCC	Face Centred Cubic
RFCC	Random Face centred Cubic
HCP	Hexagonally Closed Packed
FWHM	Full Width Half Maximum
BSW	Bloch Surface Wave
BSSW	Bloch Sub Surface Wave
IPA	Isopropanol Alcohol
nm	nanometre
RIU	Refractive Index Unit
PCB	Printed Circuit Board
OPCB	Optical Printed Circuit Board
ORMOCER	Organically Modified Ceramics
UV	Ultraviolet
IR	Infrared

List of Acronyms

NIL	Nano Imprint Lithography
MMI	Multimode Interference
DC	Directional Coupler
SEW	Surface Electromagnetic Waves
Si	Silicon
SPR	Surface Plasmon Resonance
SOI	Silicon on Insulator
K-R	Kretschmann-Raether
LoD	Limit of detection
RWG	Resonant Waveguide Grating
TIR	Total Internal Reflection
AFM	Atomic Force Microscopy
SEM	Scanning Electron Microscope
DI	De-ionised
PMMA	Poly(methyl methacrylate)
dB	decibel
MFD	Mode Field Diameter
VCSEL	Vertical Cavity Surface Emitting Laser
IL	Insertion Loss
OSA	Optical Spectrum Analyser
TLS	Tuneable Laser Source
FIB	Focussed Ion Milling
TEOS	Tetra-ethyl Orthosilicate

Declaration

I, Muhammad Umar Khan, certify that this thesis is my own work and has not been submitted for another degree at University College Cork or elsewhere.

_____

Muhammad Umar Khan

List of Publications

- **Muhammad Umar Khan**, John Justice, Jarno Petäjä, Tia Korhonen, Arjen Boersma, Sjoukje Wiegersma, Mikko Karppinen, and Brian Corbett, "Multi-level single mode 2D polymer waveguide optical interconnects using nano-imprint lithography," Opt. Express 23, 14630-14639 (2015).
- **Muhammad Umar Khan** and Brian Corbett, "Bloch surface wave structures for high sensitivity detection and compact waveguiding" Sci. Technol. Adv. Mater. 17, 398-409 (2016).
- **Muhammad Umar Khan**, John Justice, Arjen Boersma, Maurice Mourad, Renz van Ee, Alfons van Blaaderen, Judith Wijnhoven and Brian Corbett, "Development of photonic crystal structures for on-board optical communication," Proc. SPIE 9127, Photonic Crystal Materials and Devices XI, 912705 (May 2, 2014); doi:10.1117/12.2052214.
- Jacek Gosciniak, John Justice, **Umar Khan** and Brian Corbett, "Study of TiN nanodisks with regard to application for Heat-Assisted Magnetic Recording," MRS Advances, available on CJO2016. doi:10.1557/adv.2016.22.
- John Justice, **Umar Khan**, Tia Korhonen, Arjen Boersma, Sjoukje Wiegersma, Mikko Karppinen, Brian Corbett, "Design, fabrication, and characterisation of nano-imprinted single-mode waveguide structures for intra-chip optical communications," Proc. SPIE9368, Optical Interconnects XV, 936834 (2015); doi:10.1117/12.2078974.
- Mikko Karppinen, Noora Salminen, Tia Korhonen, Teemu Alajoki, Erwin Bosman, Geert Van Steenberge, John Justice, **Umar Khan**, Brian Corbett, Arjen Boersma, "Optical coupling structure made by imprinting between single-mode polymer waveguide and embedded VCSEL," Proc. SPIE9368, Optical Interconnects XV, 936817 (2015);doi: 10.1117/12.2082935.
- Jacek Gosciniak, John Justice, **Umar Khan** and Brian Corbett, "Study of high order plasmonic modes on ceramic nanodisks," Optics Express January 2017.
- **Muhammad Umar Khan**, John Justice and Brian Corbett, "Waveguide coupled BSW resonances," Optics Express (In preparation).

List of Publications

- **Muhammad Umar Khan**, John Justice and Brian Corbett, “Resonant waveguides, the future in on-chip sensing,” Conference paper (In preparation).
- **Muhammad Umar Khan**, John Justice, Pierre Lovera and Brian Corbett, “High sensitivity silicon-based Bloch surface wave sensor,” Conference paper (In preparation).

To my parents and family

Abstract

Periodic structures have always been part of our lives. With the development of human understanding it was realised that natural opals, butterfly wings and bird feathers which have been keenly observed for generations are actually naturally occurring photonic crystals (structures with periodic modulation of the refractive index). In this work, I have investigated the scientific use of refractive index contrast and nanometer scale periodicity for applications in optical interconnects and surface plasmon resonance like dielectric optical sensors.

One dimensional photonic crystals can be engineered to sustain a surface wave called as Bloch surface wave (BSW). A BSW based label-free sensor is designed and implemented using only a pair of high (Si, 70 nm) and low (SiO_2, 676 nm) index materials in contrast to multiple pairs used previously. The demonstrated bulk sensitivity (900 nm/RIU) for a single pair sensor is comparable to the multi-pair sensors using the prism based Kretschmann-Raether configuration. The demonstrated sensor using only a single pair of dielectric layers is the dielectric counterpart of the surface plasmon resonance based sensors using gold on dielectric. A SU8 waveguide is cladded by the above mentioned thicknesses of silicon and silica to demonstrate on-chip sensing using the end-fire coupling for the first time. The demonstrated on-chip sensing platform is simple to fabricate and is believed to lay the foundation of a cheap and sensitive integrated sensing system.

Organically Modified Ceramic (ORMOCER) based single-mode waveguides and passive devices for both single and multi-level centimetre sized optical boards using nano-imprint lithography (NIL) are demonstrated with waveguide loss less than 0.2 dB/cm. An ‘optical via’ for vertical coupling of light from one optical plane to another is designed and implemented using NIL. A novel 1 x 4 2D optical port is designed and implemented for the first time to spatially distribute the input light over different optical planes. Polymer waveguides inherently have smaller refractive index contrast between core and cladding requiring a bending radius of atleast 8mm for lossless communication. Sharp in-plane bends are demonstrated for the first time by integrating core-shell colloidal crystals with these polymer waveguides. The demonstrated efficiency for in-plane bends is poor which will improve with optimisation of the colloidal crystal fabrication. Finally, inverted opal photonic crystals are used as under-cladding for the waveguide core to demonstrate effectively an air suspended polymer waveguide that can be used for sensing

applications. Component density on optical printed circuit boards can be increased using the demonstrated sharp in-plane bends once better stacking is achieved.

CHAPTER 1

Introduction

1 Introduction

Light covers distance of around 150 million kilometres from surface of the sun to the earth in almost 8 minutes and 20 seconds travelling at a speed of 300,000 kilometres/second. This is the highest attainable speed in this universe and is named as the vacuum speed of light. The speed of the light in a medium is less than the vacuum speed and this reduction in the speed is determined by the refractive index (n) of that medium which is defined as:

$$\boldsymbol{n = \frac{c}{v}} \qquad \textbf{1-1}$$

where c is the speed of light in vacuum and v is the phase velocity of light in that medium. Water has a refractive index of 1.33 so light travels 1.33 times slower in water than in free space. So, it would have taken light 11 minutes and 5 seconds to reach the earth if water was present between the sun and our planet. The refractive index of a medium not only defines the speed of light inside the medium but also defines the bending of light while entering or leaving the medium. Bending of light while entering or leaving a medium is defined by the refractive index values of the material and the environment. So, refractive index contrast can be used to manipulate and control the path of the light. A high index channel with low index surroundings can be used to guide the light along the desired path. The high index channel guiding the light is called a waveguide. The refractive index of a medium itself can also be modulated to control the path of light inside the medium. A medium having periodic modulation of refractive index is called a photonic crystal.

In this thesis, the use of refractive index modulation and its contrast with the neighbouring media is studied. Different applications like sensing, guiding and manipulation of light are studied for different engineered structures having refractive index contrast and periodic modulation. Periodic modulation of refractive index in one dimension is used to design and realise Bloch surface wave based sensors. High index channels are used to guide light and to couple it both horizontally and vertically. Three dimensional modulation of refractive index being the most difficult thing to attain is studied at the end for bending of light in the guiding waveguides.

This chapter provides a general overview of the optical waveguides and the photonic crystals and explains their basic working principles. An outline of the thesis is provided at the end of this chapter.

1.1 Optical Waveguides

A high index channel used for transportation of electromagnetic waves in the optical spectrum is called an optical waveguide. An optical waveguide is the fundamental element of an optical integrated circuit as are the metallic tracks for an electrical integrated circuit. The simplest structure of a dielectric waveguide consists of a horizontally extended high-index optical medium, called the core, which is surrounded by low-index media, called the cladding. This kind of waveguide is called a planar waveguide and a guided optical wave propagates in the waveguide along its horizontal direction confined only in the vertical direction by the cladding. The light is not confined in the horizontal direction for this planar waveguide. The waveguides which confine the light in both horizontal and vertical directions are called non-planar waveguides. Planar waveguides being the simplest to understand and fabricate are discussed below to explain the types of optical modes that can propagate. An optical mode is the spatial distribution of optical energy in one or more dimensions that remains constant in time.

A three-layer planar waveguiding structure having a high index core of index n_2 surrounded by indices n_3 and n_1 from bottom and top respectively is shown in Figure 1-1 below. The layers are considered to be infinite in the y and z (horizontal) directions. The cladding layers 1 and 3 are also considered to be semi-infinite in the x (vertical) direction. This kind of waveguide is called an asymmetric waveguide because the substrate and upper cladding have different refractive indices. A waveguide having an upper cladding with index same as substrate is called symmetric waveguide. The asymmetry of the waveguide can be measured using the equations below.

$$a_E = \frac{n_3^2 - n_1^2}{n_2^2 - n_3^2} \qquad \textbf{1-2}$$

$$a_M = \frac{n_2^4}{n_1^4}\frac{n_3^2 - n_1^2}{n_2^2 - n_3^2} \qquad \textbf{1-3}$$

where a_E and a_M represent the asymmetries for TE and TM polarized light respectively.

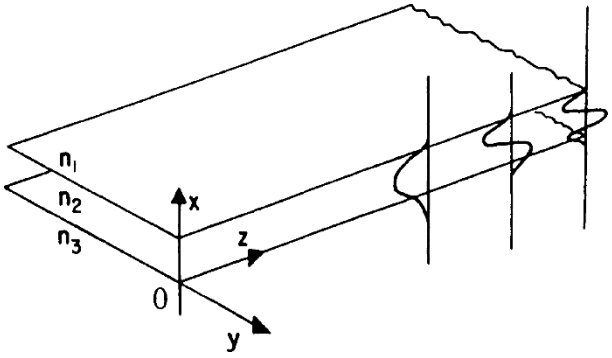

Figure 1-1: Sketch showing an asymmetric planar waveguide having a core of index n_2 on a substrate of index n_3. A layer of index n_1 (air here) acts as upper cladding for the slab waveguide. The light is confined in the vertical direction by the substrate and the air and travels in the z direction. Three possibilities of the modes are also shown. This diagram is copied from [1].

The propagation direction of the guided light is considered to be the z direction. The mode of a planar waveguide inside each layer (n_1, n_2 or n_3) can be obtained by using the equation below.

$$\frac{\partial^2 E(x,y)}{\partial^2 x} + (\boldsymbol{k^2 n_i^2 - \beta^2})\, \boldsymbol{E(x,y)} = \mathbf{0} \qquad \textbf{1-4}$$

where E(x, y) is one of the Cartesian components of E(x, y), k is the wave-vector defined as $2\pi/\lambda$, β is the propagation constant defined as $n_{eff}k$ and n_i represents the refractive index of the respective layer. The solutions of this equation can either be sinusoidal or exponential functions of x in each of the regions, depending whether $(k^2 n_i^2 - \beta^2)$ is greater than or less than zero. As the fields should be continuous at the interfaces so E(x, y) and ∂E(x, y)/∂x must be continuous at the interface between layers.

The mode shapes of the travelling light as a function of the propagation constant β are explained for a constant frequency ω. The refractive indices of the planar waveguide are considered as $n_2 > n_3 > n_1$ to correspond to a waveguiding layer of index n_2 formed on a substrate with smaller index n_3, covered by air of index n_1 from top. When $\beta > kn_2$, the effective index of the mode will be larger than the core refractive index so the function $E(x)$ must be exponential in all three regions and only the mode shape shown in Figure 1-2(a) could satisfy the boundary conditions of $E(x)$ and $\partial E(x)/\partial x$ being continuous at the interfaces. This mode is not physically realisable because the field increases unboundedly

in both Layers 1 and 3 which is impossible as the energy will be infinite for this case. When values of β *are* between kn_2 and kn_3, the effective index of the mode is less than the index of core but larger than the substrate so light will be confined inside the core. Modes (b) and (c) are well confined guided modes, generally referred to as the zero and first order transverse electric modes, TE_0 and TE_1. These modes are the real waveguide supported modes with exponential decaying of the guided light outside the core. If β is greater than kn_1 but less than kn_3, the light will be concentrating inside the substrate as shown in (d). This type of mode, which is confined at the air interface but sinusoidally varying at the substrate, is often called a substrate radiation mode. The light can travel inside the substrate but because it is continually losing energy from the core region of the waveguide so it cannot propagate for very long distances. These modes are not desired for transmitting purposes but are very useful for coupler applications such as the tapered coupler. If β is less than kn_1 the solution for $E(x)$ is oscillatory in all three regions of the waveguide structure. The energy resides in the air so this kind of mode is not a guided mode because the energy is free to spread out of the waveguiding core region. These modes are called as air radiation modes. Small portion of energy is radiated to the substrate also.

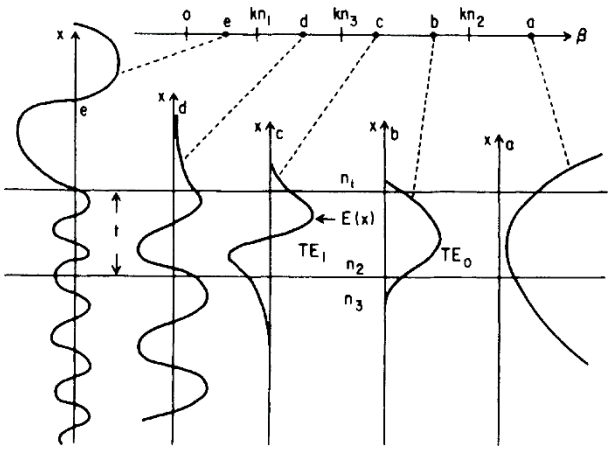

Figure 1-2: The sketch showing the possible modes for the planar waveguide structure having $n_2>n_3>n_1$. Only TE_0 and TE_1 are the waveguide guided modes having an effective index in between indices of waveguide core and the substrate. The sketch is copied from [1].

Planar waveguides are easy to fabricate but do not confine the light in the horizontal direction which is required for most of the real life devices. So, most waveguides used in device applications are non-planar waveguides. For a non-planar waveguide, the index profile n(x, y) is a function of both x and y. There are many different types of non-planar waveguides that are differentiated by the distinctive features of their index profiles. One important group of non-planar waveguides is the channel waveguides. Different kinds of the channel waveguides are shown in the Figure 1-3 below. The indices of the waveguide, substrate and the upper cladding are marked as n_1, n_2 and n_3 respectively.

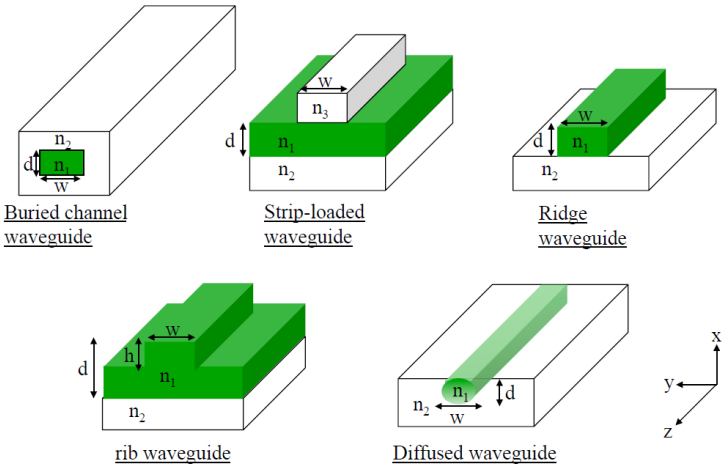

Figure 1-3: A diagram showing different type of non-planar channel waveguides. Only diffused waveguide is not a rectangular waveguide.

The buried channel waveguide is formed with a high-index waveguiding core buried in a low-index surrounding medium. The waveguiding core can have any cross-sectional geometry. A strip-loaded waveguide is formed by loading a planar waveguide, which already provides optical confinement in the x direction, with a dielectric strip of index $n_3<n_1$ or a metal strip to facilitate optical confinement in the y direction. The waveguiding core of a strip waveguide is the n_1 region under the loading strip, with its thickness d determined by the thickness of the n_1 layer and its width w defined by the width of the loading strip. A ridge waveguide has a structure that looks like a strip waveguide, but the strip on top of its planar structure has a high index and is actually the waveguiding core. A ridge waveguide has strong optical confinement because it is surrounded on three sides by low-index cladding. A rib waveguide has a structure similar to that of a strip or ridge waveguide, but the strip has the same index as the high index planar layer beneath it and

is part of the waveguiding core. These four types of waveguides are usually termed rectangular waveguides. A diffused waveguide is formed by creating a high-index region in a substrate through diffusion of dopants and is not a rectangular waveguide.

To conclude the waveguide section, the concept of optical modes in a waveguiding structure is discussed. It is mentioned that non-planar waveguides capable of confining light in all three directions are mostly used in devices. Plenty of waveguide based applications ranging from sensors [2, 3], modulators [4, 5], and other devices [6, 7] have already been demonstrated. Polymer waveguides will be discussed in detail in chapter **Error! Reference source not found.**.

1.2 Photonic Crystals

Photonic crystals (PhC) are structures with a periodic modulation of the refractive index on the order of the wavelength of the light. Periodic crystals are fabricated artificially in the labs and are found in the nature as well. The opals, butterfly wings and colourful bird feathers which have been keenly observed for generations are actually naturally found photonic crystal structures. The focus of this section is to explain different types and working of the artificial photonic crystals.

The periodicity of the refractive index results in a photonic band gap which is the most important trait of PhC and determines their practical significance. The photonic band gap (PBG) is the range of frequencies or energies for which propagation of light is prohibited inside the photonic crystal. So, if a correctly polarised light with frequency falling within the band-gap of the photonic crystal is incident, it will be reflected. This photonic band-gap concept is very similar to the well-known electronic band-gap used in solid-state physics. The regular arrangement of the atoms in a lattice results in periodicity of the electronic potential in semiconductors giving rise to the electronic band-gaps. These electronic band-gaps are forbidden energy bands for electrons. Similarly, the periodicity of the refractive index gives rise to the photonic band gap, forbidden energy bands for photons.

The periodicity of the photonic crystal can be disturbed by introducing a defect inside the crystal. The effect of such a defect is similar to the defect in a crystalline structure of

a semiconductor. Introduction of the defect results in appearing of new eigen-states inside the band-gap with energy corresponding to the eigen-frequency of the introduced defect. The light with frequency matching the frequency of the defect will propagate inside the structure.

Depending on geometry of the structure, photonic crystals can be divided into three broad categories, namely one-dimensional (1D), two-dimensional (2D) and three-dimensional (3D) structures.

1.2.1 One Dimensional Photonic Crystals (1D-PhC)

In a 1D PhC, the periodic modulation of the refractive index occurs in one direction only with a uniform structure in the remaining directions. A Bragg grating is an example of a 1D photonic crystal. Periodic modulation of the refractive index in a Bragg grating is made by repeating high and low index dielectric layers in a periodic manner. The refractive index contrast, thicknesses and the number of layers determine the behaviour of a dielectric stack. The percentage of light reflecting form an interface between two dielectrics at normal incidence for a plane wave is given by Fresnel formula

$$\boldsymbol{R} = \left(\frac{n_2 - n_1}{n_2 + n_1}\right)^2 \qquad \textbf{1-5}$$

where n_1 and n_2 are the refractive index values of the high and low index materials. This shows that a larger refractive index contrast will result in higher reflections from each interface requiring lesser number of pairs for complete reflection of the incident light. A highly reflective structure can be designed by setting optical thickness of each layer equal to one fourth of the reflecting wavelength ($\lambda/4n$). This type of stack is called a quarter wave stack. The working of a highly reflective stack is explained in Figure 1-4. The incident light is reflected back from each dielectric interface. The phase of the reflected lights should be $m*2\pi$ (m = integer) out of phase to interfere constructively. The light goes through a π phase shift on reflection from low to high index interface. No phase shift is experienced for reflection from high to low index interface. The phase shifts are marked with the respective interface in the stack. Optical thickness of each layer is set as one quarter of the wavelength to achieve a phase shift of π for round trip of light through the layer. It can be noticed that the first reflection in the sketch has a phase shift of π due

to reflection from air to the n_2 interface. The second reflection also has a shift of π. This phase shift for second reflection is due to the round trip of the light through the first dielectric layer. It can be noticed that third and fourth reflections from the stack are 2π out of phase from the first two reflections. So, reflections from the quarter wave stack interfere constructively and result in high reflections from the stack. Anti-reflection stacks can also be designed by making the reflection interfere destructively.

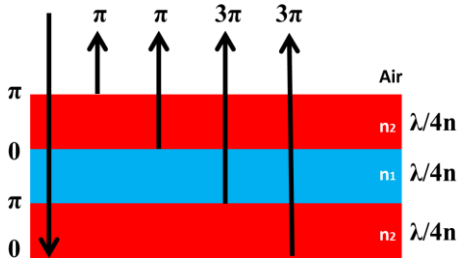

Figure 1-4: Sketch explaining the working of a highly reflective quarter wave stack. Refractive indices of the layers are selected such that n_2>n_1. Phase shift experienced by the light at high to low or low to high interface is marked next to the interface. The reflections are n*2π out of phase with respect of each other so interfere constructively.

A couple of quarter wave stacks having different refractive index contrasts between low and high index layers are simulated to show that stronger reflections can be achieved for the stack having larger refractive index contrast. A multilayer 1D PhC can be modelled using the transfer matrix method. Each layer is represented as a 2x2 matrix using its refractive index n and thickness h at a given wave vector $k = \frac{2\pi}{\lambda}$. Reflection and transmission response of a Bragg reflector can be calculated using the matrix:

$$\boldsymbol{M} = \begin{vmatrix} \boldsymbol{Cos(nhk)} & \frac{\boldsymbol{i}}{\boldsymbol{nk}}\boldsymbol{Sin(nhk)} \\ \boldsymbol{inkSin(nhk)} & \boldsymbol{Cos(nhk)} \end{vmatrix} \qquad \textbf{1-6}$$

This matrix describes the transfer of field from one layer to the next inside the stack. Each layer is represented as a matrix and the response of the multilayer is obtained by multiplying these matrices. The reflected and transmitted intensities are found using:

$$\boldsymbol{R} + \boldsymbol{T} = \boldsymbol{1} \qquad \textbf{1-7}$$

MATLAB code implementing the Transfer Matrix Method (in appendix) is used to calculate the reflection and transmission responses of the multilayer reflectors. Two quarter wave stacks having refractive index contrasts of Δn = 0.1 and Δn = 0.4 are

designed for reflection around 850 nm wavelengths. The thickness of each dielectric layer is selected to be one quarter of 850 nm (850/4*n). It is shown by simulations that the stack having a larger refractive index contrast stack needs only 20 pairs of high and low index pairs to achieve almost 100% reflection. On the other hand, the stack with smaller index contrast requires 80 layers. The calculated spectral reflection for both dielectric stacks are shown in Figure 1-5.

(a)

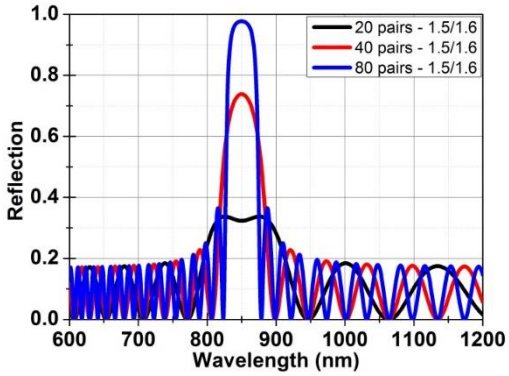

(b)

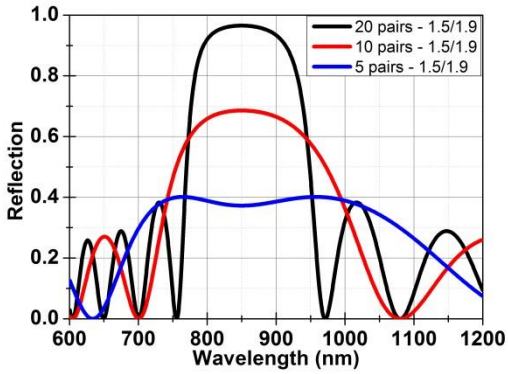

Figure 1-5: (a) Calculated reflections for a quarter wave stack having a refractive index contrast of Δn = 0.1 between low and high index layers. Calculations show that 80 layers are required for almost 100% reflection of the incident light. (b) Calculated reflections for a quarter wave stack having a refractive index contrast of Δn = 0.4 between low and high index layers. Calculations show that 20 layers are required for almost 100% reflection of the incident light.

A cavity inside the dielectric stack can be created by disturbing the periodicity in the middle of the stack. Creation of a cavity results in coupling of a particular resonant wavelength to the cavity. This wavelength starts resonating inside the cavity and results in building up of energy inside the cavity as shown in Figure 1-6(a) below. The quality

factor, sharpness and depth of the defect mode depend on the reflectivity of the side walls (mirrors). A defect inside the high index dielectric stack discussed above is simulated. Calculated transmission and reflection responses for the stack with a defect are shown in the Figure 1-6. It can be noticed that introduction of the defect results in channelling of the resonant (831 nm) wavelength through the stack. The dip/peak in the reflection/transmission response is due to the coupling of the resonant wavelength to the cavity.

(a)

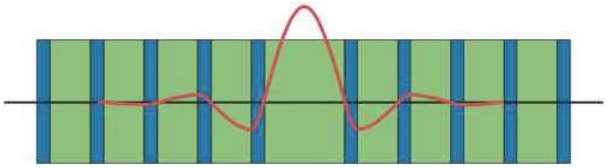

(b)

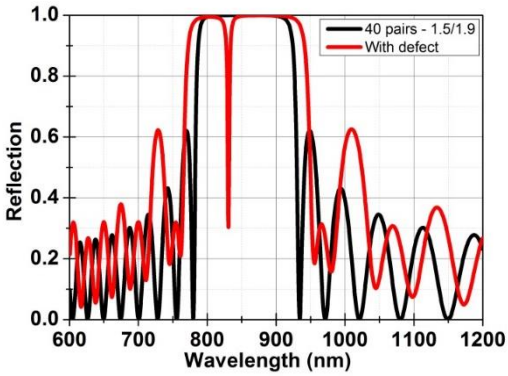

(c)

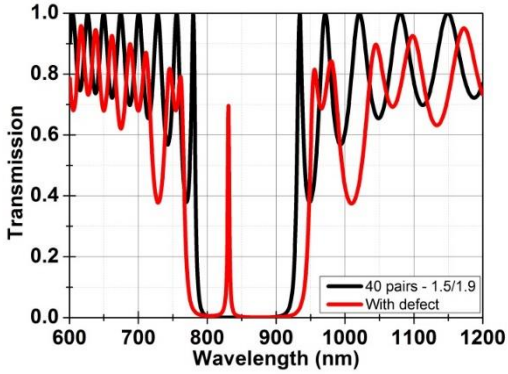

Figure 1-6: (a) A sketch showing building up of the electric field inside the cavity. The cavity is formed by increasing the thickness of the middle layer of the stack. Calculated (b) reflection and (c) transmission responses for 40 pairs of high and low index pairs having a refractive index contrast of Δn = 0.4. Thickness of the middle layer was increased to form a cavity.

To conclude the 1D photonic crystal section, 1D PhC can be designed to act as highly reflective or anti-reflecting coatings. Use of 1D photonic crystal for designing sensors, highly tuneable gratings and cavities and many other applications has been demonstrated [8-13].

1.2.2 Two Dimensional Photonic Crystals (2D-PhC)

In a 2D PhC, the periodic modulation of the refractive index occurs in a plane leaving the third direction uniform. 2D photonic crystals are usually made either by drilling of periodic holes in a slab or by etching everything leaving behind periodically repeating rods. 2D structures with holes are discussed in this section. The holes can be made in a rectangular or triangular arrangement. The widely used triangular lattice is considered here. A unit cell of a triangular lattice is shown in the Figure 1-7(a) below. Light can be incident from the middle of two holes or in-line with the holes as shown in the Figure 1-7(a) below. These directions are named as Γ-M and Γ-K in the reciprocal space. To make it simple, triangular lattice of holes in a slab can be considered as a mix of two 1D dielectric stacks oriented at an angle to each other as shown in Figure 1-7(b). The air filled holes have smaller index than rest of the slab and act similar to a low index layer in a dielectric Bragg grating. The layer containing larger number of holes is considered as a low index layer in contrast to the layer containing lesser number of holes.

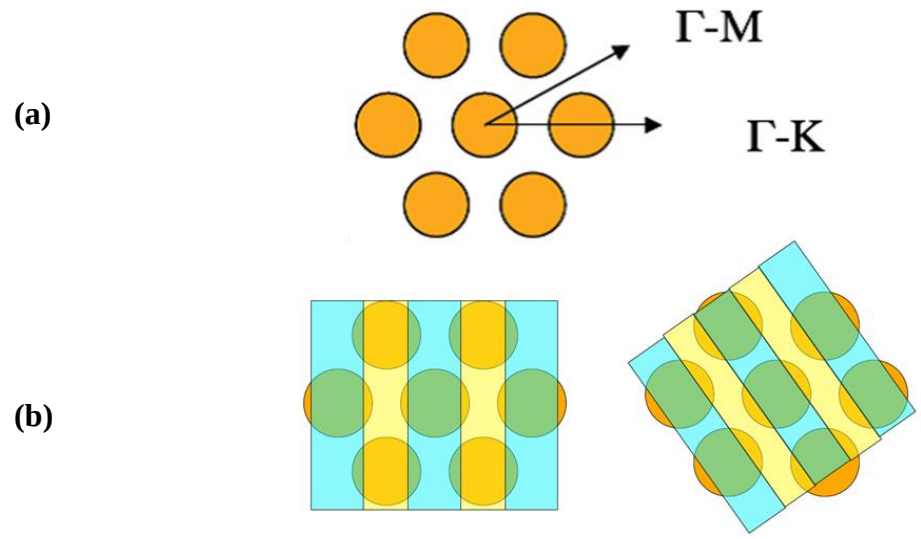

Figure 1-7: (a) A sketch showing a triangular lattice. Γ-M and Γ-K directions in the reciprocal space are marked. (b) Two 1D dielectric stacks oriented at an angle to each other are used to represent the stack.

Reflections from different planes of the triangular lattice can be explained using the bandstructure (dispersion diagrams). Absence of modes in a dispersion diagram marks the band-gap. Opening of a band-gap for a particular direction results in reflection from that plane of incidence. A complete band-gap results in reflection of light for all directions of incidence. Bandstructures of a 2-D photonic crystal for both TE and TM polarised light are calculated to show opening of a complete band-gap for a TE polarised light only. The bandstructure are calculated using commercially available Finite Difference Time Domain (FDTD) software from Lumerical Solutions. The code used for calculations and plotting of the data is available in the appendix. The simulated photonic crystal has a lattice constant of a=500 nm with 200 nm radius air filled holes. The holes are made in a Ta_2O_5 slab having a refractive index of n = 2. The calculated bandstructures are shown in Figure 1-8. The horizontal axis represents the Γ-M, Γ-K and M-K orientations of the simulated crystal in the reciprocal space. The calculated bandstructure for TE shows a complete band-gap for frequencies lying between $f_1 = 2.43\text{x}10^{14}$ Hz and $f_2 = 2.96\text{x}10^{14}$ Hz. The corresponding wavelengths can be calculated as:

$$\boldsymbol{\lambda_1 = \frac{c}{f_1} = \frac{3*10^8}{2.43*10^{14}} = 1.23\mu m} \qquad \textbf{1-8}$$

$$\boldsymbol{\lambda_2 = \frac{c}{f_2} = \frac{3*10^8}{2.96*10^{14}} = 1.45\mu m} \qquad \textbf{1-9}$$

A complete band-gap is not noticed for a TM polarised light. A TE polarised light with wavelengths falling in the band-gap will be reflected from the crystal irrespective of the direction of incidence as a complete band-gap is available for these wavelengths. The reflection response of the same crystal for light incident from middle of the holes (i.e. Γ-M direction) is calculated. Back reflections around 1300 nm wavelengths are calculated. The calculated reflection response is plotted over the bandstructure to show that the reflection peak lies inside the Γ-M band-gap.

(a)

(b)

(c)

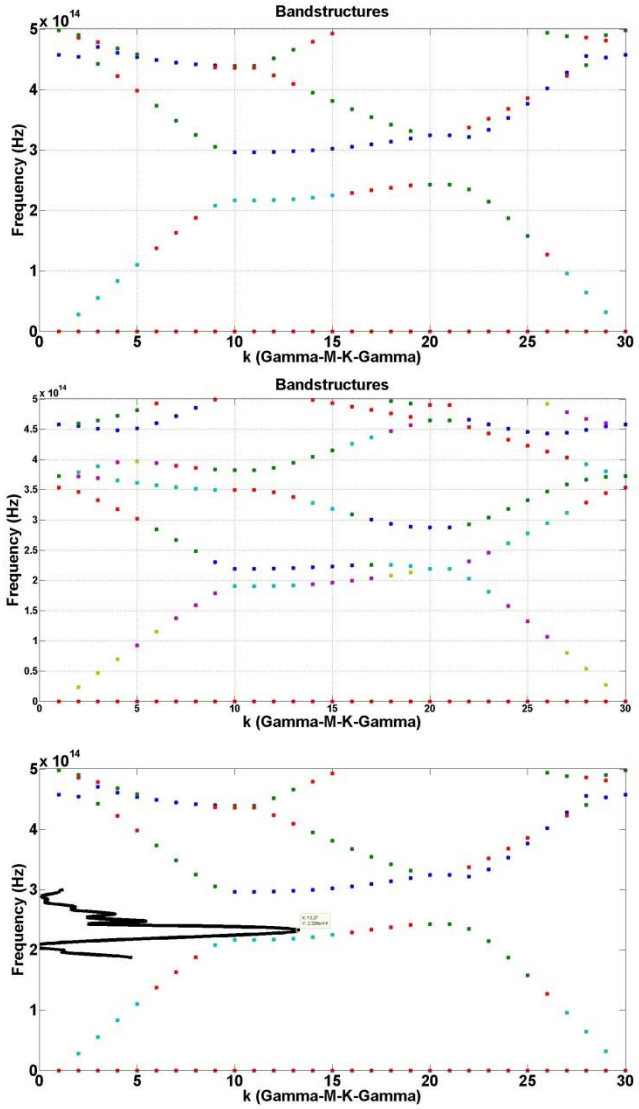

Figure 1-8: Calculated bandstrures for (a) TE and (b) TM polarized lights. There is a complete band-gap for wavelengths ranging from 1.23µm to 1.45µm for TE polarized light only. (c) Calculated reflection response is plotted over the TE bandstructure. It can be observed that reflection lies in the band-gap region.

A 2D PhC cavity can be created by removing some spheres or by changing the radius of some of the spheres inside the crystal. Creation of a cavity results in coupling of a particular resonant wavelength to the cavity. A cavity in the above mentioned triangular lattice crystal is formed and simulated by removing the central hole and by reducing the radius of six surrounding holes as shown in Figure 1-9(a). The resonance wavelength of the cavity was calculated and it was found that light starts building up at the resonance wavelength. A static image of the field inside the cavity is shown in the Figure 1-9(b)

below. The quality factor of the cavity can be tuned by changing the parameters of the cavity. High quality factor cavities have already been demonstrated and applied for different applications [14, 15]. Waveguiding of light using a line defect inside the photonic crystal has also been demonstrated [16-18]. The light inside a line defect waveguide is guided by the photonic crystal in the lateral direction and by total internal reflection in the vertical direction.

(a)

(b)

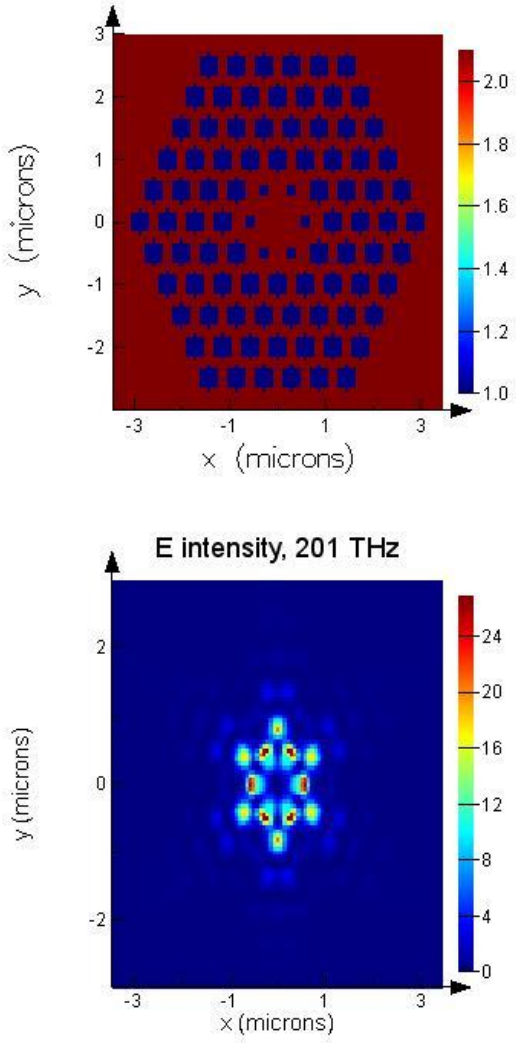

Figure 1-9: (a) Refractive index profile of the modelled cavity formed by removing a hole in the centre and reducing the radius of the six surrounded holes. (b) Calculated electric field for the resonant mode at 1492 nm wavelength.

To conclude the 2D photonic crystal section, 2D photonic crystals can be designed for different applications including sensing [19, 20], high Q cavities [14, 15], waveguiding [16-18] and slowing of light [21-24].

1.2.3 Three Dimensional Photonic Crystal (3D - PhC)

In a 3D PhC, the periodic modulation of the refractive index occurs in all three directions of the crystal. Three dimensional photonic crystals can either be opal or inverted-opal in nature. Mono dispersed particles are used to fabricate both opal and inverted opal structures. Deposition of spheres on a substrate results in an opal structure. Inverted-opal structures are made from the opal structures by infiltrating the voids between the spheres with some material and then removing the spheres to get a honey comb like structure. Inverted opal structures have very low refractive index as air takes place of the spheres after the removal of the colloids. Opal photonic crystal structures are discussed in this section.

Natural sedimentation of mono-dispersed particles on a flat surface is the easiest way to realise three dimensional colloidal photonic crystal structures. The multi-layer structures fabricated in this manner can be expected to have horizontal layers of hexagonally packed spheres stacked above each other. These hexagonally packed layer of spheres are called (111) planes. The Face Centre Cubic (FCC) lattice is formed if each individual horizontal layer of spheres repeats itself at every third layer in vertical direction. Three different positioning, repeating every third layer, can be designated as A, B and C arrangements and the stacking of repeated ABCABC... is the FCC lattice as shown in Figure 1-10 (a). The FCC lattice is formed only if everything goes right in the natural sedimentation process with the spheres positioning themselves at the right locations without any defects. Defects in the sedimentation process can change the repetition from say the third to every second layer resulting in AB, BC or AC stacking. Structures having alternating layers of spheres like ABAB… are called Hexagonal Closed Pack (HCP) structures, Figure 1-10 (b). So, any deviation from ideal sedimentation will result in changing of FCC into HCP and a mix of FCC and HCP lattice results. This mix of FCC and HCP lattices can be named as a Random Face Cantered Cubic (RFCC) lattice, Figure 1-10 (c).

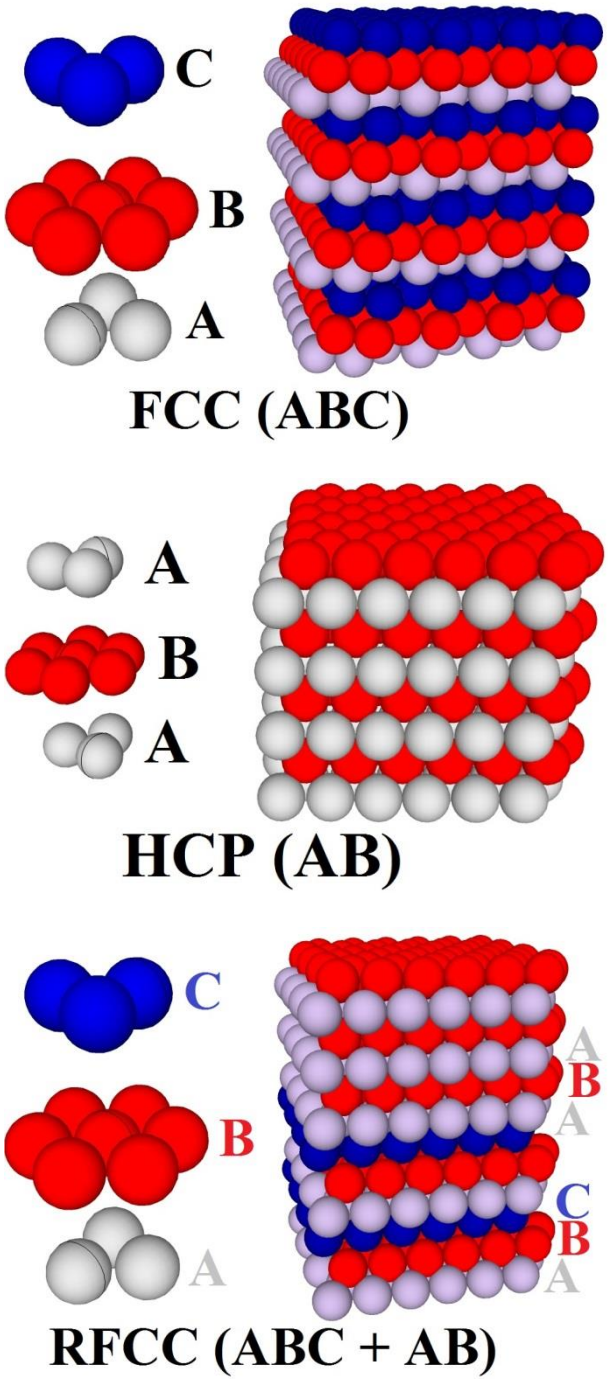

Figure 1-10: Three different relative arrangements of spheres: A, B and C are represented in White, Red and Blue colours respectively to show the stacking of (a) Face Cantered Cubic (FCC) (b) Hexagonal Closed Packed (HCP) and (c) Random Face Cantered Cubic (RFCC) structures.

The reflections from different orientations of the crystal can be explained using the bandstructure. The bandstructure of FCC structures are calculated to map different FCC reflecting planes in the reciprocal space by plotting the calculated reflection responses over the bandstructure. Calculated bandstructure of the FCC crystal are shown in Figure 1-11 (a). The bandstructure shows openings of band-gaps in different orientations of the crystal lattice in the reciprocal space. The calculated reflection from the (111) plane is plotted over the bandstructure in Figure 1-11 (b) to show that (111) plane of FCC is represented by Γ-L direction in reciprocal space. The reflection peak from the (111) plane falls exactly on top of the band-gap with Full Width Half Maximum (FWHM) equal to the opening of the band-gap. The bandstructure dispersion in the Γ-L direction is linear and behaves like a simple Bragg reflector. This band-gap in Γ-L direction moves to higher frequencies as we move from L to W directions in the reciprocal space. Movement from L to W points in the reciprocal space is equivalent to changing the angle of incidence of light on (111) plane. This movement of band-gap to higher frequencies is in agreement with the Bragg's law of dispersion with the resonance frequency moving to larger values with an increase in the angle of incidence.

It can be observed that band-gap in L-U and L-K directions follow the same trend so it can be concluded that L-U and L-K directions in the reciprocal space are identical. Reflections from (001) plane of FCC unit cell is mapped to the middle point of W-K directions which is named as X. FCC (001) plane has spheres placed in a rectangular arrangement instead of the hexagonal arrangement as for FCC (111) plane. FCC (001) planes will be discussed in more details in Chapter 5. The calculated reflection response for normal incidence of light on (001) plane of FCC photonic crystal shows a reflection peak around 1.6 THz. The reflection spectrum from the (001) plane of FCC is plotted over the calculated bandstructure in Figure 1-11 (c) to show that reflection peak falls in the band-gap frequencies at X point which is right in the middle of W-K direction. It can be observed in the bandstructure that band-gap at X moves to larger frequency values on moving towards W or K point from X.

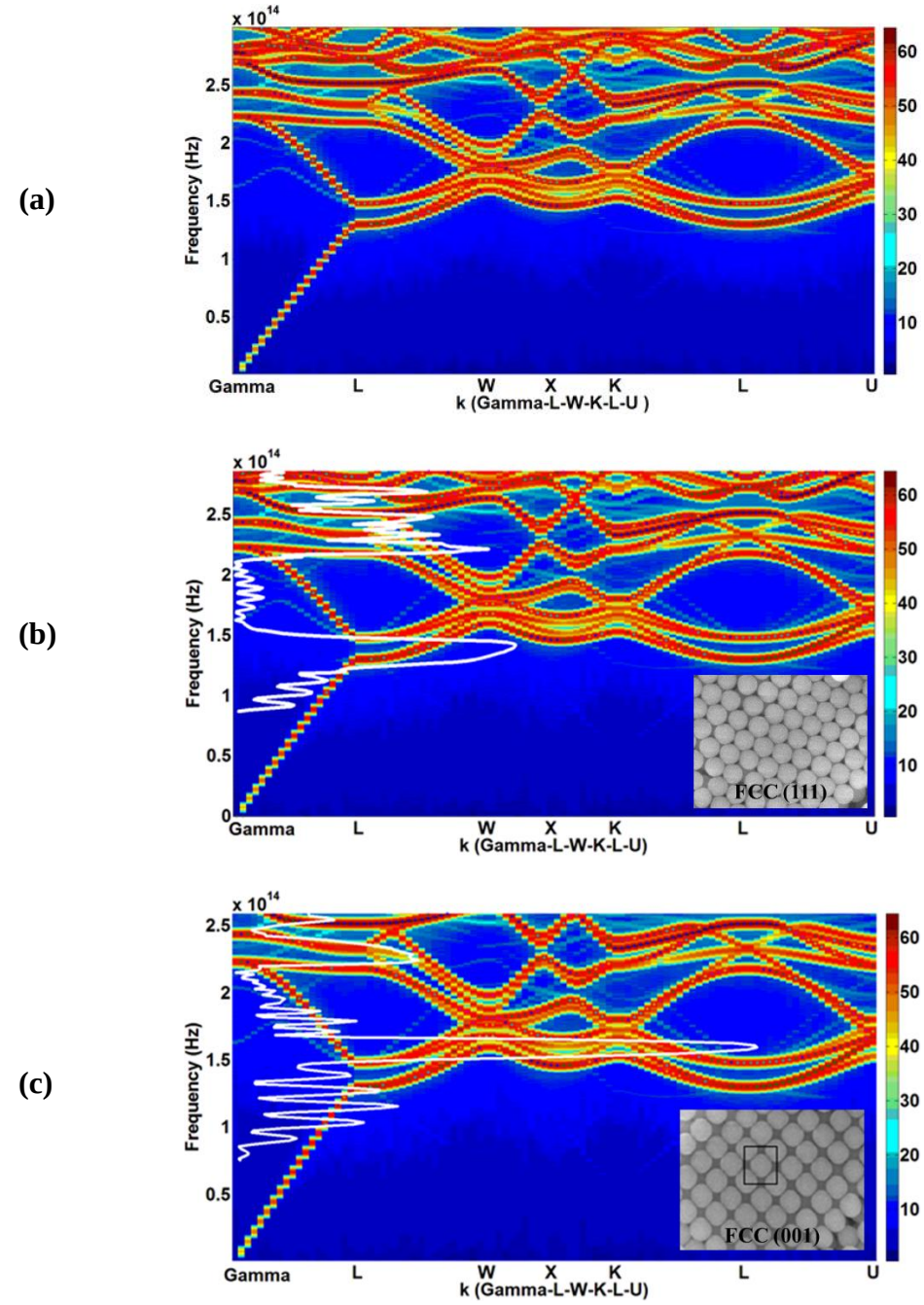

Figure 1-11: (a) Bandstructure of FCC crystal. (b) Back reflections from (111) FCC plane are plotted over the bandstructure to show that FCC (111) is represented by Γ-L in the reciprocal space. (c) Reflection from (001) FCC plane is in agreement with band-gap at X point.

The bandstructure shows inter-crossings of optical bands near K/U and W points in the reciprocal space. The crossings of the bands result in transfer of energy between the optical bands present for those frequencies. A small reflection peak in the reflection response appears just next to the strong reflection peak at the start of the inter-crossing. This new peak gets energy from the stronger peak in the neighbourhood in result of the energy transfer. As a result, the initial peak before the start of the crossing transfers its complete energy to the new born peak and disappears.

It should be mentioned here that fabrication techniques for three dimensional crystals are not so mature and controlled defects cannot be fabricated. Cracks appear in multilayer samples on drying of the spheres. Pure FCC structures can be achieved for smaller spheres but formation of RFCC or HCP is also very common for larger sphere sizes. Achieving a controlled defect inside a colloidal crystal is almost impossible to form a desired cavity.

To conclude the 3D photonic crystal section, 3D crystals have been studied and fabricated to explore different opportunities. Colour changing polymer sheets have been used for a few real life applications [25, 26]. As fabrication of these crystals lack control so use of colloidal crystal for real life applications is very limited at the moment.

1.3 Thesis Outline

A general introduction to optical waveguides and photonic crystals was provided in this chapter. In chapter 2, 1D photonic crystal structures are used to demonstrate a sensitive, simple and easy to fabricate optical sensor. A prism is used for matching of wave vectors for the demonstrated sensor. It is shown that on-chip sensing without the prism can also be achieved using polymer waveguides. In chapter 3, on-chip sensors are experimentally demonstrated using polymer waveguides. In chapter 4, polymer waveguides are studied and implemented to demonstrate a multilayer optical printed circuit board. In chapter 5, sharp bends for polymer waveguides discussed in chapter 4 are demonstrated using 3D-PhC structures. Here is the detailed outline of my thesis.

In chapter 2, the use of 1D photonic crystal for the realisation of an optical sensor capable of sensing a refractive index change over the surface is explained. A simple

sensing surface is designed and implemented by depositing a pair of silicon (Si) and silica (SiO_2) layers on sapphire substrate. The demonstrated sensitivity is compared to the already reported sensitivities for sensors using multiple pairs of layers to show that comparable sensitivities can be achieved using this simple and easy to fabricate sensor. The working principle for the sensor is explained and attributes compared to the already commercialised sensors. At the end of the chapter, it is shown using simulations that on-chip sensing can be achieved by depositing the silicon (Si) and silica (SiO_2) layers on a polymer waveguide instead of depositing on a sapphire prism.

In Chapter 3, novel on-chip sensing is demonstrated by cladding a polymer waveguide with silicon (Si) and silica (SiO_2) layers. The waveguide is excited using end-fire coupling to measure a resonance dip in the transmission. Design of the sensor for operation around telecom wavelengths is presented for measurements using the tuneable laser source and detectors readily available in the labs.

In chapter 4, polymer waveguides are investigated and implemented. A centimetre sized multi-layer optical printed circuit board (OPCB) for transportation of light from one component to another is demonstrated using polymer single mode waveguides and passive optical devices. The OPCB helps overcoming the issues faced by the conventional electrical PCBs at higher data rates. In-plane single mode waveguides, directional couplers, multi-mode interference (MMI) and Y-splitters are designed, fabricated and optically characterised to demonstrate the working at a single optical level. A method to quantify a small variation in refractive index contrast between the core and cladding of the polymer waveguides using a tuneable laser is explained. Multilayer optical interconnects are designed and fabricated to demonstrate the working of an ‘optical via’ and a ‘1x4 optical 2-D port’. Coupling of light from one level to another is experimentally demonstrated similar to the working of an electrical via in copper based electrical interconnects.

In chapter 5, the use of both opal and inverted-opal 3D photonic crystal structures for polymer optical interconnect is explained. Design and implementation of opal structures to achieve sharp bends for polymer waveguides is presented. It is shown that rectangular seed layer can be used to achieve FCC (001) stacking. Opal based reflectors are integrated

at 45° to the waveguides for in-plane bending of light at right angles. In a second demonstrator, inverted-opal structures having an effective refractive index close to air are used as under cladding for the polymer waveguide core to demonstrate effectively an air suspended polymer waveguide.

In chapter 6, the thesis is concluded and future possible research work is discussed.

1.4 References

[1] R. Hunsperger, *Integrated Optics, Theory and Technology*, Springer (2009)

[2] J. Fluitman, T. Popma, "Optical waveguide sensors," Sensors and actuators 10 (1), 25-46 (1986).

[3] H. Mukundan, A. S. Anderson, W. K. Grace, K. M. Grace,N. Hartman, J. S. Martinez, B. I. Swanson, "Waveguide-Based Biosensors for Pathogen Detection," Sensors 9, 5783-5809 (2009).

[4] R. C. Alferness, "Waveguide electrooptioc modulator" IEEE Trans. actions on Microwave Theroy and Techniques 30(8), (1982)

[5] V.E. Babicheva, A.V. Lavrinenko, "Plasmonic modulator based on metal-insulator-metal waveguide with barium titanate core", Photonics Letters of Poland 5, 57-59 (2013).

[6] V.E. Babicheva, I.V. Kulkova, R. Malureanu, K. Yvind, A.V. Lavrinenko, "Plasmonic modulator based on gain-assisted metalsemiconductor-metal waveguide," Photonics and Nanostructures - Fundamentals and Applications 10, 389-399 (2012).

[7] V.E. Babicheva, A.V. Lavrinenko, "Plasmonic modulator optimized by patterning of active layer and tuning permittivity," Optics Communications 285, 5500–5507 (2012).

[8] J. L. Floch, M. Tobar, D. Cros, J. Krupka, "High Q-factor distributed bragg reflector resonators with reflectors of arbitrary thickness," IEEE Trans. Ultrason. Ferroelect. Freq. Control 54(12), 2689-2695 (2007).

[9] A. Fu, H. Gao, P. Petrov, P. Yang, "Widely Tunable Distributed Bragg Reflectors Integrated into Nanowire Waveguides," Nano Lett. **15**, 6909−6913 (2015).

[10] F. Michelotti, B. Sciacca, L. Dominici, M. Quaglio, E. Descrovi, F. Giorgis, F. Geobaldo, “Fast optical vapour sensing by Bloch surface waves on porous silicon membranes,” Phys. Chem. Chem. Phys. 12(2), 502-506 (2010)

[11] G. A. Rodriguez, J. D. Lonai, R. L. Mernaugh, and S. M. Weiss, “Porous silicon Bloch surface and sub-surface wave structure for simultaneous detection of small and large molecules, ” Nanoscale Res. Lett. 9, 383 (2014).

[12] G. A. Rodriguez, J. D. Ryckman, Y. Jiao, S. M. Weiss, “A size selective porous silicon grating-coupled Bloch surface and sub-surface wave biosensor,” Biosens Bioelectron 53, 486-493 (2014).

[13] H. Qiao, A. H. Soeriyadi, B. Guan, P. J. Reece, J. J. Gooding, “The analytical performance of a porous silicon Bloch surface wave biosensors as protease biosensor,” Sens. Actuators B Chem. 211, 469-475 (2015).

[14] Y. Akahane, T. Asano, B-S Song, S. Noda, “High-Q photonic nanocavity in a two-dimensional photonic crystal” Nature 425, 944-947 (2003).

[15] I. Bayn, J. Salzman, “Ultra high-Q photonic crystal nanocavity design: The effect of a low-ε slab material,” Opt. Express 16(7), 4972-4980 (2008).

[16] V. Liu, S. Fan, “Compact bends for multi-mode photonic crystal waveguides with high transmission and suppressed modal crosstalk,” Opt. Express 21(7), 8069-8075 (2013).

[17] J. D. Joannopoulos, P. R. Villeneuve, S. Fan, “Photonic crystals: putting a new twist on light,” Nature 386, 143 (1997).

[18] C. Jamois a, R. B. Wehrspohn, L. C. Andreani, C. Hermann, O. Hess, U. Gösele, “Silicon-based two-dimensional photonic crystal waveguide,” Photonics and Nanostructures – Fundamentals and Applications 1, 1-13 (2003).

[19] Y. Zhang,Y. Zhao, R-Q Lv, “A review for optical sensors based on photonic crystal cavities,” Sens. and Act. A: Physical 233, 374–389 (2015).

[20] R. V. Nair, R. Vijaya, “Photonic crystal sensors: An overview,” Progress in Quantum Electronics 34 (3), 89–134 (2010).

[21] T. Baba, “Slow light in photonic crystals,” Nature Photonics 2, 465-473 (2008)

T. F. Krauss, “Slow light in photonic crystal waveguides,” J. Phys. D Appl. Phys. 40, 2666-2670 (2007)

[22] M. Soljacic, S. G. Johnson, S. Fan, M. Ibanescu, E. Ippen, J. D. Joannopoulos, “Photonic-crystal slow-light enhancement of nonlinear phase sensitivity,” J. Opt. Soc. Am. B 19, 2052-2059 (2002)

[23] J. Li, L. Faolain, S. A. Schulz, T. F. Krauss, “Low loss propagation in slow light phtotonic crystal waveguides at group indices up to 60” photonics and nanostructures – fundamental and applications 10(4), 589-593 (2012)

[24] P. Hamel, P. Grinberg, C. Sauvan, P. lalanne, A. Baron, A. M. Yacomotti, I. Sagnes, F. Raineri, K. Bencheikh, J. A. Levenson, “Coupling light into slow-light photonic-crystal waveguide from a free-space normally-incident beam,” opt. Express 21(13), 15144-15154 (2013)

[25] L. A. Woldering, A. P. Mosk, W. L. Vos, “Design of a three-dimensional photonic band gap cavity in a diamondlike inverse woodpile photonic crystal,” Phys. Rev. B 90(11) (2014)

[26] S. Kawashima, K. Ishizaki, S. Noda, “Light propagation in three-dimensional photonic crystals,” Opt. Express 18(1), 386-392 (2010).

CHAPTER 2

1D Photonic Crystals for Sensing

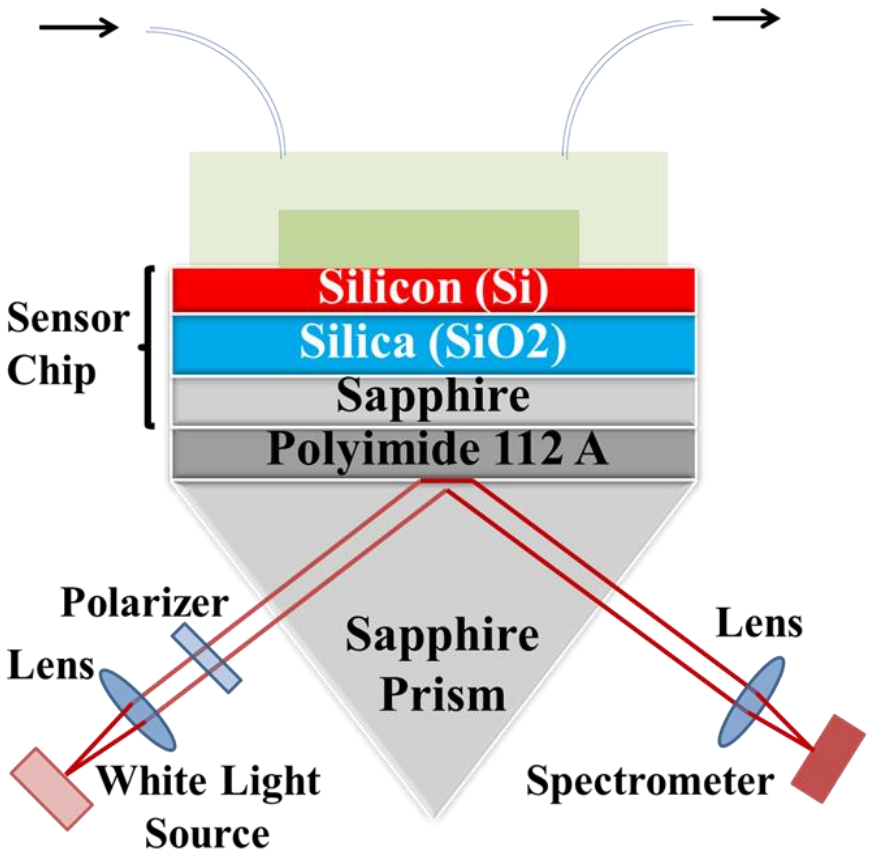

Publications from Chapter

- **Muhammad Umar Khan** and Brian Corbett, "Bloch surface wave structures for high sensitivity detection and compact waveguiding" Sci. Technol. Adv. Mater. 17, 398-409 (2016).
- **Muhammad Umar Khan**, John Justice, Pierre Lovera, Brian Corbett, "Simplified Bloch surface wave sensors," Conference paper (In preparation).

My Contributions

It was my own idea to decrease the number of layers and then to deposit on a polymer waveguide to achieve on-chip resonances. Designed, simulated and characterised the sensors. Samples were fabricated by John Justice.

About simplified BSW design

It should be mentioned here that the basic aim was to simplify the structure by reducing the number of layers. This reduction in number of layers helps reducing fabrication effort resulting into reduced cost of the sensor. The confinement of the electric field was taken care of by choosing silicon as the terminating layer. The field strength at the surface can be optimised at the expense of the number of layers or by improving the design.

2 1D Photonic Crystals for Sensing

There has been on-going research activity aimed at the realisation of optical sensors for the measurement of chemical and biological analytes for many decades. The first optical chemical sensor was reported in 1975 for the measurement of CO_2 and O_2 concentration using the changes in absorption spectrum [1]. Since then, various optical approaches including ellipsometry, spectroscopy, interferometry and surface electromagnetic waves (SEW) have been used as the measurement method [2, 3].

In this chapter, the use of 1D photonic crystals for sensing purposes is discussed. After discussing the importance and working of some optical sensors, surface plasmon resonance (SPR) based optical sensors are explained which have already been commercialized and are mostly used for refractive index based label-free sensing. SPR based sensors have broad resonances due to the losses associated with the metals and can only be operated at the metal dependent wavelengths. Operation around desired wavelengths with sharper resonances can be achieved by replacing the metal layer with a dielectric stack. These sensors using a dielectric stack are called as Bloch surface wave (BSW) sensors.

By presenting a couple of already reported BSW sensors, it is shown that BSW sensors can be designed for both TE and TM polarised light in comparison to SPR which can operate for TM polarised light only. It is shown that the number of dielectric layers can be reduced by increasing the refractive index contrast between the high and low index materials in the stack. A sensor using only a single pair of high (Si) and low (SiO_2) index layers is proposed, explained and experimentally demonstrated. It is the first time that a BSW-like sensor using only a single pair of high and low index dielectric layers is demonstrated. A similar structure using only a couple of layers (resonant mirror) was reported in 1993 [4, 5] but a resonance in the transmission response has not been reported to date. Phase change in the reflection was used for resonant mirror. The presence of a resonance dip in the reflection for the demonstrated sensor distinguishes it from the resonant mirror. The surface waves are excited using the prism based Kretschmann-Raether (K-R) configuration [6, 7]. The prism is used for matching of wave-vectors of the incident light and the surface wave. It is shown using simulations that the demonstrated 2

layer platform can be designed using silicon-on-insulator (SOI) platform for operation around telecom wavelengths. Silicon is transparent around telecom wavelengths and results in sharper resonances with better sensitivities.

A novel waveguide coupled BSW platform is proposed after the demonstration of the Kretschmann-Raether (K-R) based sensor. This waveguide coupled platform helps achieving on-chip sensing by eliminating the prisms used in K-R configuration. The waveguide coupled resonances are experimentally demonstrated in chapter 3.

2.1 Optical Sensors

An optical sensor revolves around the transducer to inter-relate the optical and (bio) chemical domains which transforms changes in the quantity of interest into changes in the optical properties of the incident light. Typically, a bio-recognition layer is attached to the surface of the transducing medium to make the sensor selective. The interaction of the target analyte with the recognition layer produces a change in the refractive index at the surface. This change in refractive index above the surface is reflected into a change in optical properties of the incident light which may be determined by optoelectronic part of the sensor.

The sensitivity of the sensors is defined as the derivative of the monitored optical parameter (resonance angle, wavelength, intensity or phase) with respect to the parameter to be determined (refractive index, concentration etc.). Sensor resolution or Limit of Detection (LoD) is the minimum change in the parameter to be determined which can be resolved by a sensing device. The influence of the temperature, light source and photo detector noise play an important role in determining the sensor resolution. It should be noted that the accuracy with which the measured parameter can be determined is very dependent upon the experimental circumstances and the degree of optimisation of the particular sensor and therefore the ultimate resolution of the particular sensor may differ from that of the considered model systems.

2.1.1 Refractive index based label-free sensing

There are two main detection protocols used in optical biosensors: fluorescence based sensing and label-free sensing. The bio recognition layer or the target analyte is tagged with florescent dyes for fluorescence based sensing. The intensity of the florescent signal determines the presence of the target analyte or the interaction of the analyte with the recognition layer. The process of tagging makes this approach expensive and difficult to implement. The process of tagging affects the natural functionality of the molecules also. The tagging process is not uniform, so the number of tags associated with a single molecule cannot be controlled. These difficulties in the fluorescence based protocol makes a label free sensing protocol more suitable as tagging of the molecules is not required. The absence of tagging process makes this detection protocol simple and cost effective. The natural functionality of the molecule is not affected in the label-free detection technique.

There are mainly two types of detection techniques in the label-free detection: Raman Spectroscopy and the refractive index based detection. The scattered light from the sample and the change in refractive index over the surface of the sensor are used for detection in the Raman spectroscopy and refractive index based measurements respectively. Various refractive index based optical sensors including resonant waveguide gratings (RWG), ring resonators, photonic crystal based sensors and surface electromagnetic Waves (SEW) based sensors have been widely used for label-free sensing. SEW based label-free sensors will be discussed for the rest of this chapter.

2.2 Surface Electromagnetic Wave (SEW) Sensors

SEW are the electro-magnetic waves that propagate along the interface between two media and can be strongly confined and significantly enhanced at the surface and decay exponentially into the neighbouring media. The optical properties of the two media determine the kind of SEW that can be sustained. SEW have been studied and demonstrated in many photonic application areas, among which sensing methods based on surface waves have become powerful diagnostic tools due to their unique properties, such as high surface sensitivity, real-time and label-free detection. The most popular

surface wave based sensing technology is undoubtedly the surface plasmon resonance (SPR) method [2, 3].

2.2.1 Surface Plasmon Resonance (SPR)

SPR is based on the excitation of the surface plasmon wave along the interface of two media having positive and negative dielectric constants e.g. metal and dielectric. The surface plasmon wave is actually a travelling wave of oscillating charges at the surface of the metal. These waves can be stimulated using an optical wave having a wave-vector matching that of the surface wave. The Drude model can be used to show the relationship between the wave-vector (β) along the interface and the angular frequency (ω) as shown in Equation 2-1 below.

$$\boldsymbol{\beta} = \frac{\omega}{c}\sqrt{\frac{\varepsilon_m + \varepsilon_d}{\varepsilon_m \varepsilon_d}} \qquad \textbf{2-1}$$

where c is the speed of light in vacuum, ε_m and ε_d are the dielectric constants of the metal and the dielectric respectively.

The surface plasmon wave is usually excited using the prism coupled Kretschmann-Raether (K-R) configuration [6, 7] to match the wave-vectors, Figure 2-1 (a). The incident light from the source is reflected from metal interface and detected by the spectrometer. The wave-vector of the incident light matches that of the plasmon wave at a particular angle of incidence resulting in a decrease of reflected light at the resonance. Both angle and wavelength dependent measurements can be performed to find the surface plasmon resonance. The field distribution of a SPR mode is calculated to show that the resonant mode is evanescent in nature and the field decays away from the metal surface in both the dielectric and the medium above the metal. The simulated SPR sensor comprised of a 45 nm thick gold (Au) layer on BK7 glass. A 5 nm thick titanium adhesion layer was also taken into consideration for an accurate modelling. The calculated SPR mode at 820 nm wavelength had an effective index of 1.38 with a penetration depth of 375 nm into the water. Bio-recognition (Antibodies) layer is usually deposited on the gold surface to allow only the desired analytes (Antigen) to attach. This attachment of the antigen causes a change in refractive index over the surface of the sensor resulting in a shift of resonance angle/wavelength.

(a)

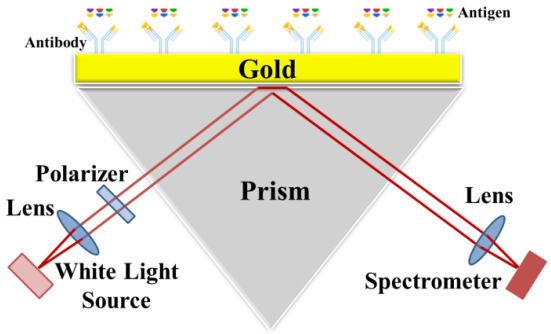

(b)

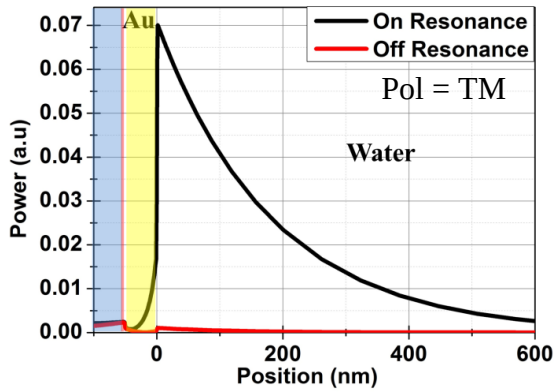

Figure 2-1: (a) Sketch of the SPR sensor showing the way it is excited using the Kretschmann-Raether (K-R) configuration. The sketch shows the bio recognition layer (Antibody) attached to the surface of the sensor to selectively attach the desired antigen. (b) The calculated power distribution shows that SPR mode is evanescent in nature with a penetration depth (1/e of electric field) of 375 nm into the water. The calculations were made for an incident light of 820 nm.

In the 1970's the potential of SPR for characterisation of thin films [8] and monitoring processes at metal interfaces [9] was recognized. The use of SPR for gas sensing and bio-sensing was demonstrated in 1982 [10-12]. In 1990, the use of SPR sensors for biological detection applications was commercialized by Biacore® [13]. Since then SPR sensing has been receiving continuously growing attention from scientific community. Noise estimations reveal that best performing plasmon based systems have nearly reached their theoretical limits [14]. One route to better performing sensors based on plasmons could be to laterally pattern the structure [15, 16] in order to exploit local field enhancement. Alternatively, modes guided at the surface of a dielectric one-dimensional photonic crystal [17, 18] have been suggested for plasmon like sensing [18,

19]. These guided modes at the surface of a dielectric one-dimensional photonic crystal are called Bloch Surface Waves (BSW) which exploit the band gap in a dielectric truncated one dimensional photonic crystal [20] to obtain guiding of a surface mode, thus giving rise to surface sensitive evanescent field sensors [21-23].

2.3 Bloch Surface Waves (BSW)

It was theoretically reported in 1977 that dielectric multilayers can sustain BSW [20] followed by the first experimental demonstration in 1978 [24]. A periodic layered structure consisting of 12 pairs of alternating layers of 500 nm thick GaAs and 500 nm thick $Al_{0.2}Ga_{0.5}As$ on a GaAs substrate was used to show BSW at the excitation wavelength of 1150 nm. At the start of the 1990s, it was experimentally shown that 2-D photonic crystal structures can also sustain the BSW [25, 26]. Recently, the BSW sustained at the truncated interface of finite one-dimensional dielectric photonic crystals (1D-PhC) have been investigated as an alternative to SPR where the metal used in SPR is replaced by a multilayer Bragg reflector. The resonance occurs by the excitation of the BSW at the interface between the Bragg reflector and the surrounding medium. There are several advantages provided by BSW propagation on flat dielectric surfaces. The BSW have longer propagation lengths as they travel on dielectric surfaces having very small losses. The use of a Bragg reflector provides greater freedom in the operating wavelengths than SPR, which is limited to a narrow range of metal dependent wavelengths. The Bragg reflector can be designed to sustain both the TE and TM polarised BSW, a condition that cannot be achieved with SPR as they are only TM polarised. Furthermore, the field intensity associated with the BSW can be enhanced by several orders of magnitude close to the surface. This tuneable localised field confinement is particularly attractive for bio sensing, waveguiding platform and enormous field enhancements [27, 28].

2.3.1 Bloch Theorem:

To investigate the propagation behaviour in periodic structures, modes of the periodic structures are determine from the solutions of Maxwell's equations in periodic medium (no source terms). A general solution to this problem is given by the Bloch theorem and the modes of the periodic medium are called Bloch modes.

For the sake of simplicity, I am considering one dimensional problem in which the refractive index n(x) is periodic in the x-direction with period Λ. Ψ(x) is the complex representation of the field Ψ(x, t) (meaning (x, t) = Re Ψ(x) $e^{j\omega t}$) and satisfies following wave equation

$$\frac{d^2\Psi}{dx^2} + k_0^2 n^2(x)\Psi(x) = 0 \qquad \textbf{2-2}$$

where k_o and λ_0 respectively are the free space wave vector and free space wavelengths. For periodic modulation of the refractive index, Bloch theorem states that a general solution of the Maxwell's equations is

$$\Psi(x) = e^{ikx}u_k(x) \qquad \textbf{2-3}$$

where $u_k(x)$ is a periodic function with same period as n(x). The periodic function $u_k(x)$ can be written as

$$u_k(x) = \sum_{l=-\infty}^{\infty} c_l e^{-ilKx} \qquad \textbf{2-4}$$

In the coming sections, the design of BSW structures and their use for sensing applications is discussed. By presenting already reported structures, it is demonstrated that the BSW can be designed for both TE and TM polarised light. The role of the refractive index contrast and number of layers is explained through simulations. A novel design of a sensing platform using only a single pair of high index contrast (Si/SiO_2) layers is explained and implemented to show a sensitivity of 900 nm/RIU. It is shown using simulations that this 2 layer high index contrast sensor principle can be applied to silicon-on-insulator (SOI) at a wavelength of 1550 nm where Si is transparent and sharper resonances with better sensitivities (1950 nm/RIU) can be obtained. After the experimental demonstration of K-R based sensor, a waveguide coupled BSW sensor is proposed for on-chip sensing. These novel waveguide coupled resonances are explained and experimentally demonstrated in chapter 3.

2.3.2 Design of Bloch Surface Wave Sensors

A BSW can be excited on the surface of a highly reflective one-dimensional photonic band-gap or Bragg reflector designed with the optical thickness of each layer being one quarter of the target reflecting wavelength, λ.

$$\boldsymbol{d_H = \frac{\lambda}{4 * n_H * Cos(\theta_H)}} \quad \textbf{2-5}$$

$$\boldsymbol{d_L = \frac{\lambda}{4 * n_L * Cos(\theta_L)}} \quad \textbf{2-6}$$

where d_H, d_L represent the thicknesses of the high and low index materials while n_H and n_L represent the refractive index values of the high and low index materials respectively. The θ_H and θ_L are the angles inscribed inside the high and low index layers respectively. The bandwidth of the reflection is set by the number of mirror pairs and the refractive index contrast, Δn. An increase in Δn results in both a higher reflection for a given number of mirror pairs and a wider reflection bandwidth. A transmitting mode inside the band-gap can be initiated by breaking the periodicity of the Bragg reflector and can be made to travel on the surface of the Bragg reflector by truncating the reflector at the appropriate thickness.

BSW is mostly excited using the prism based Kretschmann-Raether (K-R) excitation configuration to measure the angular or wavelength dependent resonance responses. The K-R configuration is used to match the wave-vectors of the incident light and the BSW as explained earlier in the SPR section. The wave-vector of the BSW (β_{BSW}) can be calculated using equation 2-7 below.

$$\boldsymbol{\beta_{BSW} = \frac{2\pi}{\lambda} * n_{prism} * Sin(\theta)} \quad \textbf{2-7}$$

where λ is the free space wavelength and θ is the angle of incidence of the light. Figure 2-2 explains the excitation of a BSW on the surface of a multilayer Bragg reflector. As light is made incident in the K-R configuration, it passes twice through the layer stack. A variation in the thickness of the last layer will result in breaking the periodicity inside the equivalent stack. This will form a cavity which will be resonant for a particular wavelength inside the band-gap. This resonance wavelength travels on the surface of the truncated stack if the angle of incidence is larger than the angle required for total internal reflection (TIR). The resonance wavelength or angle can be tuned by changing the thickness of the last layer.

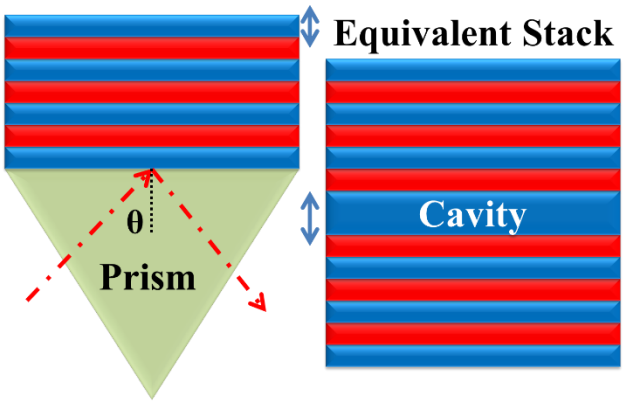

Figure 2-2: Sketch of the Bloch Surface Wave sensors showing the way it is excited using the Kretschmann-Raether (K-R) configuration along with the equivalent Bragg reflector considering the complete path of light. Blue and red colours in the diagram represent two materials having different refractive indices.

BSW have been demonstrated using two dimensional [25, 26], three dimensional [29] and more widely one dimensional photonic crystal structures (Bragg reflectors) using TiO_2/SiO_2 [30-34], Ta_2O_5/SiO_2 [35-41], Si_3N_4/SiO_2 [42-48] and porous Si [49-52] multilayers for refractive index [7-15], fluorescent sensing [53-58] and waveguiding applications [59-62]. Different measurement techniques like angular, spectral, intensity or phase interrogation have been proposed to enhance the performance of the reported sensors. The designs of a couple of TiO_2/SiO_2 BSW sensors already reported in the literature are discussed below. These sensors operate for different polarisations of light so it will help understanding the design of BSW sensors for both orthogonal polarisations. It should be mentioned here that presented field distributions and the reflection responses for the example structures from the literature were not copied but were re-simulated. I have used both transfer matrix method implemented in MATLAB (Appendix A & B) and the finite difference time domain (FDTD) methods for the simulations. Commercially available FDTD based simulator from Lumerical solutions was used and the scrip for calculations is available in Appendix A. The design of a high index contrast BSW-like sensor will be explained after explaining these couple of sensors.

A sensor (structure 'A') consisting of 20 layers of TiO_2 (n_H = 2.30) and SiO_2 (n_L = 1.434) with respective thicknesses of d_H = 163 nm and d_L = 391 nm sustains a TM-polarised BSW at the wavelength of 980 nm [23]. The final layer adjacent to the external

medium was 500 nm thick SiO_2. The calculated reflection response for an incident wavelength of 980 nm is shown in Figure 2-3(a) where water (n = 1.33) was used as the medium above the surface. Two resonance dips at incident angles of 53.4° and 65° can be observed in the reflection response having Full Width Half Maxima (FWHM) of 0.009° and 0.11° respectively. The calculated field distributions for these modes are shown in Figure 2-3(b). It can be noticed that the electric field for the resonance at 53.4° is confined at the surface of the dielectric stack. The calculated effective refractive index of the mode is 1.34 with a 1 μm penetration depth of the electric field (at 1/e) into the water. A significant part of the electric field for surface mode penetrates into the water, so a change in refractive index above the surface will result in shifting of the surface resonance. The electric field for the resonance at 65° on the other hand is buried inside the stack, so this mode is named as a Bloch sub-surface mode (BSSW). As the field is buried inside the stack so a change in refractive index above the surface will not affect the sub-surface wave. The effective index of the sub-surface wave was calculated to be 1.52, larger than surface wave as field is residing inside the stack instead of comparatively lower index water. The thickness of the last SiO_2 layer was changed to show the effect of this thickness on the resonances. The calculated resonances for a 480 nm, 500 nm and 520 nm thick last SiO_2 layer are shown in the inset of Figure 2-3(a). The sub-surface resonance is not affected by this variation while the surface resonance moves to larger angles with an increase in the thickness. This shows that the position of the surface wave resonance can be tuned by changing the thickness of the surface dielectric layer.

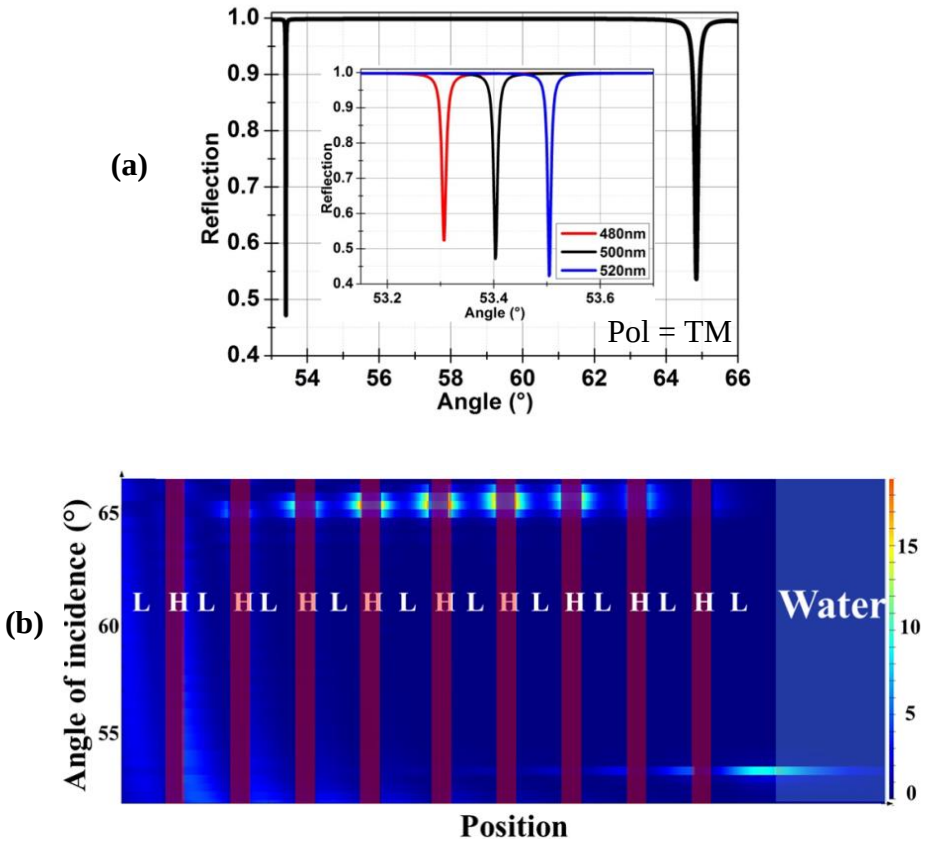

Figure 2-3: Calculated reflection response for structure 'A' having 10 pairs of TiO_2 / SiO_2 layers under plane wave excitation. Two resonances representing surface and sub-surface resonances are observed at angles of incidences of 53.4° and 65° respectively. The angles are quoted with respect to the surface normal in the substrate. The inset shows the shift in the surface resonance for different thicknesses of the surface SiO_2 layer. (b) Calculated field distributions at resonance (980 nm). High (TiO_2) and low (SiO_2) index layers are marked by H and L respectively. The field distribution shows that the resonance at 65° is due to a sub-surface mode with the electric field buried inside the dielectric stack.

A 5 layer sensor (structure 'B') using TiO_2 and SiO_2 with respective thicknesses of d_H = 96 nm and d_L = 140 nm was reported to sustain a TE-polarised BSW at the wavelength of 550 nm [24]. The surface of the multilayer adjacent to the external medium was a 34.6 nm thick TiO_2 layer. The BSW in this design was sustained for TE polarised light with the number of layers reduced from 20 to 5 using the same materials. The surface layer of the sensor was a high index layer in contrast to the low index layer for the previously discussed BSW. The calculated reflection response for this structure is shown in Figure 2-4(a). A shallow TE polarised resonance is calculated at an incident angle of

58° with air (n=1) above the surface. The FWHM of the resonance is calculated to be 0.78° which is larger than the earlier presented structure. The effective refractive index of the mode is only 1.29 as a significant portion of the field is residing inside the air. The electric field distribution at resonance is shown in Figure 2-4(b). The penetration depths of the electric field (at 1/e) are calculated to be 100 nm and 300 nm into air and water respectively. The penetration depth of this BSW into water is smaller than the previous one as the field is more tightly confined to the surface due to the high index terminating layer. Thus the use of a high index surface layer helps strongly confining the field at the surface.

(a)

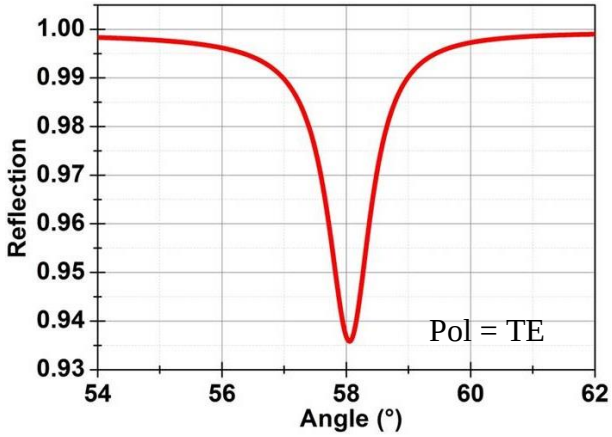

(b)

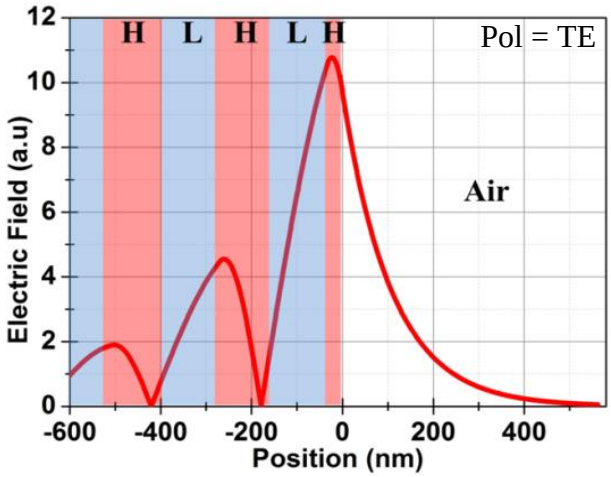

Figure 2-4: (a) Calculated reflection response for structure 'B' having 5 layers of TiO_2 and SiO_2 for operation at 550 nm wavelengths. Air was assumed above the surface for these calculations. The angles are quoted with respect to the surface normal in the BK7 substrate. (b) Calculated field distribution at resonance. High and low index layers are marked by H and L respectively.

2.3.2.1 Design of 2 layer BSW sensor

Learning from the above discussed structures, the number of layers were reduced to 2 using high (Si) and low (SiO_2) index dielectric layers on a sapphire substrate as shown in Figure 2-5(a). This structure is named as structure 'C' in the thesis. Used refractive index values for Silicon (Si), Silica (SiO_2) and sapphire were 3.67+0.03i, 1.47 and 1.77 respective at λ = 820 nm. The imaginary part in the refractive index represents the significant loss associated to Si at 820 nm. The internal angles within the individual layers needed in order to obtain a surface wave can be calculated using Snell's law. Quarter wave layer thicknesses of 60 nm and 327 nm were calculated using the equations below for Si and SiO_2 for an aqueous environment (n=1.33).

$$\boldsymbol{d_{Si} = \frac{\lambda}{4 * n_{Si} * Cos(\theta_{Si})} = 60nm} \quad \textbf{2-8}$$

$$\boldsymbol{d_{SiO2} = \frac{\lambda}{4 * n_{SiO2} * Cos(\theta_{SiO2})} = 327nm} \quad \textbf{2-9}$$

where values of the θ_{Si} and θ_{SiO2} were 21.3° and 65° respectively. The thickness of the high index silicon layer determines the position of the resonance inside the band-gap. Calculations show that a strong TM polarised mode is excited at an incident angle of 61° for λ = 820 nm using a 70 nm thick silicon layer. The resonance obtained has a full width at half maximum (FWHM) of 3.5°. This width can be reduced by increasing the number of mirror pairs at the expense of unacceptably high absorption in the Si or by increasing the thickness of the SiO_2 layer to 676 nm for the 2nd order mode which results in the FWHM of the resonance being 1°, Figure 2-5. It should be noticed that the FWHM is still high due to the loss associated to silicon at visible wavelengths. It will be shown later that sharper resonances can be achieved by operation around telecom wavelengths where silicon is transparent.

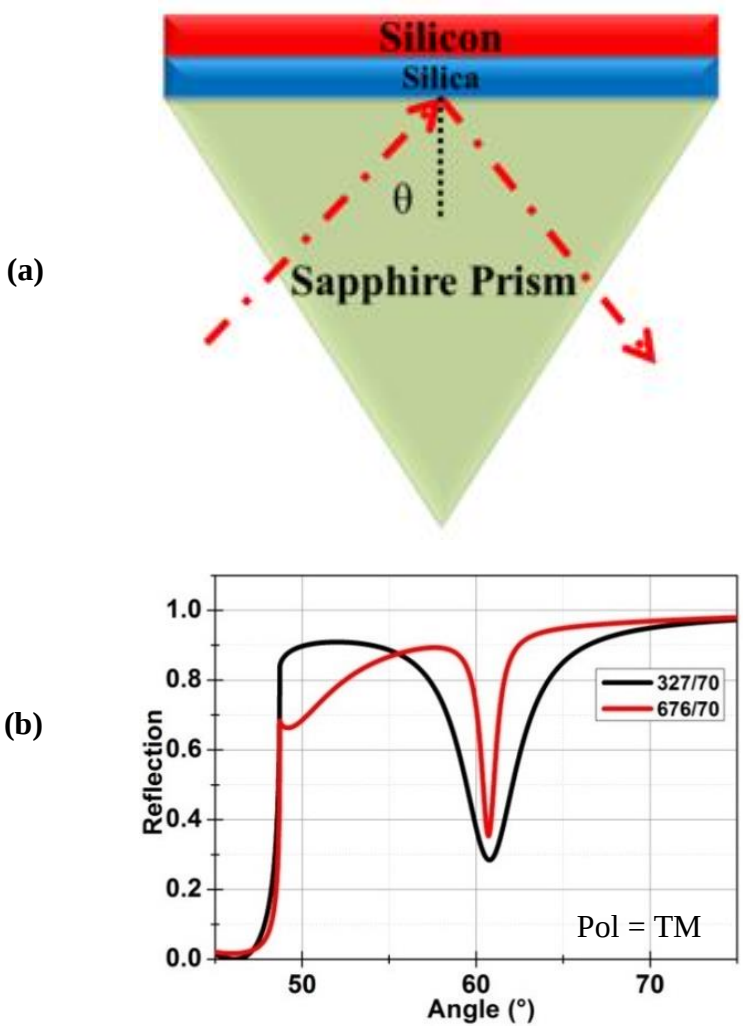

Figure 2-5: (a) A sketch showing the designed 2 layer sensor (structure 'C') with silicon and silica layers deposited on a sapphire substrate/prism. (b)Comparison of the reflection response for a 2-layer Si/SiO_2 BSW for 327 nm and 676 nm thick SiO_2 layers. A 70 nm thick Si layer was used for these calculations.

The effect of the silicon layer thickness on the resonance wavelength was studied by varying the silicon layer thickness from 40 nm to 140 nm. The angle of incidence and thickness of SiO_2 were fixed at 61° and 676 nm respectively. The 3D plot in Figure 2-6(a) shows that the reflection intensity at resonance is at a minimum for a 70 nm thick silicon layer at 820 nm supporting the earlier calculations. The effect of the silicon layer thickness on the resonance angle was also studied with the wavelength of incident light fixed at 820 nm. The 3D plot in Figure 2-6(b) confirms that the strongest resonance will be observed for 70 nm thick silicon layer at a resonance angle of 61°.

(a)

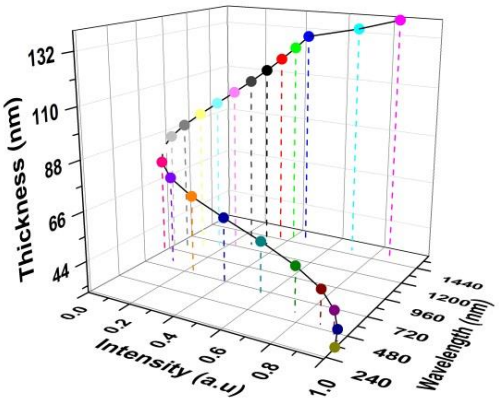

(b)

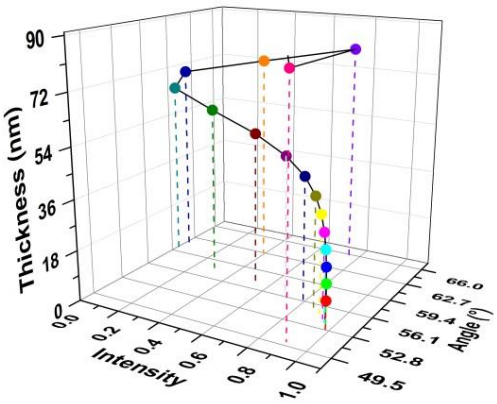

Figure 2-6: (a) 3D graph shows that the resonance depth is maximum (intensity minimum) for a Si layer thickness of 70 nm on 676 nm SiO_2 for operation at 820 nm. The angle of incidence for the calculations was fixed at 61°. (b) 3D graph shows that strongest resonance is observed for Si thickness of 70 nm at a resonance angle of 61°.

So, 676 nm and 70 nm thick layers of SiO_2 and Si were used to calculate the wavelength and angle dependent reflections shown in Figure 2-7. The shift in the resonance angle and wavelength for a change in the refractive index of $\Delta n = 0.04$ in the overlying medium, as appropriate to isopropyl alcohol (IPA), was calculated to be $\Delta\theta = 1.09°$ for $\lambda = 820$ nm and a shift of $\Delta\lambda = 36$ nm for $\theta = 61°$. Thus, the calculated bulk sensitivities are 900 nm/RIU (refractive index unit) and 27.3°/RIU.

(a)

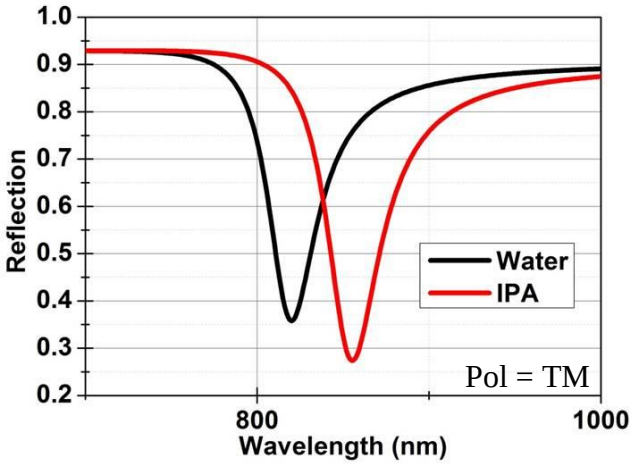

(b)

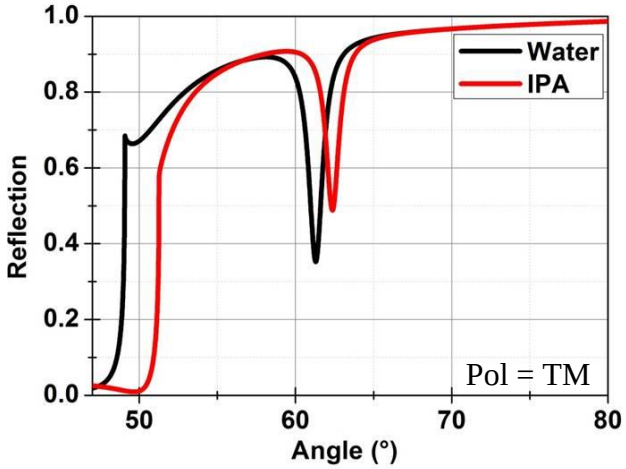

Figure 2-7: (a) Calculated wavelength dependent reflections for the structure 'C' for an angle of incidence of 61° in both water (n=1.33) and IPA (n=1.37) environments. (b) Calculated angle dependent reflection response for 820 nm incident light. Water (n=1.33) and IPA (n=1.37) were used to calculate the expected shift in the resonance for a change of Δn=0.04 above the surface. The inset shows the calculated field distribution for the BSW at resonance.

The field distributions of the excited mode for both on (61°) and off (70°) resonance are presented in Figure 2-8(a). Only a small portion of the power resides inside the silicon layer showing that the mode is evanescent. At resonance, the penetration depth (at 1/e) of the electric field into water (n=1.33) is 150 nm. This strong confinement of the field to the surface makes this sensor very suitable for label free detection of biological analytes. The mode profiles were compared with those obtained for a multilayer BSW, a SPR and for a non-resonant silicon-on-insulator (SOI) guided mode, Figure 2-8(b-d). In

all cases, water (n = 1.33) was used as the environment above the sensors for the calculations.

The multilayer BSW sensor (structure ‘D’) was designed to have a resonance at 820 nm and consisted of 5 pairs of high index TiO_2 (n=2.3+0.0002i) and low index SiO_2 (1.44) [13] layers with respective thicknesses of 137 nm and 328 nm. The thickness of the surface SiO_2 layer was 420 nm. The calculated BSW mode had an effective index of 1.34 with a 750 nm penetration depth into the water. The comparison in Figure 2-8(b) shows that the field for the high index contrast sensor is more tightly confined to the surface because of the high index (Si) top layer.

The SPR mode discussed in the SPR section with an effective index of 1.38 and a penetration depth of 375 nm into the water is also compared. I have named this structure as structure ‘E’ in this chapter. The comparison in Figure 2-8(c) shows that electric field for the high index contrast sensor is more tightly confined to the surface than a SPR sensor.

The SOI waveguide mode for a 260 nm thick Si layer (structure ‘F’) as shown in [63] at a wavelength of 1550 nm was simulated for comparison. The calculated field distributions show that the TM polarised mode is a guiding mode with equal penetration depth to our sensor. The broadband waveguide mode has an effective refractive index of 2.37 as most of the power is residing inside the high index silicon core. Note that the waveguide mode is non-resonant and lateral structuring is required to make a resonant structure for sensing. In contrast, the layered structure directly provides the resonance that can be used to monitor local refractive index changes. This presence of the resonance makes bi-layer sensor a Bloch surface wave sensor separating it from a simple waveguide as a waveguide is broadband and no resonance is observed for a waveguide.

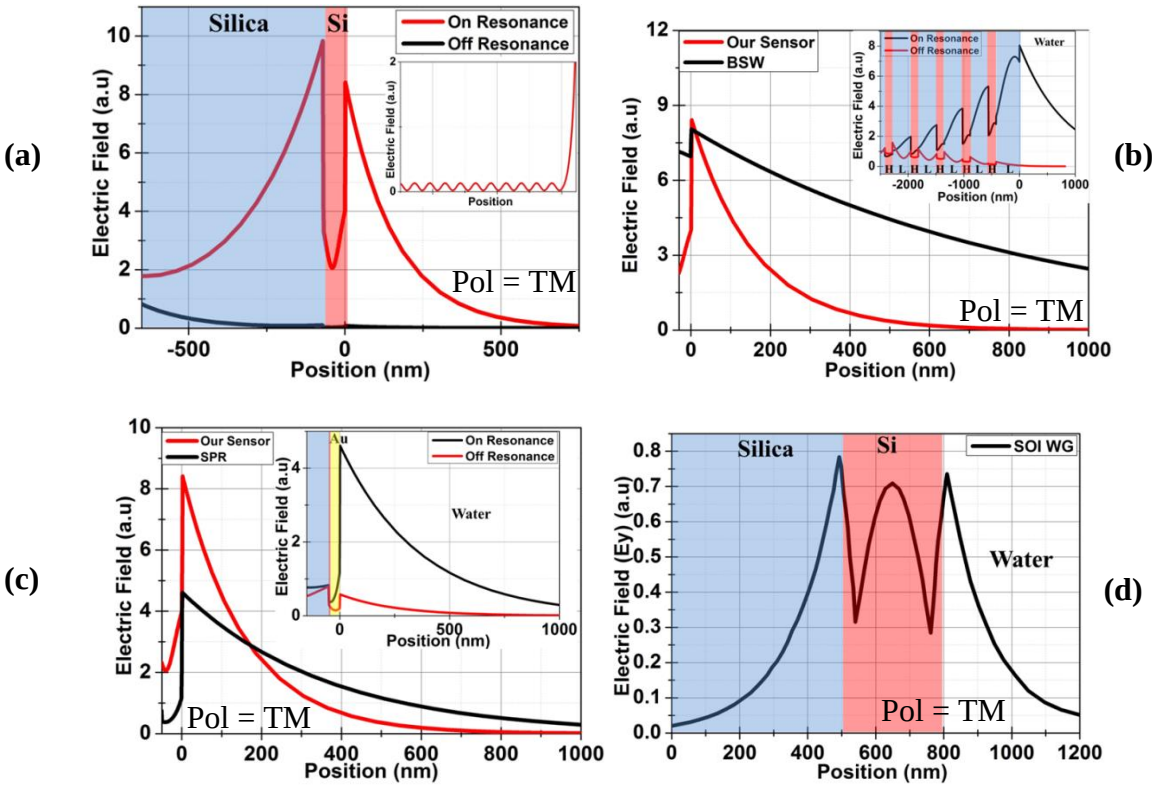

Figure 2-8: (a) Calculated field distributions for the designed sensor (structure 'C') mode at a wavelength of 820 nm on-resonance at 61° (red) and off-resonance at 70° (black). The inset shows that the excited mode is lossy as energy is leaking into the sapphire substrate. (b) A comparison between the calculated field distributions for a multilayer (TiO_2/SiO_2) BSW structure (structure 'D') at an angle of 53.5° (black) and our high index contrast sensor (structure 'C') at 61° (red). The inset shows the calculated field distribution inside the TiO_2/SiO_2 stack. High and low index layers are marked with letters H and L respectively. (c) A comparison between the calculated electric field for the SPR mode (structure 'E') at 72° (black) and the high index contrast (structure 'C') sensor (red). The inset shows the calculated field distributions for the SPR. (d) The calculated field distribution for the TM guided mode at a wavelength of 1550 nm in a 260 nm thick SOI layer (structure 'F')as used in [63].

The calculated parameters for the simulated structures explained above are summarised in Table 1. It should be noticed that typical structures are discussed as the evanescent field can be further engineered in the above mentioned sensors. Also that, I am just comparing the field penetration depth and the effective index of the mode to show that excited mode is an anti-guided BSW like mode with small portion of light residing inside the silicon which is in contrast to the silicon guided SOI mode which has larger effective index as most of the light is residing inside the high index silicon.

Sensor Type	Lateral structuring	N_{eff} of the mode	Penetration depth of electric field
High index contrast (Structure 'C')	Not required	1.54	150 nm
BSW – TM [23] (Literature, Structure 'A')	Not required	1.34	1000 nm
BSW – TE [24] (Literature, Structure 'B')	Not required	1.4	300 nm
SPR (Structure 'E')	Not required	1.38	375 nm
SOI Waveguide (Structure 'F') [63]	Required	2.37	150 nm

Table 1: Comparison between different refractive index sensors.

A tolerance analysis for the sensor was performed and it was found that a small change (± 10 nm) in the thickness of the SiO_2 layer does not significantly affect the resonance wavelength. The resonance is more sensitive to the thickness of the high index Si layer. The calculations show a 115 nm shift in resonance wavelength for a 10 nm variation in the thickness of the silicon layer as shown in Figure 2-9(a). The calculated resonances for different loss values of silicon are shown in Figure 2-9(b). An increase in the loss makes the resonance wider and shallower. So, smaller losses are desired for a sharp and prominent resonance. As the roughness of the surface will result in additional scattering loss, a smooth dielectric surface is desired. An increase in the nominal refractive index of the SiO_2 layer while keeping the refractive index of silicon constant results in the resonance moving to longer wavelengths, Figure 2-9(c). The resonance becomes broader with an increase in index due to it being off-resonance. The change in angle of incidence results in moving away from the resonance condition which will result in a shallow resonance.

(a)

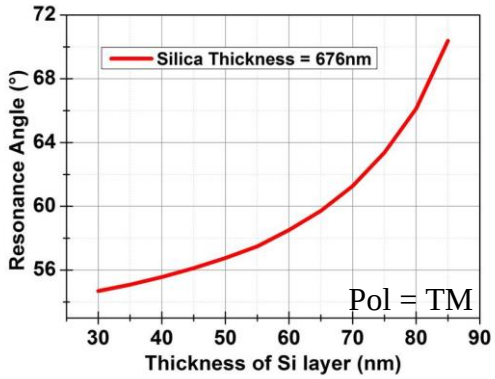

(b)

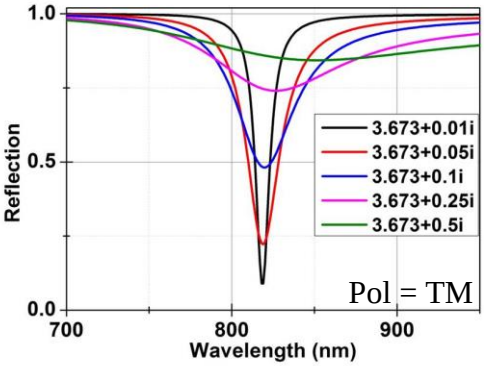

(c)

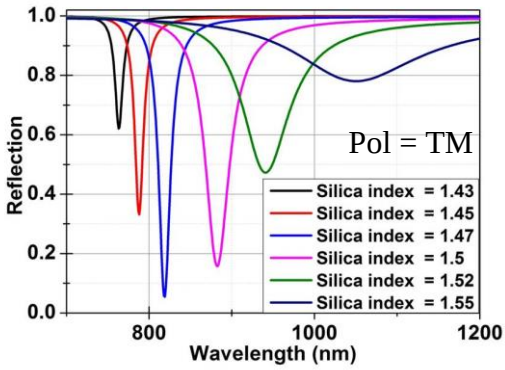

Figure 2-9: (a) Calculated resonance angles at λ = 820 nm for change in thicknesses of the silicon layer. The thickness of the SiO_2 layer was set at 676 nm. (b) Calculated responses for different values of the loss associated with the silicon layer. The resonance gets broader and shallower with an increase in the loss. (c) Calculated responses for small variation in refractive index value of the silica layer. Increase in index shifts the resonance to larger wavelengths.

2.3.2.1.1 Design for Telecom wavelengths

The single pair high index contrast structure can be designed to be resonant at a desired wavelength and polarisation state. The structure was designed for operation around 1550 nm wavelengths where silicon is transparent and the silicon on insulator (SOI) platform is widely used for photonic integrated circuits. A conventional (2 µm thick SiO_2) SOI arrangement was simulated with a silicon substrate rather than sapphire as silicon is transparent for these wavelengths allowing access through the substrate.

It is shown using simulations that both TE and TM polarised resonances can be excited for different thicknesses of the silicon layer. Refractive index values of 3.48 and 1.47 are used for Si and SiO_2 respectively. The variation of the resonance angle for both TE and TM polarised light with different thicknesses of Si are shown in Figure 2-10(a) for both water (dotted lines) and air (solid lines) above the surface. Resonances with FWHM around 0.003° are calculated which is due to the zero loss assumed for the layer materials.

The mode profile for the 1st TE mode is shown in Figure 2-10(b). It should be noticed that silicon thickness ranging from 10 nm to 75 nm will result into a TE mode as shown by the blue graph in Figure 2-10(a). This mode is calculated for 40 nm thick silicon layer with air above the surface. This mode is similar to the earlier discussed TE-polarised mode for the 5 layer TiO_2/SiO_2 structure.

The black graph in Figure 2-10(a) shows that silicon thickness ranging from 100 nm to 210 nm will result into 1st TM mode. The field distribution for the 1st TM polarised mode calculated for 170 nm thick silicon layer with air above the surface is shown in Figure 2-10(c). The mode is an evanescent mode with an effective refractive index of 1.524. The sensitivity of the resonance was calculated by changing the overlying medium with a 133 nm thick silicon layer. This silicon thickness of 133 nm was selected to get a strong resonance with water above the surface. The refractive index above the surface was changed from 1.33 (water) to 1.47 (IPA). It can be noticed in Figure 2-10(d) that resonance moves from 1550 nm to 1630 nm for a bulk refractive index change of 0.04 resulting into a calculated bulk sensitivity of 2000 nm/RIU. The calculated field distribution at resonance for water above the surface is shown in the inset of Figure

2-10(d). The penetration depth of the electric field into the water is 300 nm. The resonance can also be excited by grating coupling or tapered waveguide coupling techniques as are used in silicon photonics.

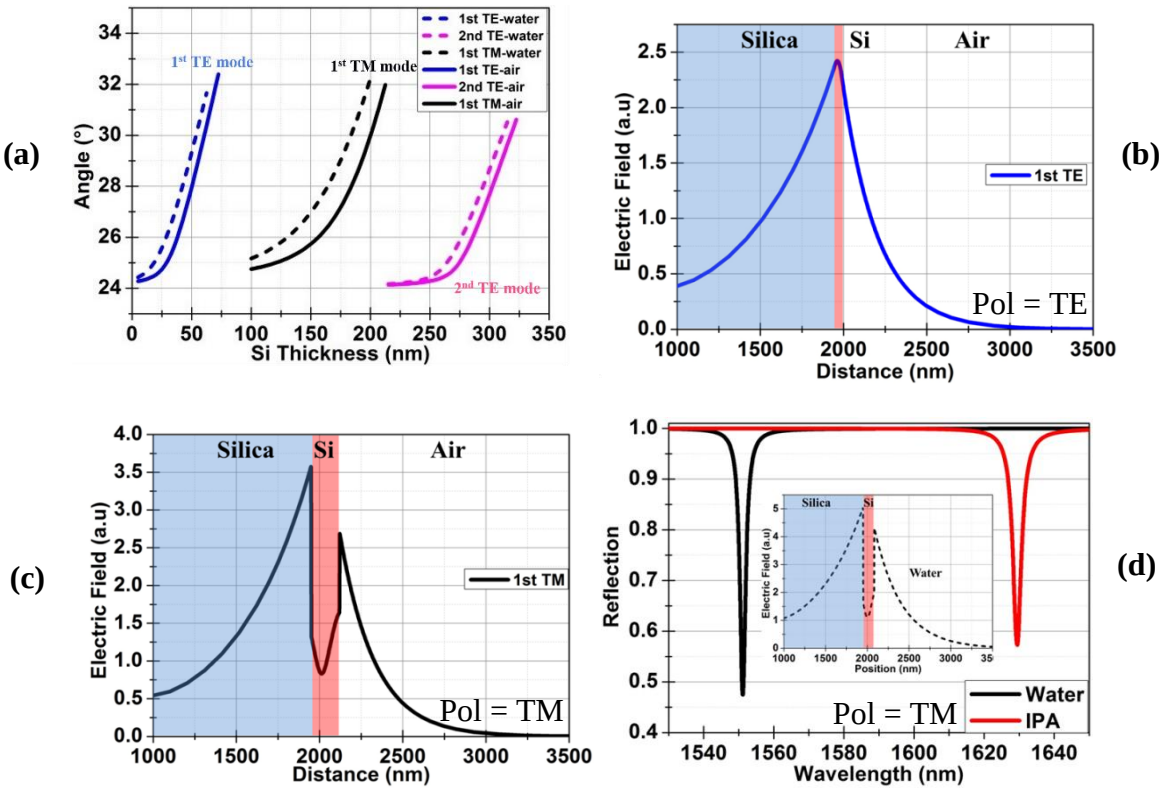

Figure 2-10: (a) Calculated BSW enhanced TE and TM modes for a wavelength of 1550 nm on SOI. The thickness of the SiO_2 layer is 2000 nm. The angles are quoted with respect to the surface normal in Si substrate. (b) Electric field of the fundamental TE mode guided by a 40 nm thick silicon layer at an angle of 26° (c) Electric field of fundamental TM mode calculated for 170 nm thick silicon layer at an angle of 26.35°. (d) Calculated wavelength dependent reflection in both water (n=1.33) and IPA (n=1.37) environments. The inset shows the calculated electric field of fundamental TM mode using 133 nm thick silicon layer at an angle of 26.1°. Water was used as the overlying medium for this calculation.

2.3.3 BSW based sensors from literature

Size-selective sensing of molecules in a label-free manner was demonstrated using a 21 layer thick porous-silicon based sensor [34, 35]. The BSSW described earlier, confined inside but near the top of the structure, was used to sensitively detect small molecules (0.8 nm) that could infiltrate the surface. The BSW being confined at the surface was used to sense larger (60 nm) immobilised analytes. The small molecules infiltrated the top surface of the sensor and resulted in shifting of the sub-surface modes. A BSSW sensitivity of 72 °/RIU (Refractive index unit) or 2038 nm /RIU was reported. A BSW sensitivity of 31°/RIU or 967 nm/RIU was reported for the large molecules.

An intensity interrogation was used to improve the performance of a 20 layer TiO_2/ SiO_2 BSW sensor [23]. An angular sensitivity of 41 °/RIU was demonstrated using different concentrations of glycerol above the sensor surface. This reported sensitivity was comparable to SPR sensors [8]. The authors fixed a resonant angle and measured the change in intensity at that angle of incidence for different concentrations of glycerol above the surface. These measurements for the same sensor demonstrated better intensity sensitivities than SPR sensors due to the sharpness of the BSW resonance. They reported an intensity sensitivity of 156 /RIU [43] with a limit of detection as low as 7.5×10^{-7} RIU significantly better than the gold SPR sensors having a sensitivity of 24 /RIU [26].

A sensing platform capable of working simultaneously in a label-free and in a fluorescence mode was reported using a 9 layer Ta_2O_5 and SiO_2 based structure [37]. Concerning the label-free operation, the reflectance was measured above the total internal reflection edge for known concentrations of glucose in doubly ionized water to show an angular sensitivity of S_{BSW} = 14.7 °/RIU. The structure was designed to sustain a TE polarised resonance around 804 nm. The reported sensitivity was much smaller than the reported SPR and other BSW sensitivities. However, a Figure of Merit (FoM) was defined as

$$\boldsymbol{FoM = S * \frac{D}{W}} \qquad \textbf{2-10}$$

where S is the sensitivity, D is the depth of the resonance and W represents the width of the resonance dip. The sensor was demonstrated to have a FoM_{BSW} = 82 / RIU, better than the SPR sensors having a FoM_{SPR} = 48 / RIU. In the fluorescence mode, the surface of the sensor was labelled with dye molecules and excited by an external laser beam. The emission was dependent on the refractive index of the surface layer and was preferentially emitted into the substrate where it could be collected. Luminescent/fluorescent detection was also demonstrated using an 8-layer Ta_2O_5/SiO_2 structure designed for a TE polarized resonance in the visible range [25]. The enhanced luminescence emission from the last SiO_2 layer terminating the reflector was due to the near-field enhancement. The measurement was defined as label-free since the luminescence concerned with the photonic structure itself rather than a specifically labelled analyte. The reported sensitivity for this sensor was 2500 nm/RIU with a limit of detection as low as $3x10^{-6}$ RIU.

Phase detection was used to enhance the performance of a 5-layer TiO_2 and SiO_2 based sensor because the phase of the reflected light from the BSW sensor changes rapidly as the excitation of BSW occurs [24]. Variable angle spectroscopic ellipsometry was used for both the angular interrogation and phase detection. Different concentrations of NaCl in water were used to demonstrate an angular sensitivity of 40 °/RIU with a LoD of about 1.2×10^{-4} RIU. The calculated phase sensitive sensitivity of the sensor was 6.6×10^3 °/RIU, higher than the angular sensitivity.

Table 2 below compares the attributes of a selection of reported BSW sensors.

No. of layers	Material (H/L)	Operating Wavelength	Sensitivity		Reference
21	Porous Silicon	1550 nm	BSSW	72 °/RIU or 2038 nm/RIU	[51]
			BSW	31 °/RIU or 967 nm/RIU	
20	Silicon Alloy	1550 nm	1100 nm/RIU		[21]
20	TiO_2/SiO_2	980 nm	Resonance Shift	41 °/RIU	[33]
			Intensity Interrogation	BSW - 156/RIU SPR - 24/RIU	
9	Ta_2O_5/SiO_2	804 nm	14.7 °/RIU		[41]
9	Si_3N_4/SiO_2	632 nm	40 °/RIU		[42]
8	TiO_2/SiO_2	632 nm	>1000 nm/RIU		[31]
8	Ta_2O_5/SiO_2	543 nm	Theoretical = 40 °/RIU		[23]
			Experimental = 18 °/RIU		
8	TiO_2/SiO_2	467 nm	600 nm/RIU		[32]

Table 2: A comparison between BSW based sensors.

2.3.3.1 Experimental demonstration of 2 layer BSW sensor

After presenting the results for different reported BSW sensors, I am explaining the fabrication and experimental characterisation of the designed 2 layer Si/SiO_2 based platform. The designed thicknesses of 70 nm and 676 nm for Si and SiO_2 respectively were deposited by electron beam evaporation on a 2 inch double-side polished sapphire wafer. Atomic Force Microscopy (AFM) measurements showed that surface roughness of the layers was less than a nanometre. The wafer was diced into 2 cm square pieces and attached to a 45° dove shaped sapphire prism with Durimide 112A as an index matching polymer.

The K-R configuration was used to excite the resonance as a function of wavelength which was preferred over angle dependent measurements because of the simplicity of the characterisation setup. A white light source (Ocean Optic HL2000) was collimated and polarised in the desired TM orientation. A microfluidic delivery system was mounted on the sensor enabling the flow of different fluids over the surface. The flow rate was maintained at 25 µl/minute. The fabricated sensor was placed at the calculated resonance angle of 61° for measurements. The reflected light from the sensor was coupled to a fibre using a lens and detected by a spectrometer (Ocean Optic USB4000). A resonance was observed at the designed wavelength of 820 nm. The FWHM of the resonance was measured to be ~ 23 nm. Solutions having different refractive index values were prepared by mixing different percentages of IPA (20, 40, 60 and 80%) in DI water. These solutions were injected into the microfluidic channel and the resonance shift measured. The resonance was found to shift to larger wavelength values with increasing concentration of IPA in DI water. The relation between the increase in concentration and shift in the resonance wavelength was found to be linear. A resonance shift of $\Delta\lambda = 36$ nm was measured for a refractive index change of $\Delta n = 0.04$ i.e. changing the fluid from pure DI water having an index of 1.33 to pure IPA having an index of 1.37. A good agreement was found between the experimentally measured and calculated resonances as shown in Figure 2-11(b). The wavelength sensitivity of the sensor was experimentally found to be 900 nm per RIU. The sensitivity of the sensor can be increased by improving the design and selection of the materials.

(a)

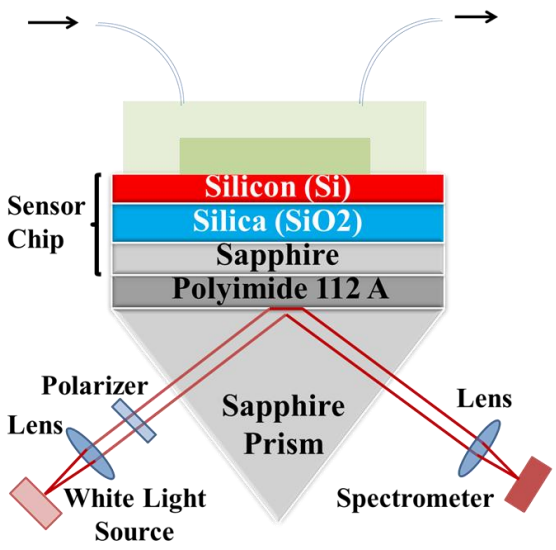

(b)

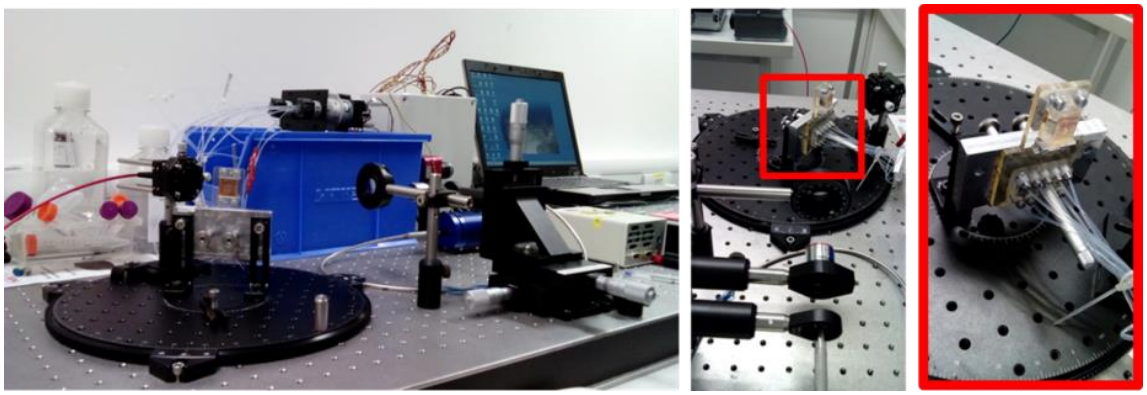

(c)

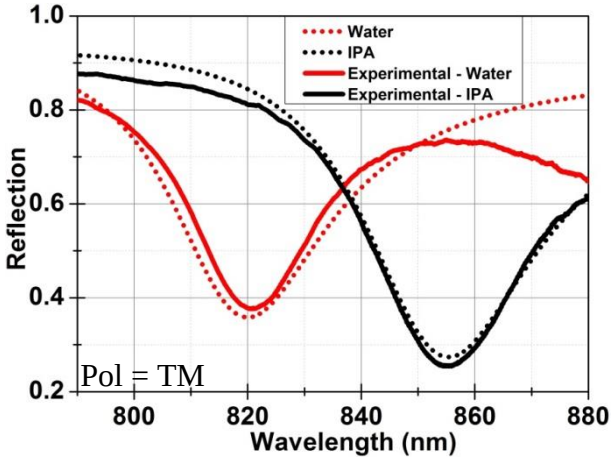

Figure 2-11: (a) Sketch showing the setup used for the measurements. The chip was attached to the sapphire prism using index matching polymer Durimide 112A. (b) Picture of the measurement setup in the lab. (c) Calculated (continuous lines) and experimentally measured (dotted lines) reflectance spectra for a high index contrast sensor with water and IPA environments.

2.3.4 Waveguide coupled resonance

A new approach based on a waveguide coupled BSW resonance is proposed here as a means to avoid the use of the prism. A dual layer Si / SiO_2 with thicknesses of 70 nm and 676 nm (as discussed earlier) are to be deposited on a deep etched waveguide which will be excited by end fire coupling for excitation of BSW-like resonance at 820 nm wavelength. As the structure was originally designed for TM polarised light only, so dielectric layers are proposed to be deposited on the top surface of the waveguide as shown in Figure 2-12(a). TM polarised light has its electric field perpendicular to the deposited layers and will result in excitation of the surface wave. The BSW will only be excited if the effective index of the waveguide mode matches.

Simulations are performed to demonstrate the working of this waveguide coupled structure. SU8 having a refractive index of 1.585 is chosen as waveguide material because it is easy to process and is suitable for waveguide applications. The waveguides will be fabricated on a glass substrate as glass has smaller refractive index than SU8. The refractive index of the polymer should be larger than substrate to prevent coupling of the light to the substrate. A 2.5 µm x 2.5 µm waveguide will achieve a waveguide mode with effective index of 1.54 (i.e. to match the effective index of the BSW). The calculated transmission response for the structure shown in Figure 2-12(a) is shown in Figure 2-12(b) for TM polarised light. Water was used as the overlying medium for the calculations. A resonance dip at wavelength around 770 nm can be observed. Electric field was calculated to be sure that the resonance dip was actually due to the surface wave at this wavelength. The calculated electric field is shown in Figure 2-12(c). A surface wave having electric field concentrated at the silicon surface and decaying away from the silicon can be observed for an incident wavelength of 770 nm. This confirms that BSW-like resonance demonstrated earlier using the Kretschmann-Raether configuration can also be excited using a polymer waveguide. The waveguide will be excited using the end-fire coupling which will help eliminating the bulky prisms used for K-R configuration.

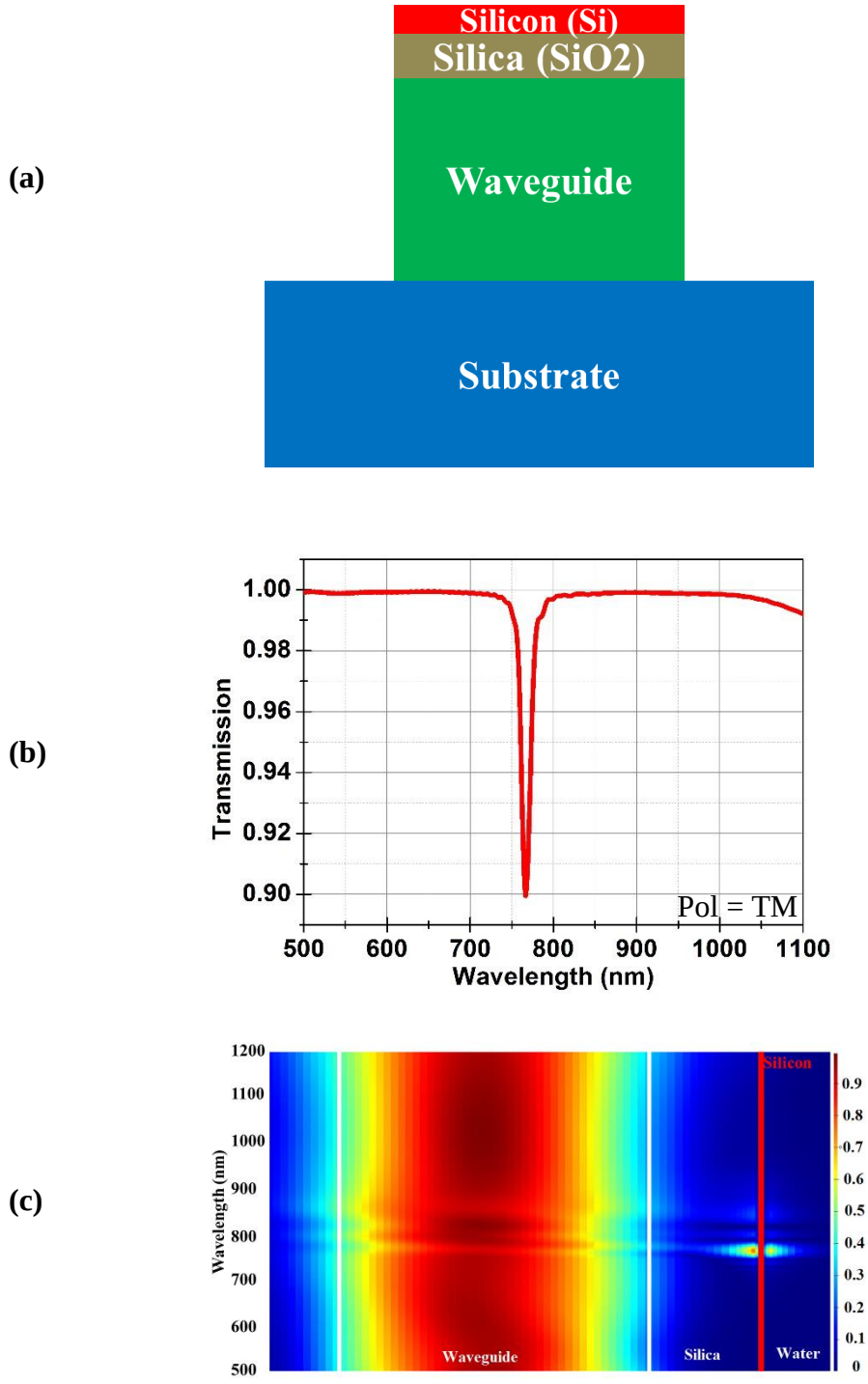

Figure 2-12: (a) Schematic of proposed waveguide coupled structures using deposition of the resonant structure on the top surface of the waveguide. The resonance can only be excited by TM polarized light. (b) Calculated transmission for TM polarised light showing a resonance dip at 770 nm wavelength. (c) Calculated electric field confirms that the resonance dip is due to the surface wave excited at a wavelength of 770 nm.

Calculations have confirmed that the proposed design will help achieving on-chip sensing of different analytes. Waveguide coupled resonances will be demonstrated in chapter 3.

2.4 Conclusions and discussion

To conclude, a high index contrast sensing surface using silicon on silica on sapphire is proposed and experimentally demonstrated. The sensor was designed by initially decreasing the number of dielectric layers using relatively low index contrast materials ZrO_2 and SiO_2. The index contrast was later increased by using Si and SiO_2 as low and high index materials respectively. Silicon was selected as high index material due its availability and high index value. Considerable losses for silicon around 820 nm wavelengths were a negative point but the ultimate goal is to operate the sensor around telecom wavelengths with possibilities of active guiding by doping of silicon. Silicon, being high index terminating layer, helped reducing the penetration depth into water to 150 nm. A similar structure using only a couple of layers (resonant mirror) was reported in 1993 but a resonance in the transmission response has not been reported to date and phase change in the reflection was used for measurements. The presence of a resonance dip in the reflection for the demonstrated sensor distinguishes it from the resonant mirror. The demonstrated sensitivities (900 nm/RIU) are compared with already reported BSW sensitivities and novel waveguide coupled BSW resonances are proposed at the end. The waveguide coupled resonances are experimentally demonstrated in chapter 3.

It is found that the sensor is very sensitive to the thickness of the silicon layer. A 10 nm variation in thickness of the silicon layer results in 115 nm shift in the resonance. The silicon layer should therefore be carefully/accurately deposited for operation at the desired wavelength. Simulations show that a substrate with index larger than 1.6 is required for matching of the wave vector. For the demonstrated sensor, sapphire was selected as the substrate and the prism material for matching of the wave vector.

2.5 References

[1] D.W. Lubbers, N.Opitz, “Eine neue pCO2-bzw: pO2-Messonde zur Messung des pCO2 oder pO2 von Gasen und Flu¨ ssigkeiten,” Zeitschrift Fu¨ r Naturforschung C30, 532-533 (1975).

[2] J. Homola, S. S. Yee, and G. Gauglitz, “Surface plasmon resonance sensors: review,” Sens. Actuators B Chem 54(1-2), 3–15 (1999).

[3] J. Homola, “Surface plasmon resonance sensors for detection of chemical and biological species,” Chem. Rev. 108(2), 462–493 (2008).

[4] R. Cush, J. M. Cronin, W. J. Stewart, C. H. Maule, J. Molloy, and N. J. Goddard, “The resonant mirror: a novel optical biosensor for direct sensing of biomolecular interactions Part I: Principle of operation and associated instrumentation,” Biosens. Bioelectron. 8, 347-353 (1993).

[5] H. N. Daghestani, B. W. Day, “Theory and applications of surface plasmon resonance, resonant mirror, resonant waveguide grating, and dual polarization interferometry biosensors,” Sensors 10(11), 9630-9646 (2010).

[6] E. Kretschmann, and H. Raether, “Radiative decay of non radiative surface plasmons excited by light,” Z. Naturforsch **23a**, 2135-2136 (1968).

[7] H. Raether, Surface plasmons on smooth and rough surfaces and on gratings (Springer-Verlag, 1988).

[8] I. Pockrand, J.D.Swalen., J.G. Gordon, M.R. Philpott, “Surface plasmon spectroscopy of organic monolayer assemblies,” Surface Sci. 74, 237–244 (1978).

[9] J.G. Gordon II, S. Ernst, “Surface plasmons as a probe of the electrochemical interface,” Surface Sci. 101, 499-506 (1980).

[10] C. Nylander, B.Liedberg, T. Lind, “Gas detection by means of surface plasmons resonance,”. Sens. Actuators B Chem **3**, 79–88 (1982).

[11] B. Liedberg, C. Nylander, I. Lundstrom, “Surface plasmons resonance for gas detection and biosensing,” Sens. Actuators B Chem **4**, 299–304 (1983).

[12] B. Liedberg, C. Nylander, I. Lundstro¨m, “Biosensing with surface plasmon resonance—how it all started,” Biosens. Bioelectron. **10**, i–ix (1995).

[13] V. Owen, “Real-time optical immunosensors - A commercial reality,” Biosens. Bioelectron. **12,** i-ii (1997).

[14] M. Piliarik, J. Homola, “Surface plasmon resonance (SPR) sensors: approaching their limits?,” Opt. express **17**(19), 16505-16517 (2009).

[15] S. Roh, T. Chung, and B. Lee, “Overview of the characteristics of micro and nano-structured surface plasmon resonance sensors,” Sensors (Basel) **11**(2), 1565-1588 (2011).

[16] C. Zhao, J. Zhang, “Plasmonic demultiplexer and guiding,” ACS Nano **4**(11), 6433-6438 (2010).

[17] W. M. Robertson, “Experimental measurement of the effect of termination on surface electromagnetic waves in one-dimensional photonic bandgap arrays,” J Lightwave Technol. **17**(11), 2013-2017 (1999).

[18] V. N. Konopsky, E.V. Alieva, “Long-range propagation of plasmon polaritons in a thin metal film on a one-dimensional photonic crystal surface,” Phys Rev Lett. **97**(25), 253904 (2006).

[19] M. Shinn and W. M. Robertson, “Surface plasmon-like sensor based on surface electromagnetic waves in a photonic band-gap material,” Sens. Actuators B Chem. **105**(2), 360-364 (2005).

[20] P. Yeh, A. Yariv, C. S. Hong, “Electromagnetic propagation in periodic stratified meida. I. General theory,” J. Opt. Soc. Am. **67**, 423-438 (1977).

[21] F. Giorgis, E. Descrovi, C. Summonte, L. Dominici, and F. Michelotti, “Experimental determination of the sensitivity of Bloch surface waves based sensors,” Opt. Express **18**(8), 8087-8093 (2010).

[22] V. N. Konopsky, T. Karakouz, E. V. Alieva, C. Vicario, S. K. Sekatskii, G. Dietler, “Photonic crystal biosensor based on optical surface waves,” Sensors (Basel) **13**(2), 2566-2578 (2013).

[23] A. Sinibaldi, R. Rizzo, G. Figliozzi, E. Descrovi, N. Danz, P. Munzert, A. Anopchenko, F. Michelotti, "A full ellipsometric approach to optical sensing with Bloch surface waves on photonic crystals," Opt. Express **21**(20), 23331-23344 (2013).

[24] P. Yeh, A. Yariv, and A.Y. Cho, "Optical surface waves in periodic layered media" Appl. Phys. Lett. **32**(2), 104-105 (1978).

[25] R. D. Meade, K. D. Brommer, A. M. Rappe, J. D. Joannopoulos, "Electromagnetic Bloch waves at the surface of a photonic crystal," Phy. Rev. B **44**(19), 10961-10964 (1991).

[26] W. M. Robertson, G. Arjavalingam, R. D. Meade, K. D. Brommer, A. M. Rappe, J. D. Joannopoulos, "Observation of surface photons on periodic dielectric arrays," Opt Lett. **18**(7), 528-530 (1993).

[27] Ballarini, M., et al., "*Bloch surface waves-controlled emission of organic dyes grafted on a one-dimensional photonic crystal,"* Appl. Phys. Lett. **99**(4), 043302 (2011).

[28] J. Gao, A. M. Sarangan, Q. Zhan, "Polarization multiplexed fluorescence enhancer using a pixelated one-dimensional photonic band gap structure," Opt Lett. **37**(13), 2640-2642 (2012)

[29] S. Y. Su, L. Tang, T. Yoshie, "Optical surface Bloch modes of complete photonic bandgap materials as a basis of optical sensing," Opt. Lett. **36**(12), 2266-2268 (2011).

[30] A. Pokhriyal, et al., "Multicolor fluorescence enhancement from a photonics crystal surface," Appl. Phys. Lett. **97**(12), (2010).

[31] Y. Guo, J. Y. Ye, C. Divin, B. Huang, T. P. Thomas, J. R. Baker, T. B. Norri, "Real-time biomolecular binding detection using a sensitive photonic crystal biosensor," Anal. Chem. **82**, 5211-5218 (2010).

[32] A. Farmer, A. C. Friedli, S. M. Wright, and W. M. Robertson, "Biosensing using surface electromagnetic waves in photonic band gap multilayers," Sens. Actuators B Chem. **173**, 79–84 (2012)

[33] W. Kong, Z. Zheng, Y. Wan, S. Li, and J. Liu, "High-sensitivity sensing based on intensity-interrogated Bloch surface wave sensors," Sens. Actuators B Chem. **193**, 467–471 (2014).

[34] Y. Li, T. Yang, Z. Pang, G. Du, S. Song, S. Han, "Phase-sensitive Bloch surface wave sensor based on variable angle spectroscopic ellipsometry," Opt. Express **22**(18), 21403-21410 (2014).

[35] V. N. Konopsky, E. V. Alieva, "A biosensor based on photonic crystal surface waves with an independent registration of the liquid refractive index," Biosens Bioelectron, **25**(5), 1212-1216 (2010).

[36] E. Descrovi, F. Frascella, M. Ballarini, V. Moi, A. Lamberti, F. Michelotti, F. Giorgis, C. F. Pirri, "Surface label-free sensing by means of a fluorescent multilayered photonic structure," Appl. Phys. Lett. **101**(13), 131105 (2012).

[37] A. Sinibaldi, N. Danz, E. Descrovi, P. Munzert, U. Schulz, F. Sonntag, L. Dominici, F. Michelotti, "Direct comparison of the performance of Bloch surface wave and surface plasmon polariton sensors," Sens. Actuators B Chem. **174**, 292-298 (2012).

[38] E. Descrovi, et al., "Leakage radiation interference microscopy*,"* Opt Lett, **38**(17), 3374-3376 (2013).

[39] F. Michelotti, A. Sinibaldi., P. Munzert, N. Danz,E. Descrovi, "Probing losses of dielectric multilayers by means of Bloch surface waves," Opt Express 38(5), 616-619 (2013).

[40] A. Angelini, et al., "Focusing and extraction of light mediated by Bloch surface waves," Sci Rep. **4,** 5428 (2014).

[41] A. Angelini, A. Lamberti, S. Ricciardi, F. Frascella, P. Munzert, N. De Leo, and E. Descrovi, "In-plane 2D focusing of surface waves by ultrathin refractive structures," Opt. Lett. **39**(22), 6391-6394 (2014).

[42] V. Paeder, V. Musi, L. Hvozdara, S. Herminjard, and H. P. Herzig, "Detection of protein aggregation with a Bloch surface wave based sensor," Sens. Actuators B Chem. **157**(1), 260–264 (2011).

[43] M. Ballarini, F. Frascella, E. Enrico, P. Mandracci, N. D. Leo, F. Michelotti, F. Giorgis, E. Descrovi, "Bloch surface waves controlled fluorescence emission: Coupling into nanometer-sized polymeric waveguides," Appl. Phys. Lett. **100**(6), 063305 (2012).

[44] R. Badugu, K. Nowaczyk, E. Descrovi, J. R. Lakowicz, "Radiative decay engineering 6: fluorescence on one-dimensional photonic crystals," Anal. Biochem. **442**(1), 83-96 (2013).

[45] L. Yu, E. Barakat, T. Sfez, L. Hvozdara, J. D. Francesco, H. P. Herzig, "Manipulating Bloch surface waves in 2D: a platform concept-based flat lens," Light Sci. Appl. **3**(1) e124 (2014).

[46] E. Descrovi, F. Giorgis., L. Dominici, F. Michelotti, "*Experimental observation of optical bandgaps for surface electromagnetic waves in a periodically corrugated one-dimensional silicon nitride photonic crystal,"* Opt Express, **33**(3), 243-246 (2008).

[47] E. Descrovi, T. Sfez, M. Quaglio, D. Brunazzo, L. Dominici, F. Michelotti, H. P. Herzig, O. J. Martin, F. Giorgis, "Guided Bloch surface waves on ultrathin polymeric ridges," Nano Lett. **10**(6),2087-2091 (2010).

[48] F. Michelotti, and E. Descrovi, "Temperature stability of Bloch surface wave biosensors," Appl. Phys. Lett. 99(23), 231107 (2011).

[49] F. Michelotti, B.S., L. Dominici, M. Quaglio, E. Descrovi, F. Giorgis, F. Geobaldo, "Fast optical vapour sensing by Bloch surface waves on porous silicon membranes," Phys Chem Chem Phys, 12(2), 502-506 (2010).

[50] G. A. Rodriguez, J. D. Lonai, R. L. Mernaugh, and S. M. Weiss, "Porous silicon Bloch surface and sub-surface wave structure for simultaneous detection of small and large molecules, " Nanoscale Res. Lett. **9**, 383 (2014).

[51] G. A. Rodriguez, J. D. Ryckman, Y. Jiao, S. M. Weiss, "A size selective porous silicon grating-coupled Bloch surface and sub-surface wave biosensor," Biosens Bioelectron **53**, 486-493 (2014).

[52] H. Qiao, A. H. Soeriyadi, B. Guan, P. J. Reece, J. J. Gooding, "The analytical performance of a porous silicon Bloch surface wave biosensors as protease biosensor," Sens. Actuators B Chem. **211**, 469-475 (2015).

[53] I. V. Soboleva, et al., “Fluorescence emission enhanced by surface electromagnetic waves on one-dimensional photonic crystals,” Appl. Phys. Lett. **94**(23), 231122 (2009).

[54] M. Ballarini, F. Frascella., N. D. Leo, S. Ricciardi, P. Rivolo, P. Mandracci, E. Enrico, F. Giorgis, F. Michelotti, E. Descrovi, “*A polymer-based functional pattern on one-dimensional photonic crystals for photon sorting of fluorescence radiation,”* Opt Express, **20**(6), 6703-6711 (2012).

[55] A. Angelini, et al., “Fluorescence diffraction assisted by Bloch surface waves on a one-dimensional photonic crystal,” New Journal of Physics **15**(7), 073002 (2013).

[56] F. Frascella, et al., “A fluorescent one-dimensional photonic crystal for label-free biosensing based on BLOCH surface waves,” Sensors (Basel) **13**(2), 2011-2022 (2013).

[57] K. Toma, et al., “Bloch surface wave-enhanced fluorescence biosensor,” Biosens Bioelectron 43, 108-114 (2013).

[58] L. Fornasari, et al., “Fluorescence excitation enhancement by Bloch surface wave in all-polymer one-dimensional photonic structure,” Appl. Phys. Lett. 105(5), 053303 (2014).

[59] A. I. Tahachou, I. V. Zozoulenko, “Waveguiding properties of surface states in photonic crystals,” J. Opt. Soc. Am. B 23(8), 1679-1683 (2006).

[60] T. Sfez, E. Descrovi, L. Yu, D. Brunazzo, M. Quaglio, L. Dominici, W. Nakagawa, F. Michelloti, F. Giorgis, O. J. F. Maertin, and H. P. Herzig, “Bloch surface waves in ultrathin waveguides: near-field investigation of mode polarization and propagation,” J. Opt. Soc. Am. B **27**(8), 1617-1625 (2010).

[61] M. Liscidini, D. Gerace, D. Sanvitto, and D. Bajoni, “Guided Bloch surface wave polaritons,” Appl. Phys. Lett. **98**, 122228 (2011).

[62] L. Yu, E. barakat, W. Nakagawa, and H. P. Herzig, “Investigation of ultra-thin waveguide arrays on a Bloch surface wave platform,” J. Opt. Soc. Am. B **31**(12), 2996-3000 (2014).

[63] A. Densmore, A. “Sensitive Label-Free Biomolecular Detection Using Thin Silicon Waveguides,” Advances in Optical Technologies 2008, 1-9 (2008).

CHAPTER 3

Waveguide Coupled BSW Resonances

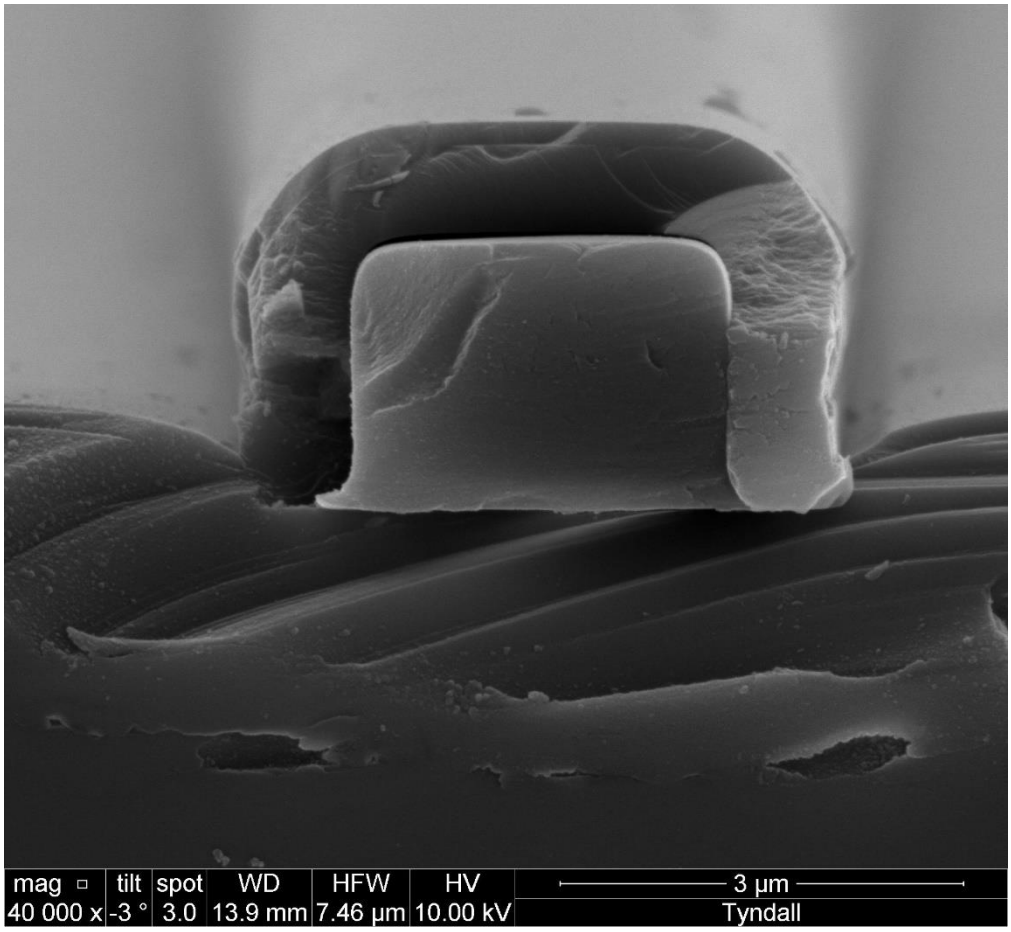

Publications from Chapter

- **Muhammad Umar Khan**, John Justice, and Brian Corbett, "Waveguide coupled Bloch surface wave resonances," Opt. Express (Submitted).
- **Muhammad Umar Khan**, John Justice, and Brian Corbett, "Resonant waveguides," Conference paper (In preparation).

My Contributions

Designed, simulated and characterised the waveguide coupling. Samples were fabricated by John Justice.

3 Waveguide coupled BSW resonances

It was proposed and demonstrated using simulations in section 2.3.4 that on-chip BSW resonances can be excited without the K-R coupling prisms if we deposit the designed thicknesses of silicon (70 nm) and silica (676 nm) on a carefully designed polymer waveguide.

Here the design, fabrication and characterization of waveguide coupled BSW sensors are explained. Two different possibilities for the dielectric layer deposition on the waveguide are proposed. The dielectric layers can either be deposited on the top surface only or on all three sides of the waveguide. Deposition on all three sides of the waveguide makes the sensor resonant for both TE and TM polarisations. The dielectric layers can also be deposited on the substrate before the fabrication of the waveguide for a reference resonance which will not shift with the analyte. The simpler of the proposed structures having dielectric layers deposited on the top surface only were fabricated in the first step to experimentally demonstrate a surface wave resonance around 800 nm wavelengths. Air and water were used to show the shift in resonance with refractive index change above the surface. The sensitivity for the waveguide coupled sensor with dielectric layers deposited on the top only was experimentally measured to be 300 nm/RIU. The sensor having dielectric layers deposited on all three sides of the waveguide was fabricated in the next step. The sensor was designed, fabricated and characterised to show resonances around 1550 nm wavelengths. It was experimentally demonstrated that the both TE and TM polarised light result in excitation of a resonance.

3.1 Design

A new approach based on a waveguide coupled BSW-like resonance is proposed here as a means to avoid the bulky prism used in the Kretschmann-Raether configuration. A dual layer Si/SiO_2 with designed thicknesses of 70 nm and 676 nm respectively are to be deposited on a deep etched waveguide which will be excited by end-fire coupling for on-chip excitation of BSW-like resonance around 820 nm wavelengths. The dielectric layers can either be deposited only on the top surface or on all 3 sides of the fabricated waveguide as shown in Figure 3-1(a, b). Si/SiO_2 layers can also be deposited on the glass substrate

before the fabrication of the waveguides to excite a control resonance at the Si and Glass-substrate interface, Figure 3-1(c, d). The orientations of the electric field (polarisation) responsible for the excitation of the surface waves are indicated. The structure presented in Chapter 2 was originally designed to sustain a resonance for light having the electric field perpendicular to the surface. So, a surface wave on the top dielectric surface can only be observed for TM polarised light as shown in Figure 3-1(a). On the other hand, both TE (electric field perpendicular to the side surfaces) and TM (electric field perpendicular to the top surface) polarised light can excite the surface waves on the structure shown in Figure 3-1(b) where the layers are deposited on the sides of the waveguide as well. The structures shown in Figure 3-1(c, d) will have an additional resonance due to the layers lying underneath the waveguides. These resonances will only be excited if the effective index of the waveguide mode matches.

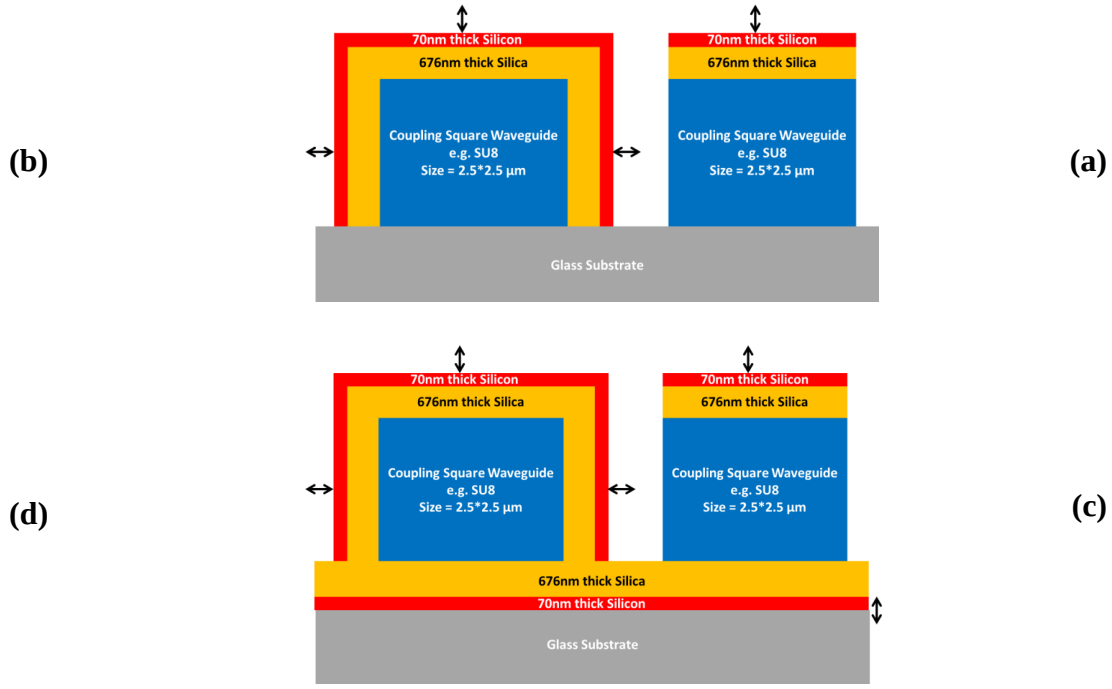

Figure 3-1: Schematic of proposed waveguide coupled structures using deposition of the resonant structure on (a) the top surface of the waveguide on glass. (b) 3 sides of the waveguide on glass. (c) the top surface of the waveguide on Si/SiO_2 underlying layers. (d) 3 sides of the waveguide on Si/SiO_2 underlying layers. The orientations of the electric field responsible for excitation of the resonance are marked.

The proposed waveguide coupled structures were modelled and simulated. SU8 polymer, being suitable for waveguiding applications, was chosen as a waveguide material on a SiO_2 (Schott AF-32) substrate. The refractive index of the polymer should be larger than SiO_2 to prevent coupling of the light to the substrate. It was found that a waveguide mode with effective index of 1.54 (i.e. to match the effective index of the BSW-like resonance) can be achieved using a 2.5 µm x 2.5 µm SU8 waveguide.

The structures were modelled and simulated for transmission responses of the structures shown in Figure 3-1. The calculated transmission responses for the structure shown in Figure 3-1(a) having Si/SiO_2 layers on top of the waveguide only are shown in Figure 3-2(a). The transmission responses were calculated for TM polarised light. Air and water were used above the surface to show the shift of the resonance with the change in refractive index above the surface. The calculated shift in resonance was almost 100 nm resulting in a sensitivity of 300 nm/RIU.

The calculated transmission responses for structure shown in Figure 3-1(c) having Si/SiO_2 layers both on top and bottom of the waveguide are shown in Figure 3-2(b). Two different resonance dips at 690 nm and 900 nm wavelengths for air above the surface can be noticed in the transmission response. The transmission response was calculated for TM polarised light. These resonance dips are due to excitation of surface waves on the top and bottom surfaces of the SU8 waveguide. As two different media, air and the glass substrate, are in contact with the silicon layers sustaining the surface waves so the resonances are at different wavelengths.

The calculated electric fields for these modes at resonance are shown in Figure 3-2(d, e). It can be noticed that the resonance at 900 nm wavelengths shown in Figure 3-2(d) is excited at the interface of silicon and glass substrate with the field penetrating into the substrate. A change in refractive index in the surroundings will not have any effect on this resonance as mode is buried inside the structure. Water was used as the surrounding medium to validate that only the resonance at 690 nm wavelengths shifted. The resonance at 900 nm was not shifted by changing the surrounding medium to water and can be used as a reference resonance to measure the shift in the surface wave resonance. The field distributions calculated for the structure having dielectric layers on all sides (Figure

3-1(d)) are shown in Figure 3-2(c-e). TE polarised light results in excitation of surface waves on both side walls, Figure 3-2(c). The surface waves on the top and bottom surfaces for TM polarised light are shown in Figure 3-2(d and e) respectively. This confirms that the structures shown in Figure 3-1(b, d) can be used to excite surface waves for both TE and TM polarised light.

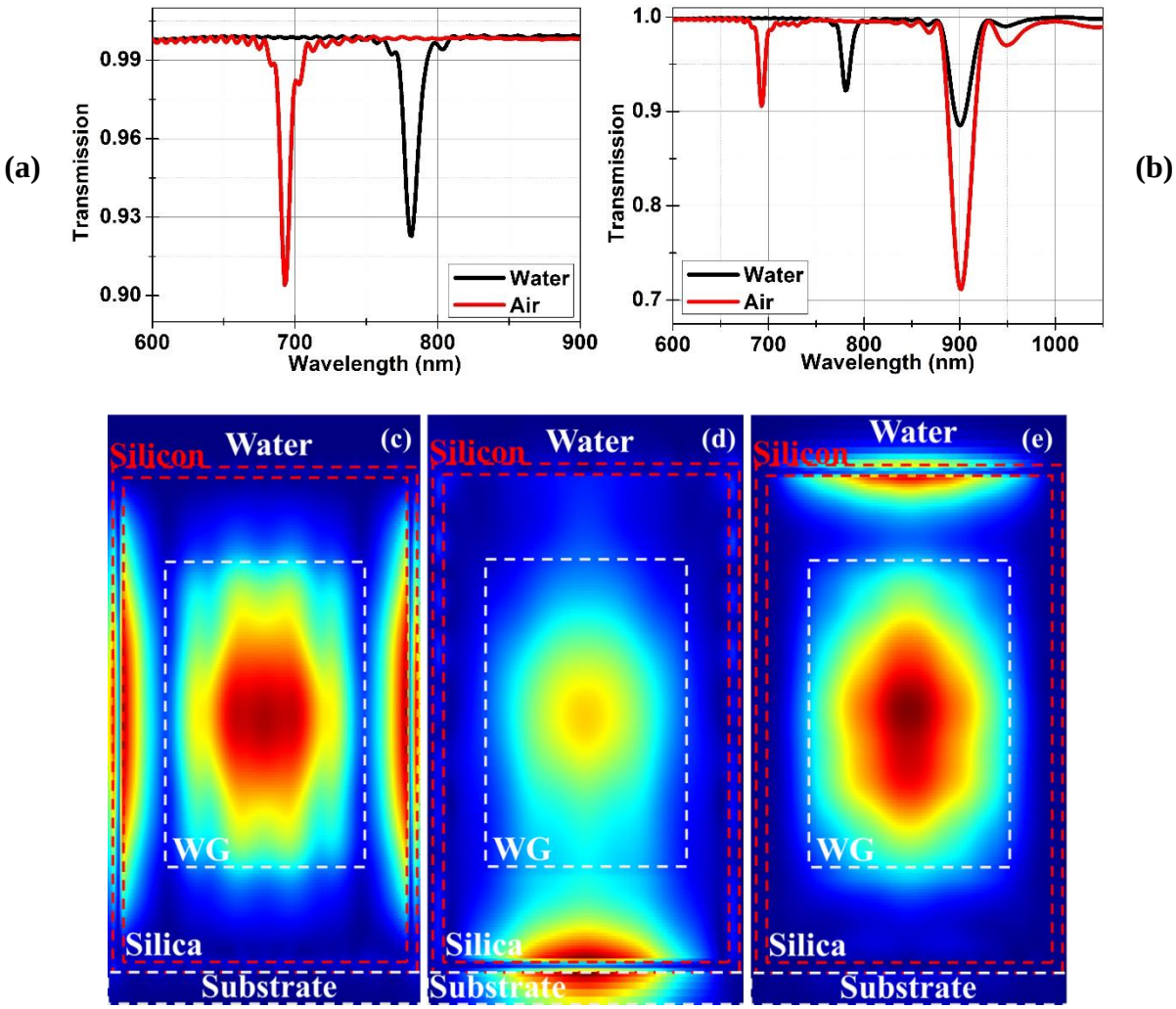

Figure 3-2: (a) Calculated transmission for TM polarised light shows a resonance at 690 nm wavelengths for air surroundings. A resonance shift of about 100 nm was observed for changing of environment from air (n=1) to water (n=1.33). These responses were calculated for a waveguide covered by sensing layers on top surface only. (b) Calculated transmission for TM polarised light showing resonances at 690 nm and 900 nm wavelengths for an air environment. Change of environment from air (n=1) to water (n=1.33) resulted in shifting of the 690 nm resonance only. These responses were calculated for a waveguide having sensing layers on both top and bottom surfaces. (c) Calculated fields for TE polarised light shows that surface wave will be excited on both side walls as

electric field is perpendicular to these walls. (d) Calculated electric field for resonance around 900 nm wavelengths for TM polarised light. The field is buried inside the glass substrate and has no interaction with the surrounding medium. (e) The calculated electric field for resonance at 690 nm wavelength for TM polarised light. The field is penetrating into the surrounding medium. These fields were calculated using the structure shown in Figure 3-1(d).

Simulations were performed to investigate the effect of small variations in refractive index of the waveguide or thickness of the silicon layers. The refractive index of the SU8 waveguide was varied from 1.535 to 1.585 to show that the resonance wavelength changes with change in refractive index due to change in effective index of the waveguide mode. The resonance depth decreases due to the mismatch between the surface mode and the effective index of the waveguide. The thickness of the silicon layer was varied from 60 nm to 80 nm to show that resonance wavelength increases with an increase in thickness of the silicon layer. The strongest resonance was observed for a thickness of 70 nm with water above the surface. This calculated thickness of 70 nm is in agreement with the silicon thickness used for sensors demonstrated in chapter 2. The simulation results for these variations are shown in the figure below.

(a)

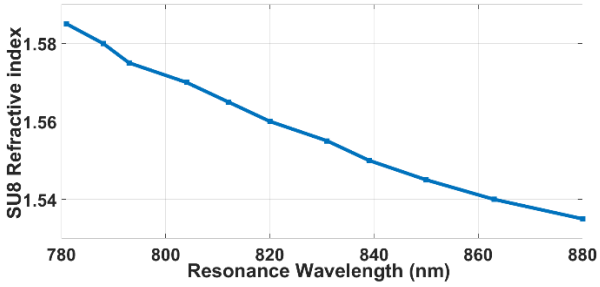

(b)

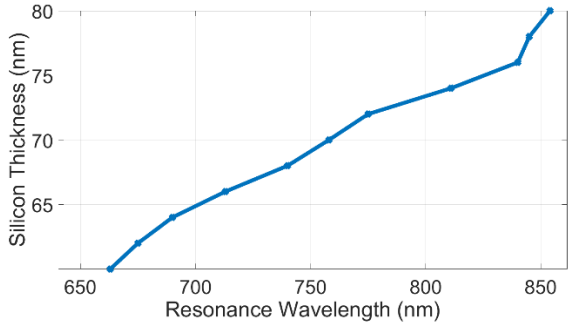

Figure 3-3: (a) Plot showing the change in resonance wavelength with change in refractive index of the SU8 waveguide. An increase in refractive index of the waveguide results in resonance at smaller wavelengths or vice-versa. (b) Plot showing an increase in resonance wavelength with increasing refractive index of the SU8 waveguide.

3.2 Fabrication and Characterization

Waveguides with sensing layers only on the top surface being the simplest among the proposed structures were fabricated in the first step to experimentally demonstrate the working of this sensing platform. Schott AF-32 wafer was pre-treated by Dehydrate bake at 200°C for 5 minutes. O_2 plasma was used for 4 minutes at 250 Watts to promote the adhesion before the spin coating. A 2500 nm thick SU8 layer was deposited on the pre-treated AF-32 wafer by spin coating. The sample was annealed at 180 °C for 5 minutes to prevent possible crinkling of SU8 during Si evaporation. The sample was allowed to cool down for 10 minutes. O_2 plasma was used for 4 minutes at 250 Watts after the annealing to promote adhesion between the polymer and the SiO_2 layer. SiO_2 was sputtered on the annealed and plasma treated SU8 using the Oxford sputterer. It took 77 minutes to sputter the oxide . The thickness of the sputtered SiO_2 was measured to be 670 nm at the edge of the wafer. Si was evaporated subsequently using the Leybold evaporator to complete the deposition process. The evaporation rate during the process was 0.2 nm/sec at a flowing current value of 267 mA. No APS or heating was used during the process and tooling was at 99.4%. The deposited thickness of Si layer was found to be around 75 nm. Dry etching process (Oxide etch) was used for etching of Si/SiO_2 layers with end point detection. The sample was etched for 4 minutes at V_{pp}=480V and LUR=5.14. BCB etch was used subsequently for etching of the SU8 using V_{pp}=350V and LUR=4.8. The sample was oil bonded to a silicon wafer for the etching process. After the etching process samples were diced into chips for the measurements. The sample was diced at the lowest possible dicing speeds to get good facets. Scanning Electron Microscope (SEM) images of the fabricated waveguide are shown in Figure 3-4 below. Both the silicon and silica layers were present on the SU8 waveguide. It should be noticed that there is no delamination between the polymer and the dielectric layers.

(a)

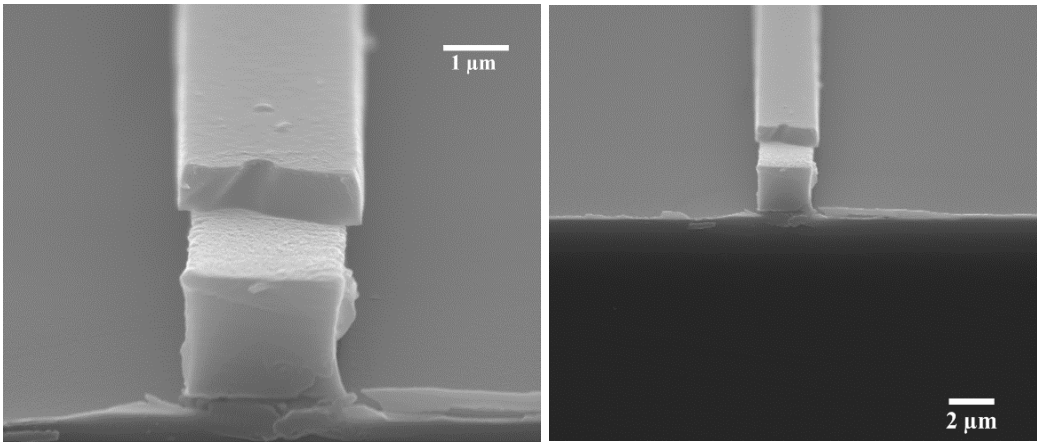

(b)

Figure 3-4: Scanning Electron Microscope (SEM) images of the Si/SiO_2 coated waveguides.

The diced waveguides were measured on a waveguide measurement system using a fibre-coupled super continuum light source from Fianium. Single mode lens ended fibres were used to couple to the input and output waveguides and the power maximised in order to measure the transmitted powers. The output fibre was coupled to an Optical Spectrum Analyser (OSA) in order to observe the spectral response of the waveguide. Transmission spectra for both TE and TM polarisations of the incident light were measured. A resonance dip was observed only for TM polarised light with air above the surface. Measured TM polarised resonance at 860 nm wavelength for air above the surface is shown in the Figure 3-5(a). Full Width Half Maximum (FWHM) of the resonance was measured to be 55 nm. The shift in resonance was investigated by putting some DI water (n=1.33) on the waveguide. A shift of almost 100 nm was observed for a refractive index change of 0.33 (i.e. 1.33(water) - 1.0(air) = 0.33) as shown in Figure 3-5(b). The bulk sensitivity was calculated to be $\frac{100}{0.33} = 303\ nm/RIU$ which was in agreement with the simulations. The resonance was measured at larger wavelength values than predicted by the simulations which can be due to a small variation in deposited silicon thickness (75 nm instead of 70 nm) or a refractive index value different than used in the simulation.

(a)

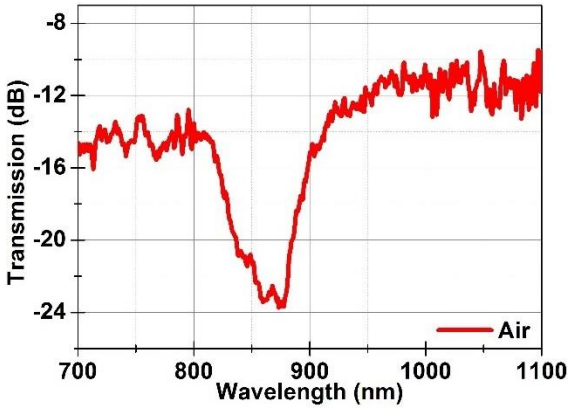

(b)

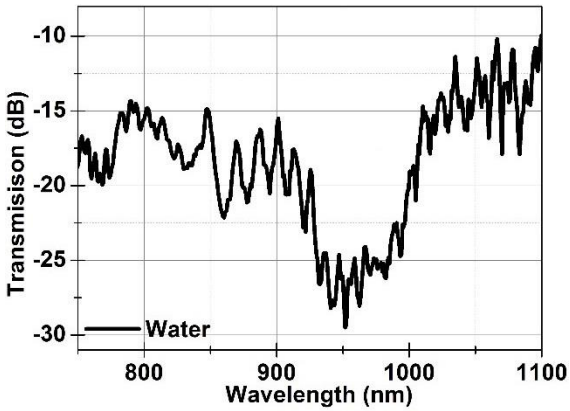

Figure 3-5: (a) Measured transmission response for air above the waveguide. A resonance can be observed for a wavelength of 865 nm. (b) Measured transmission response for water above the waveguide. A resonance can be observed for a wavelength of 963 nm.

It should be mentioned here that both resonances at 865 nm and 965 nm can be observed simultaneously if the waveguide is not completely covered with DI water. The surface wave excited at the regions having air above the surface will result in resonance around 865 nm wavelengths and surface wave excited at the region having water above the surface will result in resonance around 965 nm wavelengths. I want to comment on the observed fringe pattern that the fourier transform was calculated but no clear evidence could be concluded from these calculations. These fringes seem to appear due to the coupling lengths of a symmetric directional coupler (Taking waveguide and silicon layers as two coupling waveguides) but as the device is still under investigation so conclusions can be made after more investigations. After the experimental demonstration of waveguide coupled resonance for the waveguide with dielectric layers deposited on the top surface only, next step was to implement the structure with dielectric layers on all three sides of the waveguide for both TE and TM resonances. The sensor was designed

for resonance around telecom wavelengths due to the availability of the tuneable laser source. Use of laser will help reducing the unwanted noise in the transmission response observed for operation around 800 nm wavelengths. The design and implementation of the sensor with dielectric layers on all three sides of the waveguide for operation around telecom wavelengths is discussed in the coming section.

3.3 Operation around Telecom wavelengths

The thicknesses of the dielectric layers to be deposited on a 2.5 µm x 2.5µm SU8 waveguides for operation around telecom wavelengths were calculated. Calculations predicted that 150 nm and 1600 nm thick layers of silicon and SiO_2 respectively will result in resonance around telecom wavelengths. Simulations were performed to see the effect of variation in thicknesses of silicon and SiO_2. The calculated transmission responses for different thicknesses of silicon and silica layers are shown in Figure 3-6 below. Thickness of the silicon layer was varied from 120 nm to 200 nm keeping the SiO_2 thickness fixed at 1600 nm. It was found that the resonance moves to larger wavelength with an increase in thickness of the silicon layer. The strongest resonance was calculated for a silicon thickness of 150 nm. The thickness of the SiO_2 layer was also varied form 800 nm to 2400 nm to find that the strongest resonances can be achieved for a thickness of around 1600 nm.

(a)

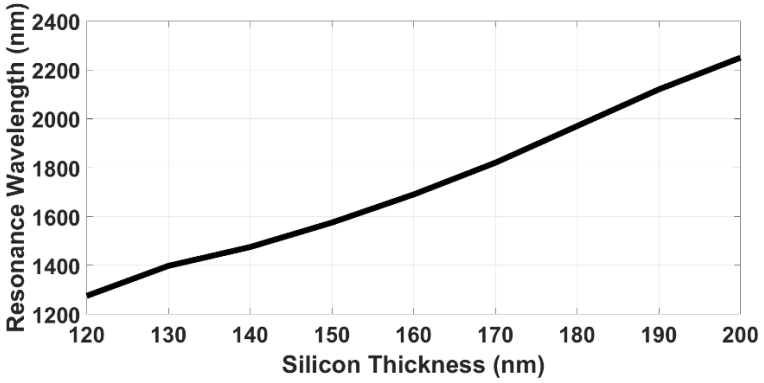

(b)

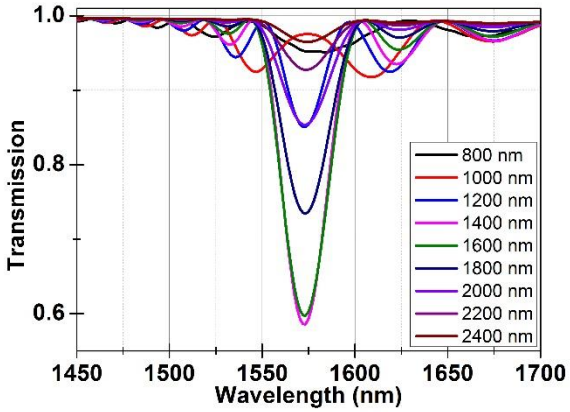

Figure 3-6: (a) Calculated transmission responses for different thicknesses of silicon layer. Thickness of the SiO_2 layer was fixed at 1600 nm for these calculations. The resonance moves to larger wavelengths with an increase in thickness of the silicon layer. (b) Calculated transmission responses for different thicknesses of the SiO_2 layer. Thickness of the silicon layer was 150 nm for these calculations.

The simulation results show that small variation in thicknesses of Si and SiO_2 will not affect the performance drastically. The designed thicknesses of 150/1600 nm for Si/SiO_2 were deposited on the SU8 waveguides. The waveguides were fabricated before the deposition of dielectric layers. A 2500 nm thick SU8 layer was deposited on a Schott AF-32 wafer by spin coating. The waveguides were made by photolithography and subsequent dry etch process. The fabricated waveguides were annealed at 180 °C for 5 minutes to prevent possible crinkling of SU8 during Si evaporation. O_2 plasma was used after the annealing to promote adhesion between the polymer and the SiO_2 layer. SiO_2 was sputtered on the annealed and plasma treated SU8. Si was evaporated subsequently to complete the deposition process. The wafer was diced into chips to optically measure the fabricated dielectric covered waveguides. Scanning Electron Microscope (SEM) image of the fabricated waveguide is shown in Figure 3-7 below. It should be noticed that there is no delamination between the polymer and the dielectric layers. There was not a big difference in thicknesses of the deposited layers on the top surface and side walls of the waveguide. This shows that the deposition of the dielectric layers on different surfaces of the waveguide was uniform and TE and TM polarised resonances should be observed for similar wavelengths of the incident light.

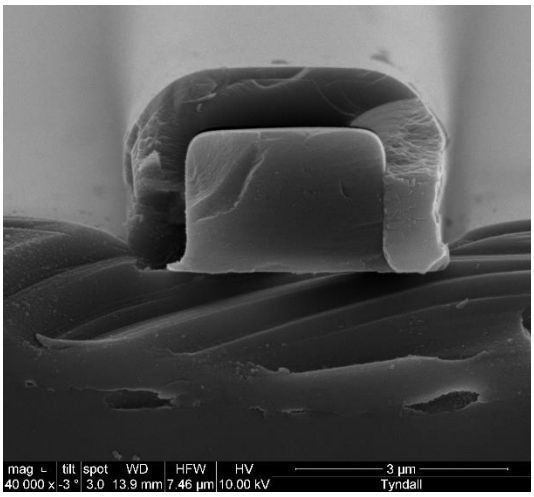

Figure 3-7: Scanning Electron Microscope (SEM) image of the SU8 waveguide with SiO_2 and Si layer deposited on all sides of the waveguide.

The diced waveguides were measured on a waveguide measurement system using a fibre-coupled tuneable laser source (TLS) which could be tuned from 1440 nm to 1640 nm wavelengths. Single mode lens ended fibres were used to couple to the input and output waveguides of the fabricated waveguides and the power maximised in order to measure the transmitted powers. The output fibre was coupled to an infrared photo-detector to measure the output optical power. Polarisation of the light from TLS was controlled to measure transmission responses for both TE and TM polarisations of the incident light. Measured transmission responses for TE and TM polarised light are shown in Figure 3-8 below. A resonance was observed at 1535 nm wavelength for both polarisations. The depth and full width half maximum (FWHM) for TE and TM polarised lights were found to be different. The resonance for TE polarised light was found to be more prominent and broad than the one for TM polarised light. The FWHM of the TM and TE polarized resonances were measured to be 13 nm and 23 nm respectively. A surface wave is excited on each side wall of the waveguide for TE polarised light as previously shown in Figure 3-2(c). Excitation of two resonance waves for TE is the reason of this deeper resonance. TM polarised resonance is shallower as a surface wave is excited on the top surface only. The loss of the dielectric layers plays an important role in determining the broadness of the resonance. TE resonance is broader as it experiences double the loss due to a couple of surface waves excited on the side walls

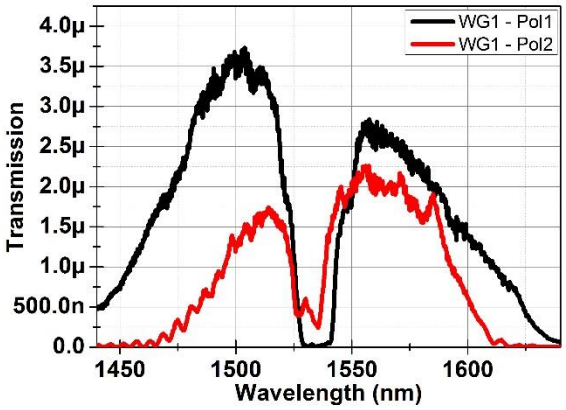

Figure 3-8: Experimentally measured transmission responses for TE and TM polarized lights.

3.4 Conclusions and discussion

To conclude, waveguide coupled BSW resonances are experimentally demonstrated by depositing dielectric layers on polymer waveguides. The dielectric layers are first deposited on the top surface to show resonances for TM polarised light only. Polarisation independent resonances (resonance for TE and TM polarised light) are demonstrated by depositing the layers on all three sides of the waveguide. A structure with dielectric layers underneath the waveguide is proposed for a reference resonance which will help determining the shift in resonance.

It seems that the silicon layer on the top surface of the waveguide is a bit thicker than the silicon layer on the side walls. This is due to the deposition in the vertical direction exposing less of the side wall area. As discussed in chapter 2, thinner silicon layer should result in resonances at smaller wavelengths. But the measurements do not show a big difference in resonance wavelengths. The difference in thicknesses of silicon layer needs investigation. The fabricated waveguides are multimode for wavelengths around 820 nm so more than one mode can couple to the surface wave. This coupling of multiple modes to the surface wave can result in a broader resonance or more than one resonances. This is the first demonstration of the waveguide coupled resonances and the details about waveguide being multimode and deposition on the substrate are still to be investigated. The initial demonstrated sensitivities are 300 nm/RIU which can be improved by carefully designing the dielectric layers and the waveguide sizes.

CHAPTER 4

Polymer Optical Interconnects

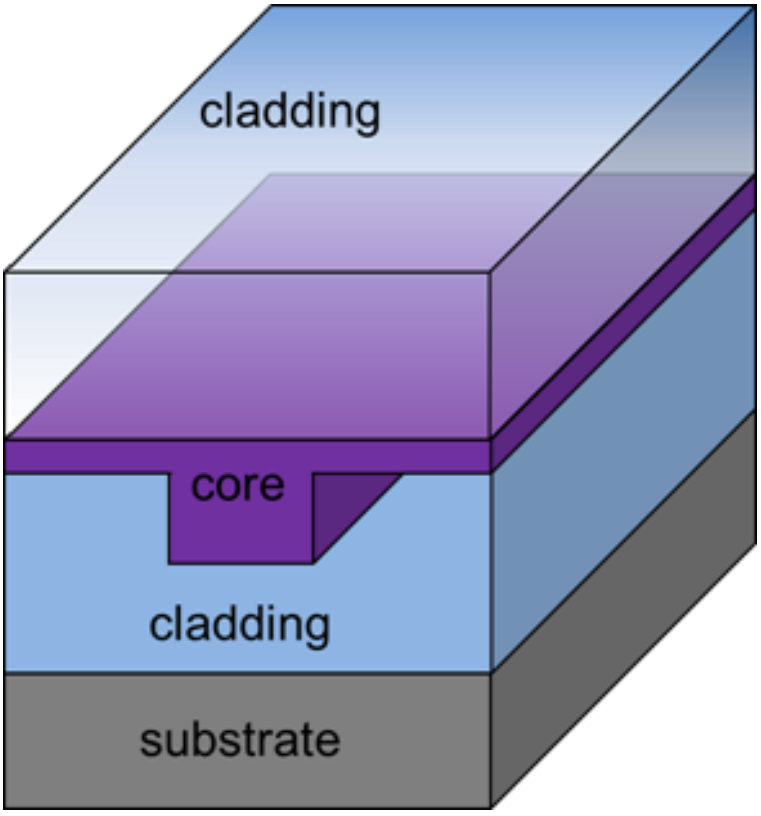

Publications from Chapter

- **Muhammad Umar Khan**, John Justice, Jarno Petäjä, Tia Korhonen, Arjen Boersma, Sjoukje Wiegersma, Mikko Karppinen, and Brian Corbett, "Multi-level single mode 2D polymer waveguide optical interconnects using nano-imprint lithography," Opt. Express 23, 14630-14639 (2015).
- John Justice, **Umar Khan**, Tia Korhonen, Arjen Boersma, Sjoukje Wiegersma, Mikko Karppinen, Brian Corbett, "Design, fabrication, and characterisation of nano-imprinted single-mode waveguide structures for intra-chip optical communications," Proc. SPIE9368, Optical Interconnects XV, 936834 (2015); doi:10.1117/12.2078974.
- Mikko Karppinen, Noora Salminen, Tia Korhonen, Teemu Alajoki, Erwin Bosman, Geert Van Steenberge, John Justice, **Umar Khan**, Brian Corbett, Arjen Boersma, "Optical coupling structure made by imprinting between single-mode polymer waveguide and embedded VCSEL," Proc. SPIE9368, Optical Interconnects XV, 936817 (2015);doi: 10.1117/12.2082935.

My Contributions

This work was part of FP7 project 'Firefly'. Characterised the fabricated waveguides and devices using waveguide measurement setup and simulated some of the devices. The samples were fabricated at VTT Finland using nano-imprint lithography (NIL).

4 Polymer Optical Interconnects

As discussed in the previous chapter, a polymer waveguide can be cladded by the designed thicknesses of SiO_2 and Si to achieve on-chip BSW resonances eliminating the bulky prisms used in the Kretschmann-Raether configuration. In this chapter, I am using the polymer waveguides for the development of an optical printed circuit board OPCB using direct Ultra Violet (UV) nano-imprint lithography (NIL). Metal based interconnects suffer from inherent disadvantages such as electromagnetic interference, power and heat dissipation issues at high operating frequencies [1, 2]. On-board polymer waveguides on the other hand are high speed interconnects that are capable of operating at rates greater than 10 Gb/s and provide a superior bandwidth × length performance in comparison to electronics [2]. Silicon photonics based interconnects are a solution for chip-level dimensions but are not realistic for board-level (1-20 cm) dimensions because of the manufacturing cost and mode size mismatch with optical fibres. So, polymer waveguides can be used as high speed and high bandwidth interconnects between racks, on backplanes, daughter cards and on the chip level [3] as shown in figure below.

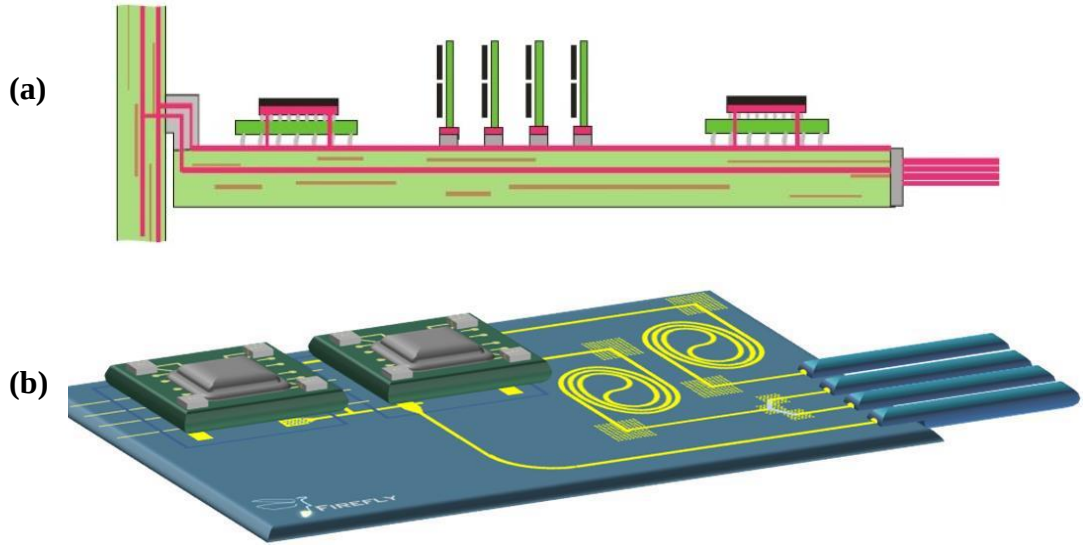

Figure 4-1: (a) Sketch showing an optical circuit board with fibre attached at the board edge. (b) Sketch showing the Firefly board as proposed in the project proposal.

A low loss and cheap polymer is desired to fabricate polymer single mode waveguides. There are a range of low loss optical polymers operating in the telecom range of 1300-1600 nm such as Poly(methyl methacrylate) (PMMA), SU8 and organic-inorganic hybrid materials [4, 5]. Particularly, Organically Modified Ceramic (ORMOCER) [6] is an excellent material for shaping optical structures via ultraviolet (UV) lithographic or stamping [7, 8] processes. Commercially available ORMOCER is used to demonstrate single-mode waveguides and passive devices for both single and multi-level centimetre sized optical boards using NIL patterning. In-plane single mode waveguides, Directional Couplers, Multi-Mode Interference (MMI) and Y-splitters are designed, fabricated and optically characterized to show the workings of the process at a single optical level. The fabrication tolerances associated with the stamping process are analysed to prove that fabrication tolerances do not affect the overall working of the devices making NIL suitable for optical interconnect applications. A method to quantify a small variation in refractive index contrast between the core and cladding of the polymer waveguides is proposed using a tuneable laser. Multilayer optical interconnects, being more challenging structures, are fabricated in the next step to demonstrate the working of an optical via and a 1x4 optical 2-D port, Figure 4-2. Coupling of light from one level to another is experimentally demonstrated similar to the working of an electrical via in copper based electrical interconnects.

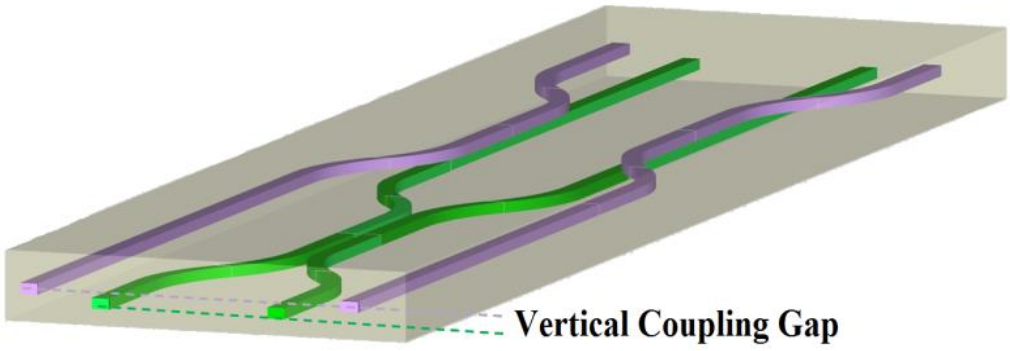

Figure 4-2: Sketch showing a schematic combination of in-plane and vertical directional couplers

4.1 Literature Review

In-plane and multi-level polymer waveguides at telecom wavelengths (1300-1600 nm) have already been reported in literature [9-16]. Previous report of polymer based 1x2 Y-branch splitters [17] shows an insertion loss (IL) of 3.8 - 4.8 dB for 12 mm long splitter. Here 2 cm long splitters show an insertion loss of 0.9 ± 0.1 dB at 1550 nm. Polymer based directional couplers have been reported with an insertion loss of 0.7 dB at 1310 nm wavelengths [18]. Here the directional couplers and MMI devices show less than 0.45 dB insertion losses at 1550 nm. Coupling of optical signal from one signal plane to another has already been reported using curved surfaces [19] or partial mirrors using sloped reflectors [20] in polymer waveguides. Single mode optical vias have recently been demonstrated in Si_3N_4 waveguides [21, 22] but this is the first time that multi-level vertical coupling of telecom wavelengths by directional couplers in polymeric waveguides using NIL is demonstrated. The use of polymers and NIL makes the fabrication process suitable for board level optical interconnects being cost effective and suitable for mass production.

4.2 Fabrication using Nano-imprint Lithography (NIL)

Single layer and multilayer single mode waveguide stacks were fabricated by full-wafer direct UV NIL of polymer materials on 100 mm diameter silicon wafers. Commercially available ORMOCER materials were used for fabrication: Ormocore with a measured refractive index, n, of 1.534 at 1550 nm and Ormoclad with a measured n = 1.519 at 1550 nm. Having less than 4 nm surface roughness [10] on NIL patterned waveguides and shrinkage of less than 5% on curing [6], ORMOCER is a very suitable polymer for waveguide applications.

The nano-imprint process broadly consists of two steps; the formation of the stamp and the nano-imprint lithography. The samples were fabricated by VTT Finland, so details of the applied fabrication processes can be found in their papers [9, 15 and 16]. Only the main process steps are overviewed and the specific parameters for the presented waveguide samples are mentioned. The stamp was formed by lithographic patterning of positive photoresist. The inverted rib process outlined in Figure 4-3(a) begins with the application of a 30 µm thick lower index cladding material, Ormoclad, by spin coating to

ensure optical isolation between the waveguide mode and the underlying substrate, Figure 4-3(a1). An imprint stamp was brought in contact with the lower cladding to form trench waveguides upon UV curing, Figure 4-3(a3). An example of a trench is shown in Figure 4-3(b). These trenches were filled by a material of a higher refractive index, namely a mixture of Ormocore and Ormoclad, which was applied via spin-coating, resulting in the formation of a slab layer of higher index material above the trench, Figure 4-3(a4). It is important that the layer is flat, filling the trench completely. The core was cured. Spin coating and curing of a lower index material, Ormoclad, on top of this slab completed the fabrication of a single level optical waveguide.

Multilayer optical interconnects were fabricated by repeating the same imprinting process for the addition of each subsequent layer. Both the lateral alignment and the vertical separation between signal planes are very important factors in the fabrication of multilayer optical interconnects. The upper layer can be laterally aligned with respect to the lower layer(s) using an optical alignment method during the imprinting with alignment patterns made on the stamp. Lateral alignment tolerances between 1 – 2 μm across a 100 mm diameter wafer were achieved, sufficient for many applications. The low refractive index cladding layer between optical planes should be flat and uniform as it defines the vertical layer-to-layer separation. The thickness variations were found to be less than ± 0.15 μm across the wafer [9]. A 30 μm thick cladding was used as the top-most cladding layer on the multilayer stack after fabricating the desired number of signal planes. In the rib waveguide process, the lower cladding was first spin coated and then the core layer was spin-coated and imprint patterned, Figure 4-3(c).

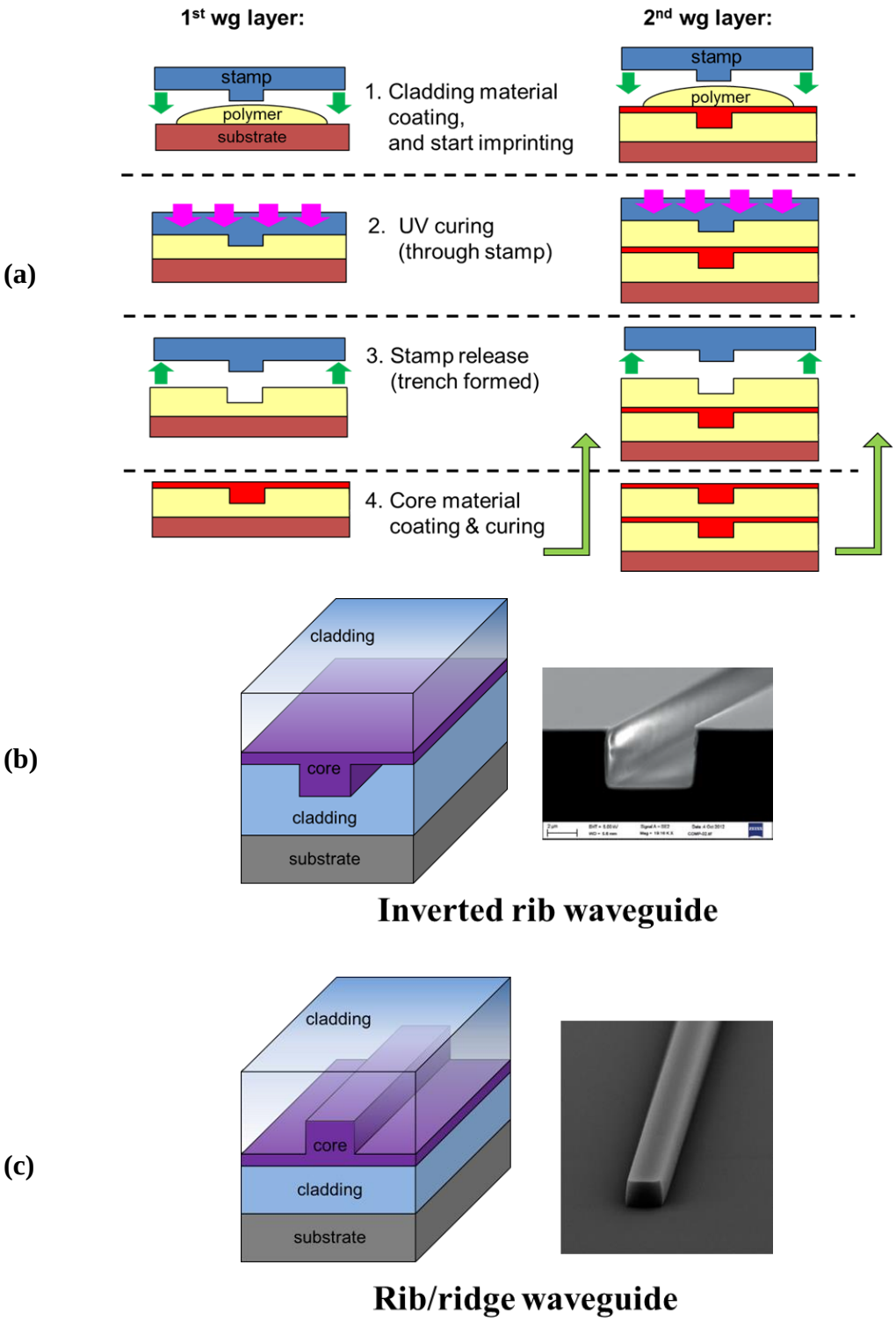

Figure 4-3: (a) Step by step fabrication process for multilayer inverted rib waveguides using UV nano-imprinting. Sketch and Scanning Electron Microscope (SEM) images of (b) inverted rib and (c) rib waveguides.

4.3 Single mode optical waveguides

Single mode optical waveguides consisting of a 5 x 5 μm core of higher index material clad by two layers of lower index material were designed with an index contrast of 0.6% between the core and the cladding polymers with n=1.528 and n=1.519 respectively. The small refractive index contrast results in low optical confinement with the mode extending into the cladding material making sidewall roughness potentially an important factor in the waveguide loss. This is not a factor here as the roughness is less than 4 nm [10] with NIL patterned ORMOCER waveguides. The majority of the waveguide loss is associated with material loss. The loss of the waveguide cladding material Ormoclad is slightly smaller (<0.1 dB/cm difference) than the loss of core material, i.e. the mixture of the Ormocore and Ormoclad. The choice of this low index contrast means that waveguide supports only the fundamental waveguide mode at 1550 nm with a Mode Field Diameter (MFD) of approximately 7 μm where the MFD is defined at $1/e^2$ of the electric field. This MFD is chosen to be intermediate between the 4-5 μm MFD of the VCSEL sources used and standard single mode fibres which have MFD of approximately 10 μm and thus maximises their coupling.

The routing of signals requires in-plane bending of the waveguides. The low contrast in refractive indices between the core and cladding of 0.6% and the resultant low optical confinement places a lower limit on the bend radius. If the bend radius is too small the light escapes the waveguide core and radiates out into the cladding causing high optical losses. Bends of large radii have two disadvantages; firstly the loss due to the length of the waveguide will be higher, and secondly, will require a large footprint on the substrate. The loss of the waveguides was measured from the attenuation of the optical signal in a long spiral of length 27 cm. The overall loss was measured as 0.84 - 0.89 dB/cm at 1530 nm and 0.75 - 0.8 dB/cm at 1550 nm, composed of material loss of about 0.7 dB/cm at 1530 nm and 0.6 dB/cm at 1550 nm (from material datasheet) and therefore an excess waveguide loss of <0.2 dB/cm in a straight waveguide. The excess loss of the waveguides at various bend radii was simulated using a commercially available 3D mode solver, FIMMWAVE from Photon design [23]. Waveguide bends of radii from 2 to 10 mm were fabricated employing these S-bends. The excess loss in the bend structures was

measured in comparison to straight control waveguides fabricated on the same chip. The waveguides were measured on a waveguide measurement system using a fibre-coupled tuneable laser source set at 1550 nm. Single mode lensed fibres were coupled to the input and output ports of the waveguides and the power maximised to measure the output powers. The measurements were repeated for three sample chips, each having the same layout. A good match between simulated and measured excess loss was observed, Figure 4-4. The measured loss increased rapidly for bend radii < 7 mm with minimal increase for bend radii greater than 8 mm. The residual layer thickness was measured via microscope imaging to be approximately 0.5 μm.

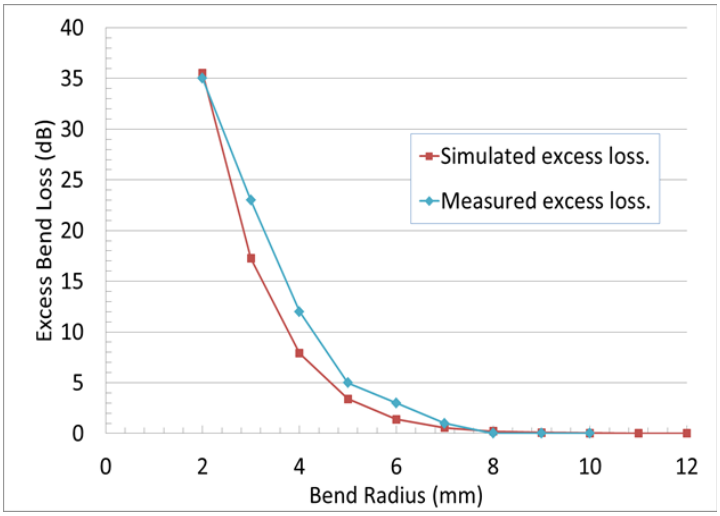

Figure 4-4: Comparison between the calculated and experimentally measurement excess bend loss values in an S-bend (2x 60° arcs) when compared to straight control waveguide. This comparison was made for a residual layer thickness of 5 μm. Lines are shown as guide to eye.

4.4 In-plane passive optical interconnects

On-board optical interconnect should include optical components capable of functions beyond the simple routing of signals. Manipulation of optical signals, such as splitting of light, wavelength multiplexing and other functions may be implemented by the inclusion of passive optical components such as multi-mode interference (MMI) devices, directional couplers and Y-branch power splitters. These devices were fabricated and the characteristics measured and compared with simulations.

4.4.1 Directional couplers (DC)

Directional couplers operate on the principle of resonant power transfer between two adjacent waveguides whose modes overlap. The amount of light transfer between waveguides can be controlled by varying the length and spacing of the waveguides in the interacting region. The gap between waveguides was chosen to be 5 µm as gaps less than 2 µm are difficult to fabricate given the waveguide feature size of 5 µm. Directional couplers were fabricated with interaction lengths varying from 500 µm to 5000 µm in 500 µm steps. Simulations predicted that the coupling length, where all the light input from one waveguide is coupled to the adjacent waveguide, was 2000 µm. The power from the 'through' and 'coupled' output ports of the directional coupler were measured, Figure 4-5(a). The total output was normalized to the input power for directional couplers of different lengths. The fabricated directional couplers displayed a coupling length of slightly less than 2000 µm with less than 0.45 dB insertion loss and 0.02 ± 0.01 dB power imbalance between outputs.

(a)

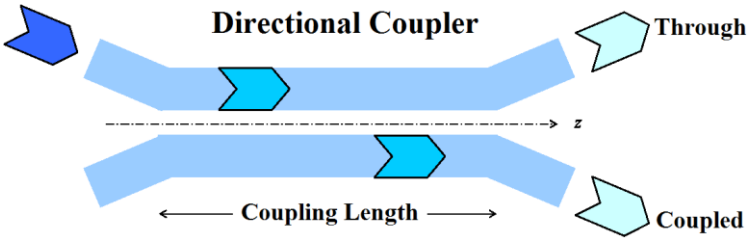

(b)

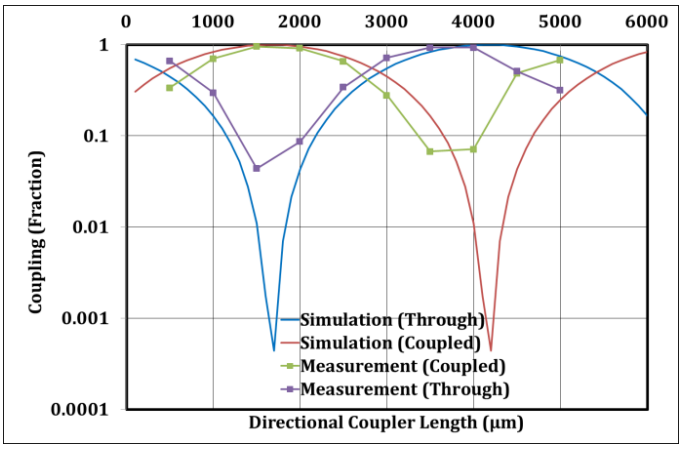

Figure 4-5: (a) Sketch showing the definition of the through and coupled ports of a directional coupler. (b) Comparison of the splitting of light in the 'coupled' and 'through' ports of polymeric directional couplers with different coupling lengths at 1550 nm.

4.4.2 Multi-mode interference devices (MMI)

Multi-mode interference devices employ self-imaging in a multi-mode section of the waveguide. The input field is reproduced in single or multiple images at intervals along the direction of propagation of the waveguide in the multimode region of the device. A MMI design employing single mode input and output waveguides and a multi-mode region of 40 μm width was chosen. This width keeps the length of a 1 x 2 splitter to less than 1 mm with the simulations predicting a peak efficiency of approximately 90% (IL = 0.45 dB) at a length of 970 μm. The efficiency was calculated as the sum of both outputs divided by the total output power through an adjacent straight waveguide which was used as a control. MMIs were fabricated with lengths varied from 880 μm to 980 μm in 20 μm steps. Some additional MMIs of lengths 1090 μm, 1100 μm and 1120 μm were also added to the chips to measure the variation in coupling efficiency. The measured efficiencies for MMIs of different lengths are shown in Figure 4-6(a) and agree well with the simulations, with the efficiency increasing with the length of the multimode region to a maximum at a length of approximately 970 μm. Multimode regions of the fabricated MMI devices were diced at different lengths along the direction of the propagation to observe the self-imaging of the input mode. Devices were diced at the lengths of 450 μm, 650 μm and 950 μm marked with red dotted lines in Figure 4-6(b). An infra-red camera was used to image the output intensity at these lengths. Good agreement between the simulated and measured intensity profiles at the different lengths of the MMI region is shown in Figure 4-6(b).

(a)

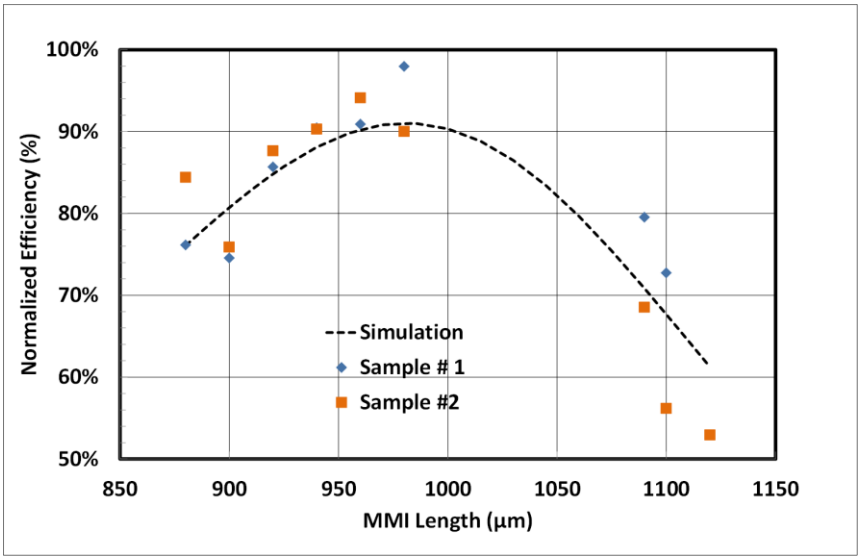

(b)

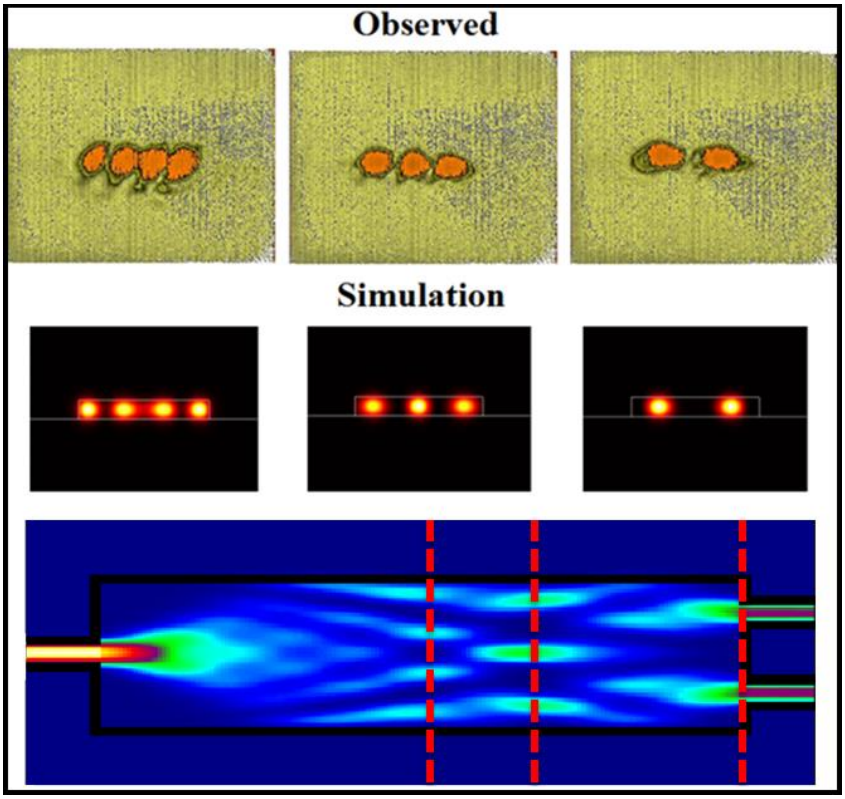

Figure 4-6: (a) Comparison of the simulated and measured efficiencies of the MMIs of different lengths measured at 1550 nm. (b) The measured and simulated modes for MMIs diced at different lengths of the multimode regions.

4.4.3 Y-Splitters

Y-branch splitters were designed and fabricated to divide the input power into half. Cascaded splitters were also designed to get different fractions of the input power shown in Figure 4-7(a). Correct splitting ratios were achieved for different devices with 0.9 ± 0.1 dB insertion loss and 0.02 ± 0.01 dB power imbalance between the outputs. Insertion loss can be improved by further optimizing the design and fabrication process.

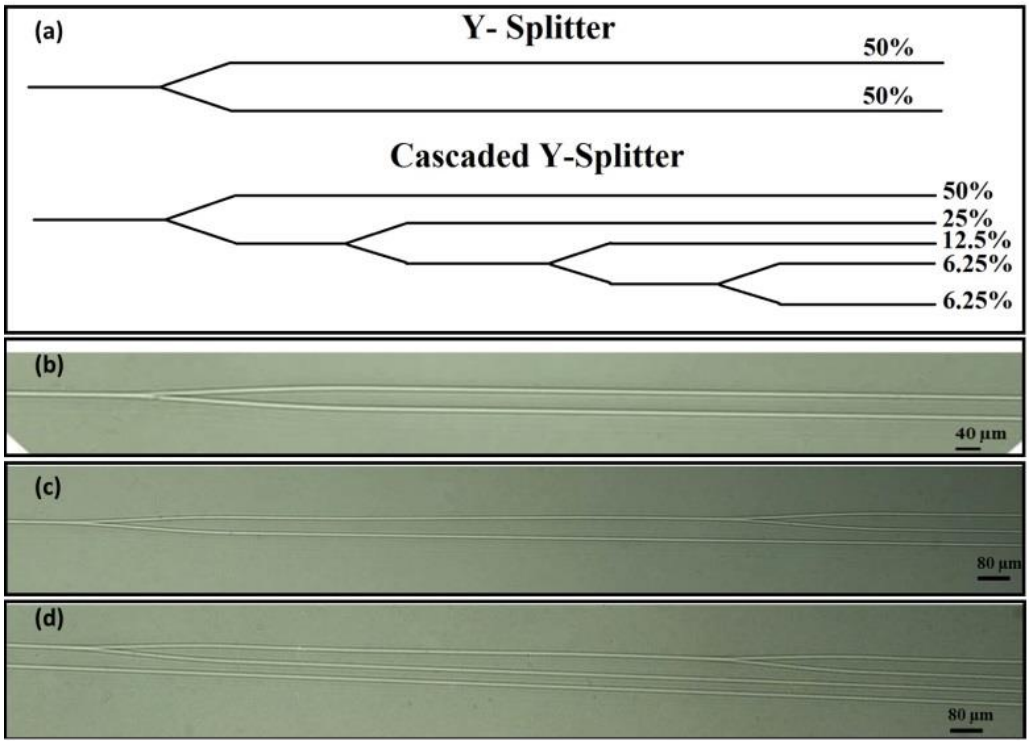

Figure 4-7:(a) Sketches of Y-splitters designed for 50-50% and 50%, 25%, 12.5%, 6.25% and 6.25% splitting. Microscope images of (b) the fabricated 50-50% Y-splitter, (c) the start of the cascaded Y-splitter and (d) the continuation of the cascaded Y-splitter.

4.4.4 Fabrication Tolerances

The use of NIL results in two parasitic effects: the presence of a residual layer (or slab) of core material and sloped side walls of the waveguides, Figure 4-8(a). The residual layer is inherent in the NIL process, whereas the sloped waveguide side walls originate from the stamp fabrication process. At least a small tilt of the side walls is also preferred in the imprinting, because it eases the stamp release (compared to vertical walls), thus improving the fabrication yield. Processing of polymers may also result in a variation in

the actual refractive index contrast between the core and cladding materials if the mixing ratio of the two polymers used in "tuning" the core index is not controlled precisely. Simulations to investigate the effect of these variations show that directional couplers are much more sensitive as compared to MMI devices. The sloped sidewalls reduce the effective gap between the waveguides of the directional coupler in the coupling region, thus reducing the coupling length, Figure 4-8(e). The side wall angles were consistently measured to be less than 20° in the fabricated samples. A thinner residual layer increases the coupling length of the directional coupler by increasing the effective index contrast between adjacent waveguides and thereby increasing the modal confinement and reducing the evanescent field overlapping the adjacent waveguide in the coupling region, Figure 4-8(g). Note that the residual layer thickness in the fabricated structures was consistently measured to be less than 0.5 µm. Geometry-related variations in device performance were well controlled. Tight control of the polymer mixing ratio is essential for control of the index contrast. A larger index contrast increases the coupling length due to increased modal confinement inside the core, Figure 4-8(f). Good control of polymer mixing ratio is evident as coupling lengths of the fabricated directional couplers were consistently measured to be 1900 ± 100 µm in line with the simulations. MMI devices, whose modal expansion occurs in the core material, do not depend on the overlap of the evanescent tail of the mode into an adjacent waveguide and therefore are less affected by the changes in refractive index contrast compared to directional couplers, Figure 4-8(c). The increase in effective width due to sloped sidewalls is small and leads to a small increase in efficiency, Figure 4-8(b). The MMIs are therefore more tolerant to all these process related effects.

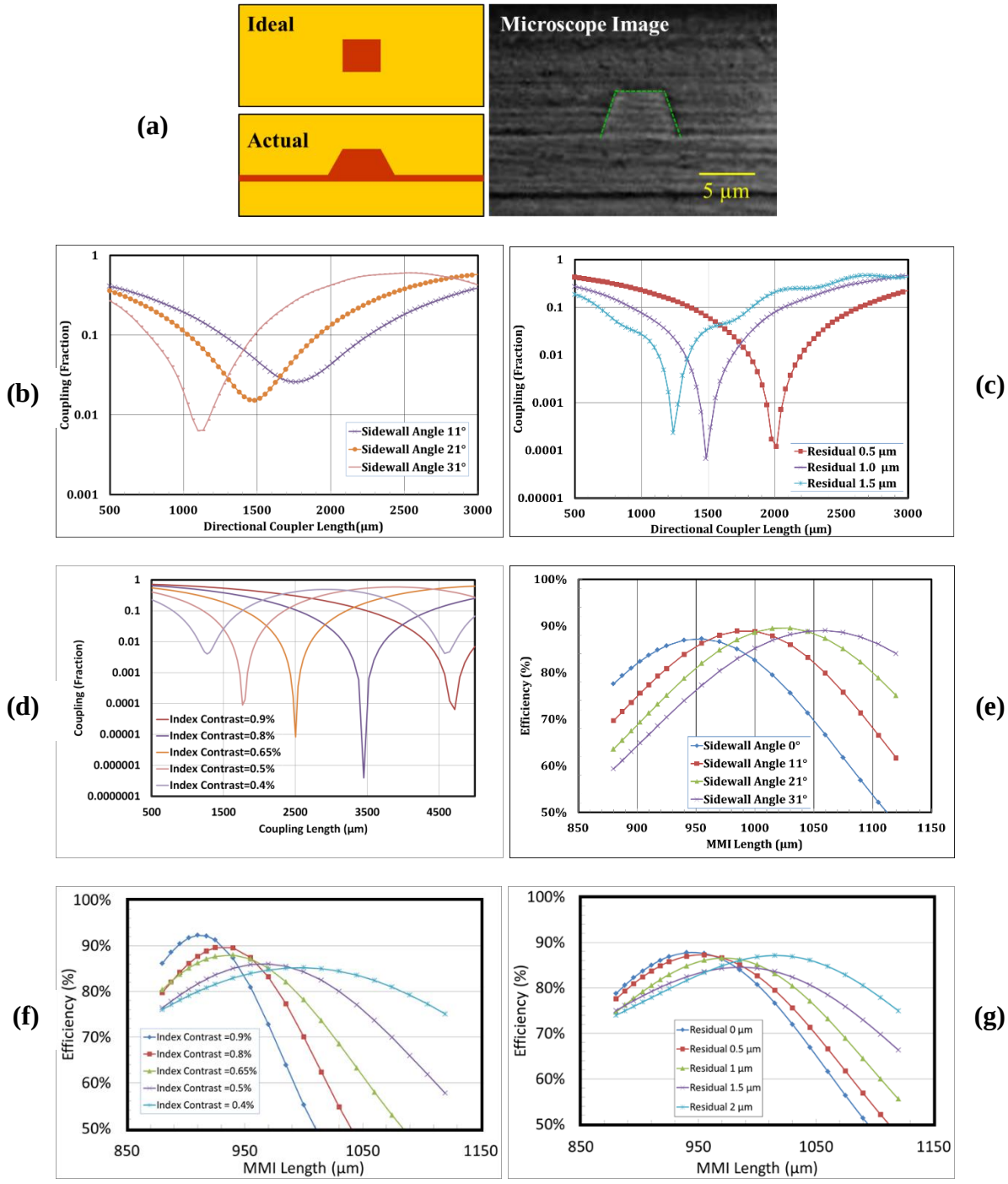

Figure 4-8: (a) A comparison between the ideal and actual fabricated waveguides. Simulations of the maximum efficiency as a function of MMI length for: (b) an increase in the side wall angle, (c) a change in refractive index contrast, (d) a change in residual layer thickness. Simulations of the maximum efficiency as a function of directional coupler length for: (e) wall angle (f) a change in refractive index contrast. (g) a change in residual layer thickness.

Simulations show that a small change in refractive index contrast, Δn, between the core and cladding results in a significant change in coupling length of the directional coupler. Thus a method to experimentally quantify a small variation in Δn of a fabricated device was investigated. This method can be used for small (5 μm) waveguides in comparison with, for example, ellipsometry which has difficulty in distinguishing small index changes in multilayer structures with small feature sizes. Waveguides of fixed dimension but with different Δn were simulated to calculate the output mode for both centre and off-centre excitations of the waveguides. Simulations show that the waveguides with Δn = 0.6% will remain single mode irrespective of the position of input excitation for all wavelengths across our measurement spectral range as represented by three wavelengths i.e. 1440 nm, 1550 nm and 1640 nm. The waveguides will become multimode for the shorter wavelengths i.e. 1440 nm and 1550 nm for off-centre excitation if the index contrast is increased to Δn = 0.7%. A further increase in the index contrast will excite multiple modes in the waveguides for all three wavelengths with off-centre excitation. The mixing ratio of the polymers was changed to get an index contrast of 0.8%, which is higher than the single mode value of 0.6%. Devices with the different index contrasts were measured using the waveguide measurement system using a fibre-coupled tuneable laser source for all three wavelengths. The output waveguide was scanned in horizontal and vertical directions to measure the output mode shape. It was experimentally observed that a waveguide having a higher index contrast was multimode for all three wavelengths and we measured a coupling length of 4000 μm for directional couplers on that chip which is consistent with the 0.8% index contrast, Figure 4-9. Note that variations in sidewall angle and residual layer thickness were measured with a microscope and would not account for the observed difference. Matching these results with simulation results confirmed that the refractive index contrast of the tested sample was 0.8% as calculated form the applied 80% - 20% mixing ratio of Ormocore and Ormoclad for the sample.

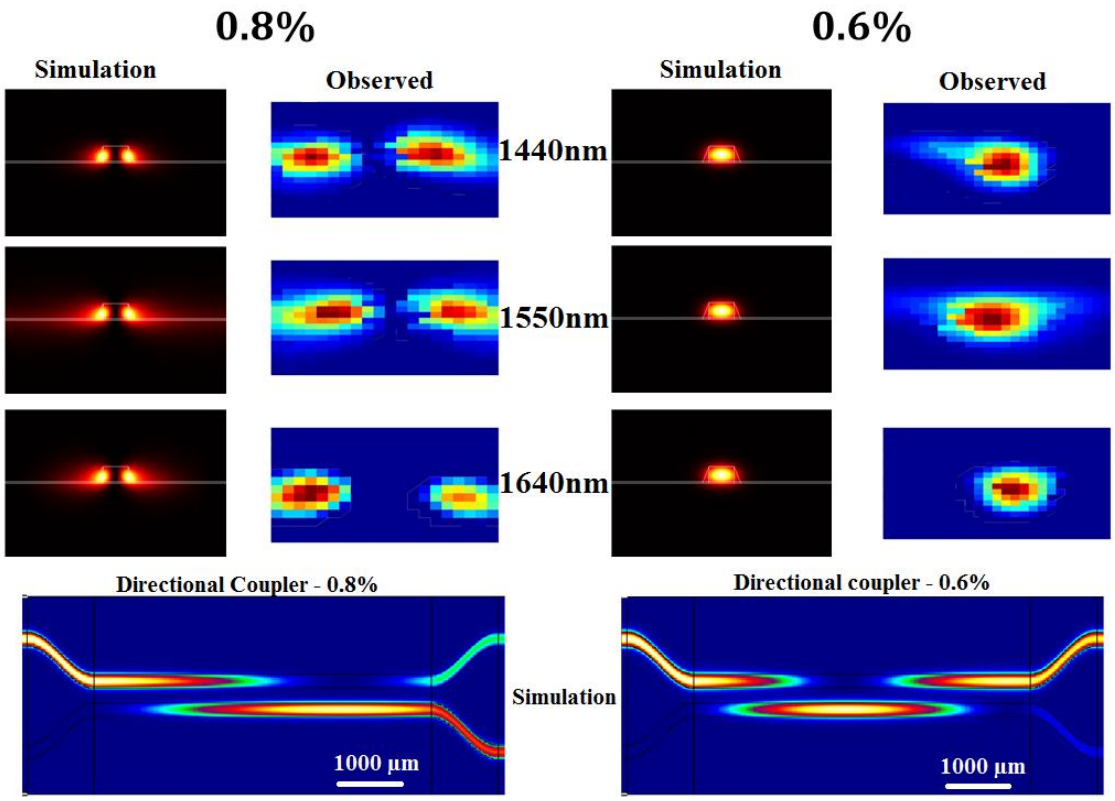

Figure 4-9: Comparison of the measured modes in a directional coupler at different wavelengths with the simulations confirms that refractive index contrast of the sample is 0.8%. The measured coupling lengths are also in agreement with the simulations.

4.5 Multilevel Optical Interconnects

Multilevel optical structures were designed to achieve coupling from one signal plane to another analogous to electrical interconnections. The vertical coupler works on the same principle as the in-plane coupler but light resonantly transfers between the waveguides closely stacked in the vertical direction. The vertical coupler thus can act as an 'optical via' to transfer light from one signal plane to another if designed to fully (100%) transfer the power. The spacing between the waveguides (top of lower waveguide to bottom of upper waveguide) in the vertical coupling region was 5 µm as for the in-plane couplers so as to obtain similar coupling lengths. Vertical directional couplers were fabricated on 100 mm diameter silicon wafers using multiple NIL stages as indicated in Figure 4-10(a). Vertical couplers with coupling lengths varying from 500 µm to 1250 µm in 250 µm steps were fabricated. The insertion loss of the fabricated devices was measured to be less than 0.45 dB. The normalized powers from the 'through' and 'coupled' outputs

of the vertical directional coupler are plotted in Figure 4-10(a). It can be seen that almost 50% of the input power was up-coupled for a coupling length of 900 μm. It can be inferred from the measured results that complete transfer of power will take place at a coupling length of 1800 μm which is consistent with the coupling length of in-plane couplers. So, a vertical directional coupler having a coupling length of 1800 μm can act as an 'optical via' to transfer power from one signal plane to another. Note that a lateral misalignment between upper and lower signal plane(s) will increase the separation between the waveguides resulting in larger coupling lengths in vertical directional couplers.

A combination of in-plane and vertical couplers as shown in Figure 4-10(d) was designed and fabricated to realize a two dimensional 1x4 port. This 2-D port was designed to equally split the input power into four waveguides spatially placed on two vertically stacked optical planes. An in-plane Y-branch coupler was used to equally split the input light into two waveguides. Two identical vertical directional couplers of coupling length 900 μm were placed on the output waveguides of the in-plane coupler to up-couple half of the available power. The fabricated devices were characterized using the setup explained earlier to measure one output at a time. Measurement results show that incident power can be split into 4 spatially placed waveguides with an insertion loss of 1.2 dB. The imbalance between the combined power in the two ports on the top layer and the corresponding power in the bottom layer was 0.2 ± 0.02 dB. The output ports of the fabricated devices were imaged using a camera by exciting an input port. The image showing the splitting of light into the 4 ports is shown in Figure 4-10(d). As the light is from a single laser source and split into four ports so the output signals should be coherent and show interference. The resulting interference fringes are shown in Figure 4-10(d) which were obtained by defocussing the camera to allow the overlap of the light from the different ports confirming the coherence of the output light.

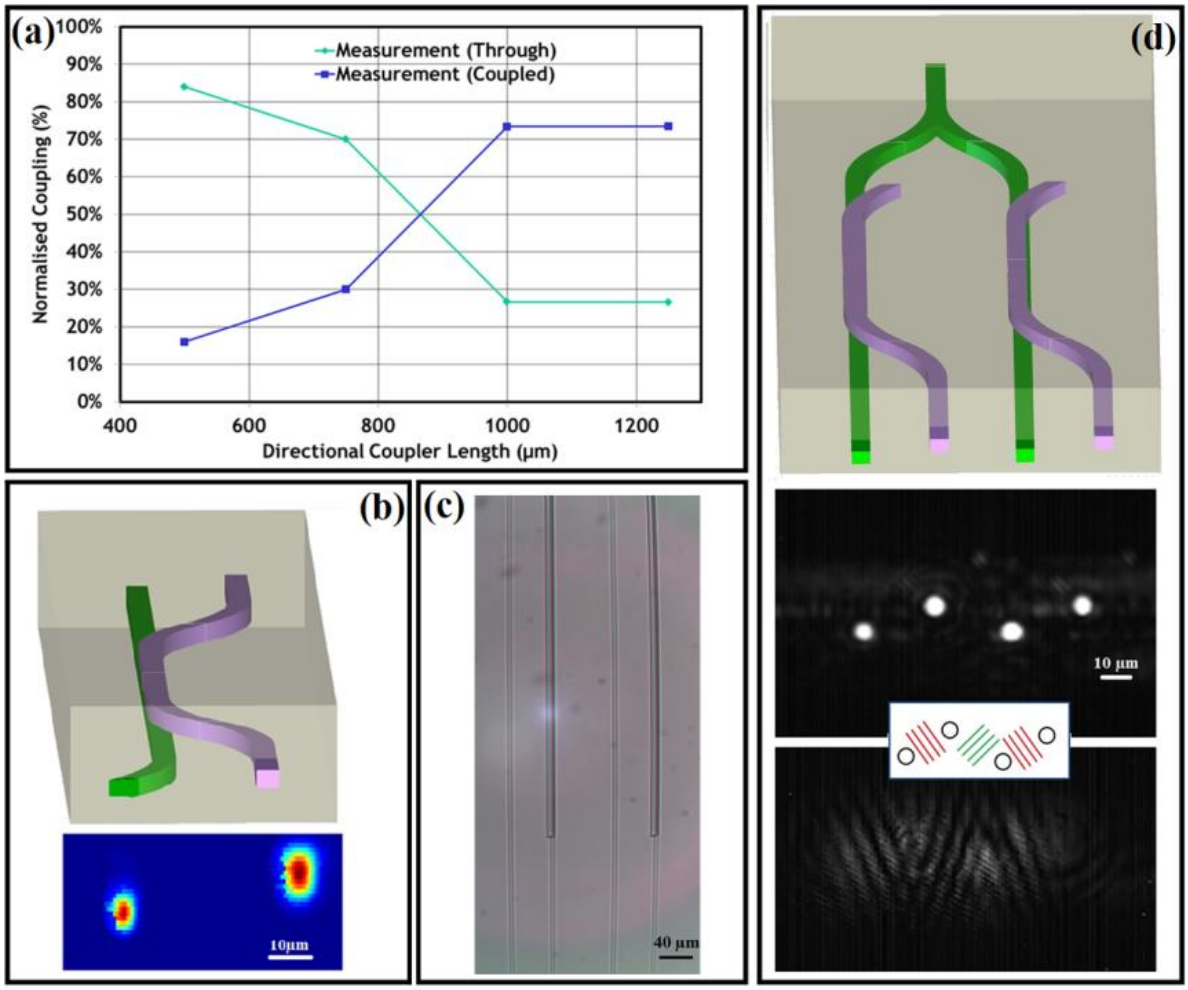

Figure 4-10: (a) Measured normalized powers from 'through' and 'coupled' ports of the vertical directional coupler. A crossing at 900 µm was also measured for in-plane directional couplers. (b) Schematic of a vertical coupler with the measured image of the light split laterally and vertically. (c) Microscope images of a multilevel device to show the alignment of the vertically connected waveguides. The top image was taken after imprinting the 2nd level waveguides and before spinning the core material. (d) Schematic of 1x4 2-D port device with camera image of light split into the 4 ports. The interference fringes were measured by defocusing the camera.

4.6 Conclusions and discussion

To conclude, single mode polymer waveguides for board-level communications are demonstrated using nano-imprint lithography (NIL). Single level and multi-level passive optical devices are demonstrated. An 'optical via' coupling light from one optical plane to another is demonstrated using a vertical directional coupler. A 1 x 4 2D optical port is demonstrated using a power splitter and vertical directional couplers. It is found that

directional couplers are more sensitive to changes in parameters (refractive index, side wall slope etc.) than MMI devices. The multilevel devices are really sensitive to the vertical alignment of the waveguides and the thickness of the cladding layer between the vertically placed waveguides. A variation in thickness of the separating cladding changes the coupling gap between the waveguides resulting in a different coupling length. In the same way, a misalignment between the vertically placed waveguides results in an increase in the coupling gap. The 1 x 4 2D optical port is even more sensitive to variation in thickness of the cladding layer between the two optical planes as a variation in thickness results in different coupling gaps for two arms of the device. This difference in coupling gaps lead to a power imbalance between the output ports. So, power imbalance between the ports can be pretty large for such devices if care is not taken while depositing the cladding layer between the two optical planes. A precisely deposited layer of uniform thickness is required for minimal power imbalance between the output ports. A vertical misalignment will affect both the arms so not a major factor in the power imbalance between the ports of the 2D port.

It is found that bending radius of the waveguide should at least be 8 mm for lossless communication. This large radius puts a restriction on the component density on a board. This large bending radius is addresses in chapter 5 using opal photonic crystals. A low index cladding was used as upper and lower claddings for these polymer waveguide cores. The cladding layer underneath the waveguide core was used to prevent coupling of light into the high index substrate. The cladding above the core was used to prevent shifting of mode into the under cladding as air above the core would have pushed the mode downwards. Air cladded waveguides are demonstrated using inveted opal crystals in chapter 5. This polymer waveguides related work helped attaining the required knowledge and the experimental experience for achieving of the waveguide coupled BSW resonances. The waveguide coupled BSW resonances are explained in the coming chapter.

4.7 References

[1] M. Horowitz, C.K.K. Yang, S. Sidiropoulos, "High-speed electrical signaling: overview and limitations," IEEE Micro. **18**, 12–24 (1998).

[2] D. A. B. Miller, "Physical reasons for optical interconnection," (Special Issue on Smart Pixels) J. Optoelectron. **11**, 155 (1997).

[3] R. Dangel, J. Hofrichter, F. Horst, D. Jubin, A. La Porta, N. Meier, I. M. Soganci, J. Weiss, B. J. Offrein, "Polymer waveguides for electro-optical integration in data centers and high-performance computers," Opt. Express **23**, 4736-4750 (2015).

[4] U. Streppel, P. Dannberg, C. Wächter, A. Bräuer, L. Fröhlich, R. Houbertz and M. Popall, "New waferscale fabrication method for stacked optical waveguide interconnects and 3D micro-optic structures using photo-responsive (inorganic-organic hybrid) polymers," Opt. Mat. **21**, 475-483 (2002).

[5] R. A. S. Ferreira, P. S. Andre, and L. D. Carlos, "Organic–inorganic hybrid materials towards passive and active architectures for the next generation of optical networks," Opt. Mat. **32**, 1397–1409 (2010).

[6] Information on Ormocer™ Materials, Ormocore™ and Ormoclad™ available at: http://microresist.de/sites/default/files/download/OrmoCore_OrmoClad_product_information.pdf

[7] W.S. Kim, J.H. Lee, S.Y. Shin, B.S. Bae, Y.C. Kim, "Fabrication of ridge waveguides by UV embossing and stamping of sol-gel hybrid materials," IEEE Photon. Technol. Lett. **16**, 1888-1890 (2004).

[8] F. Gu, H. Yu, W. Fang, L. Tong, "Nanoimprinted polymer micro nanofiber Bragg gratings for high-sensitive strain sensing." IEEE Photon. Technol. Lett. **25**, 22 (2013).

[9] T. Korhonen, N. Salminen, A. Kokkonen, N. Masuda, M. Karppinen, "Multilayer single-mode polymeric waveguides by imprint patterning for optical interconnects," Proc. SPIE **899**1, 899103 (2014).

[10] J. Hiltunen, A. Kokkonen, J. Puustinen, M. Hiltunen, J. Lappalainen, "UV-imprinted single-mode waveguides with low loss at visible wavelength," IEEE Photon. Technol. Lett. **25**, 996–998 (2013).

[11] M. Karppinen, N. Salminen, T. Korhonen, T. Alajoki, E. Bosman, G. V. Steenberge, J. Justice, U. Khan, B. Corbett and A. Boersma, "Optical coupling structure made by imprinting between single-mode polymer waveguide and embedded VCSEL," Proc. SPIE **9368**, 936817 (2015).

[12] J. Justice, U. Khan, T. Korhonen, A. Boersma, S. Wiegersma, M. Karppinen and B. Corbett, "Design, fabrication, and characterization of nano-imprinted single-mode waveguide structures for intra-chip optical communications," Proc. SPIE **9368**, 936834 (2015).

[13] A. Boersma, B. J. Offrein, J. Duis, J. Delis,M. Ortsiefer, G. V. Steenberge, M. Karpinen, A. V. Blaaderen, and B. Corbett, "Polymer-based optical interconnects using nanoimprint lithography," Proc. SPIE **8630**, 86300Y (2013).

[14] C. Gimkiewicz, H.D. Thiele, C. Zschokke, S. Mahmud-Skender, S. Westenhofer, and M.T. Gale, "Cost-effective fabrication of waveguides for PLCs by replication in UV-curable sol-gel material," Proc. SPIE **5451**, 465–474 (2004).

[15] J. Hiltunen, M. Hiltunen, J. Puustinen, J. Lappalainen, P. Karioja, "Fabrication of optical waveguides by imprinting: usage of positive tone resist as a mould for UV-curable polymer," Opt. Express **17**, 22813–22822 (2009).

[16] M. Wang, J. Hiltunen, S. Uusitalo, J. Puustinen, J. Lappalainen, P. Karioja, and R. Myllylä, "Fabrication of optical inverted-rib waveguides using UV-imprinting," Microelectron. Eng. **88**(2), 175–178 (2011).

[17] M.-C. Oh, M.-H. Lee, and H.-J. Lee, "Polymeric waveguide polarization splitter with a buried birefringent polymer," IEEE Photon. Technol. Lett. **11**(9), 1144–1146 (1999).

[18] R. Yoshimura, H. Nakagome, S. Imamura, T. Izawa, "Coupling ratio control of polymeric waveguide couplers by bending," Electron. Lett. **28**, 2135–2136 (1992).

[19] W. Ni, X. Wu, J. Wu, "Layer-to-layer optical interconnect coupling by soft-lithographic stamping," Opt. Express **17**(3), 1194-1202 (2009).

[20] C. T. Chen, P. K. Shen, T. Z. Zhu, C. C. Chang, S. S. Lin, M. Y. Zeng, C. Y. Chiu, H. L. Hsiao, H. C. Lan, Y. C. Lee, Y. S. Lin, M. L. Wu, "Chip-level 1 × 2 optical interconnects using polymer vertical splitter on silicon substrate," IEEE Photon. J. **6**(2), 7900410 (2014).

[21] D. D. John, M. J. R Heck, J. F. Bauters, R. Moreira, "Multilayer platform for ultra-low-loss waveguide applications," IEEE Photon. Technol. Lett. **24**(11), 876–878 (2012).

[22] J. Feng and R. Akimoto, "A three-dimensional silicon nitride polarizing beam splitter," IEEE Photon. Technol. Lett. **26**(7), 706–709 (2014).

[23] Fimmwave™ by Photon design [Online]. Available: http://www.photond.com/products/fimmwave.htm.

CHAPTER 5

3D Photonic Crystals for Optical Interconnects

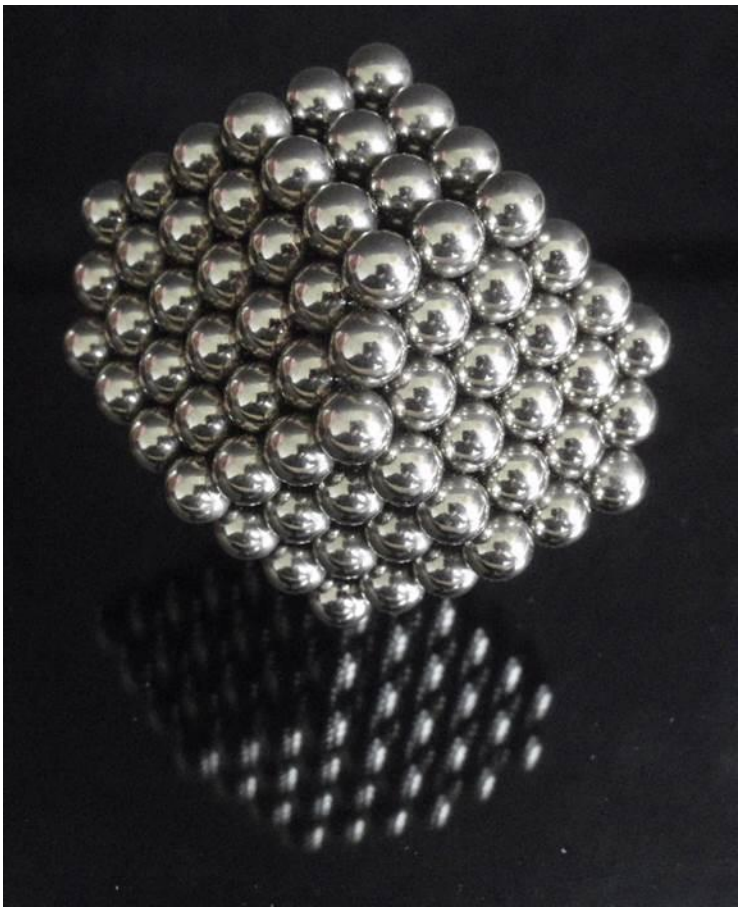

Publications from Chapter

- **Muhammad Umar Khan**, John Justice, Arjen Boersma, Maurice Mourad, Renz van Ee, Alfons van Blaaderen, Judith Wijnhoven and Brian Corbett, "Development of photonic crystal structures for on-board optical communication," Proc. SPIE 9127, Photonic Crystal Materials and Devices XI, 912705 (May 2, 2014); doi:10.1117/12.2052214.
- **Muhammad Umar Khan**, Joseph McGrath, Brian Corbett, Martyn E. Pemble, "High contrast polyimide waveguides imprinted on low refractive index inverted opal substrates by micro-molding," Advanced optical materials (submitted)

My Contributions

Sharp bends using opal photonic crystals

This work was part of the FP7 project 'Firefly'. Designed, simulated and characterised the core-shell photonic crystal structures. Silica and core-shell particles were synthesised at University of Utrecht and stacked at TNO Netherlands. The waveguides for the integrated samples were fabricated at VTT Finland.

Waveguides on inverted Opal

Simulated and characterised the waveguides. The samples were fabricated by Joe McGrath.

5 3D Photonic Crystals for Optical Interconnects

As explained in optical interconnect chapter, single mode polymer waveguides can be used to guide information-carrying light from one component to another on an optical printed circuit board (OPCB). The low cost and ease of fabrication associated with polymer waveguides make them attractive for board size applications but large bending radii (at least 8 mm) make it difficult to achieve high component density. This restriction on the bending radius is due to the small index contrast between the core and the cladding of the waveguide. Air cladded waveguides can result in higher index contrast but for that a low index substrate is required because a polymer core cannot be deposited directly on a high index substrate. Fabrication of polymer core on high index substrate will result in coupling of the light into the substrate. In chapter 4, a polymer with refractive index smaller than the core was used as under cladding between the high index silicon substrate and the waveguide core to prevent coupling of light into the substrate. An upper cladding of the same polymer as that of under cladding was deposited over the waveguide core as air above the core would result in pushing of the mode into the under cladding. An air cladded waveguide can best be achieved if the refractive index of the under cladding is close to air. As polymers with refractive index close to air are not available so cladding materials need to be used as under and upper claddings resulting in a small index contrast between the core and the cladding. Sharper bends can be achieved by either placing a reflector at 45° to the waveguide or by coming up with an under cladding having refractive index similar to air for high index contrast air cladded waveguides.

In this chapter, the use of opal photonic crystal structures for achieving sharp bends and inverted-opal as a low index substrate for polymer waveguides are discussed. In the first section, design and implementation of opal structures is presented for sharp bends in polymer waveguides. Opal based reflectors are integrated at 45° to the waveguides for in-plane bending of light at right angles. In the second section, inverted-opal structures having an effective refractive index close to air are used as under cladding for the polymer core to demonstrate effectively an air suspended polymer waveguide.

It should be mentioned here that silica and core-shell spheres were synthesised at University of Utrecht and stacked at TNO. I proposed the parameters for crystals, modelled the structures and characterised the fabricated samples. The polymer waveguides were fabricated at VTT as explained in chapter 4. The air suspended polymer waveguides discussed in the second part of the chapter were fabricated by Joe McGrath from AMSG group at Tyndall National Institute. I characterized the waveguides lying on the inverted opal crystals.

5.1 Opal Photonic crystal for in-plane bending

The design, fabrication and characterization of the opal photonic crystals are explained for achieving sharp in-plane polymer waveguide bends. Different orientations of the FCC opal crystal were explained in section 1.2.3 using the bandstructures. First of all, the design of a silica sphere based FCC (111) structure for in-plane reflections around telecom wavelengths is considered. As the waveguide is covered with a cladding polymer so this polymer can infiltrate into the colloidal crystal. This infiltration results in almost zero refractive index contrast between the spheres and the infiltrated polymer background, making it a continuous medium. So, core-shell spheres with a core of high index TiO_2 inside SiO_2 shell are proposed for larger index contrast. Calculations show that core-shell FCC (001) structures act as better reflectors than the conventional FCC (111) structures. Choosing FCC (001) also provides better control in stacking of spheres.

Silica spheres, being relatively easy to synthesise, were used to improve the stacking of FCC (001) structures using different fabrication techniques before moving on to more complex core-shell based structures. A good FCC (001) stacking was achieved on a structured substrate using a slow sedimentation technique. The fabricated silica sphere samples were analysed and optically characterized to be sure that fabricated samples had FCC (001) stacking. Core-shell samples were fabricated and integrated with polymer waveguides in the next step to experimentally demonstrate the sharp in-plane bends.

5.1.1 Modelling

A FCC structure made of 1000 nm diameter silica spheres in air background is modelled and simulated in the first step. The photonic crystal structure is 'integrated' at the end of a 5 µm x 5 µm polymer waveguide (discussed in chapter 4) with the intention to bend the light travelling inside the waveguide. The height of the crystal is equal to that of the waveguide. The FCC structure of silica spheres can act as a reflector if the index contrast (Δn) between the silica spheres (n_{silica}=1.45) and the background air (n_{air}=1.0) is sufficient to open up a band-gap in the incident direction. The photonic crystal is tilted at 45° to the incident light in order to bend the light at 90°. The reflected light is to be guided by a polymer waveguide placed at a right angle to the incident waveguide. In the simulations, air is used as the background for the stacked silica spheres. The modelled photonic crystal structure integrated with the waveguide and the calculated 90° and back reflected optical powers are shown in Figure 5-1.

(a)

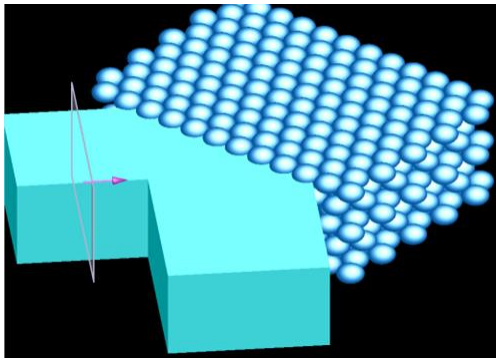

(b)

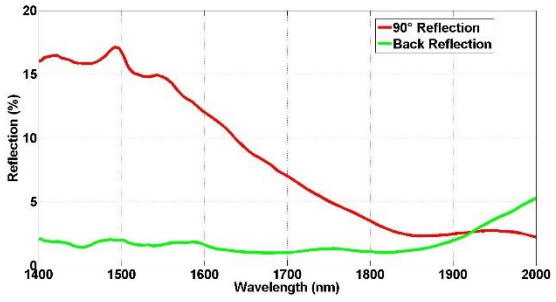

Figure 5-1: (a) Modelled FCC photonic crystal structure integrated with polymer waveguides for 90° bending of light. The photonic crystal structure is 6 sphere layers high and 10 layers deep. (b) The reflected light at 90° to the incident waveguide and in the backwards direction are plotted in red and green colours respectively.

The effective refractive index of the FCC structure is calculated to be $n_{eff} = 1.33$ using $n_{eff} = n_{silica} * 0.74 + n_{air} * 0.26$ where 0.74 is the packing factor of the silica spheres in air. The small reflection intensity at 90° to the incident light shows that the index contrast between silica and air is not sufficient to open up a wide bandgap which results in most of the light transmitting through the structure because back reflections are negligible as shown by the green plot in Figure 5-1(b).

A larger refractive index contrast is required for higher reflectivity and this can be achieved by increasing refractive index of the spheres. Core-shell spheres having core of higher refractive index material TiO_2 ($n_{titania}$ = 2.4) inside a silica (n_{silica} = 1.45) shell are considered, Figure 5-2(a). Such core-shell based structures integrated with polymer waveguides are modelled and simulated to see whether the index contrast is sufficient to be an efficient reflector at telecom wavelengths. The simulations show that a 700 nm diameter silica sphere with a 430 nm TiO_2 core can be used for reflections around 1550 nm wavelengths. The effective refractive index of the core-shell particles having $n_{core} = 2.4$ and $n_{shell} = 1.45$ is calculated to be $n_{sphere} = 1.67$ using $n_{sphere} * \frac{4}{3}\pi r_{sphere}^3 = [n_{core} * \frac{4}{3}\pi r_{core}^3] + [n_{shell} * \frac{4}{3}\pi(r_{shell}^3 - r_{core}^3)]$. The effective refractive index of core-shell FCC structure in air background is calculated to be 1.5 using $n_{eff} = 0.74 * n_{sphere} + 0.26 * n_{background} = 1.5$ where 0.74 is the sphere packing factor in FCC. The larger refractive index contrast $\Delta n = 0.67$ between the core-shell particles and the background air is very helpful for the photonic crystal to act as a reflector. The calculated reflection intensities from core-shell particles crystal are shown in Figure 5-2(b). The red plot shows that more than 50% of the incident light is reflected at 90° around telecom wavelengths. These reflections from photonic crystal reflector follow Bragg's law and move to smaller wavelengths with an increase in angle of incidence.

(a)

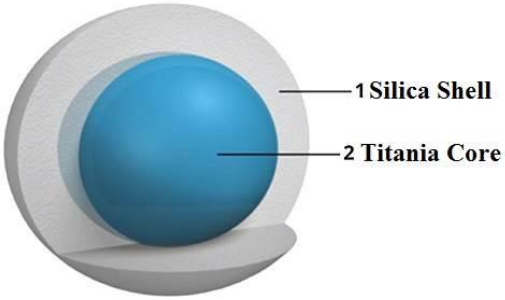

(b)

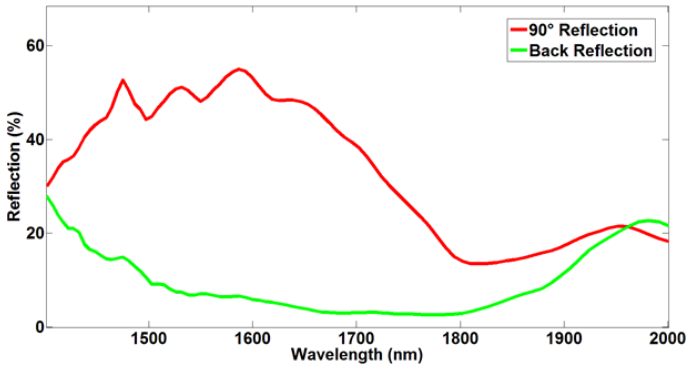

Figure 5-2:(a) Sketch of a core-shell sphere having a TiO_2 core inside SiO_2 shell. (b) Red plot shows calculated optical power in 90° waveguide. Green plot shows calculated optical power reflected backwards in the incident waveguide from TiO_2/SiO_2 core-shell photonic crystal structure.

Simulation results above show that core-shell based FCC structures with air background can be integrated with polymer optical waveguides for achieving sharp bends. The polymer waveguide core is actually not surrounded by air but by a low index polymer cladding. Deposition of the upper cladding can result in infiltration of the cladding polymer into the voids between the spheres. This infiltration may displace some of the spheres from their original position leading to the formation of random FCC structures which will ultimately degrade the performance of the reflector. This lack of control in stacking can be overcome by forcing the spheres to position themselves. A patterned substrate instead of a flat surface can be used to potentially get better control in stacking even after the infiltration of the polymer. The substrate can be patterned with small pillars or holes to achieve a rectangular grid called as the seed layer. This seed layer is intended to force the spheres to arrange themselves in a rectangular arrangement in contrast to a hexagonal arrangement without the seed layer. The subsequent layer of spheres will fit themselves in the grooves formed from first layer of spheres thus resulting in a FCC (001) stacking.

Core-shell particles structured on rectangular seed layer are modelled and simulated to show that FCC (001) structures can be used for in-plane bending of light. The FCC unit cell and the selected FCC reflecting plane are marked in black and red colours respectively in Figure 5-3(a). The model shows that FCC (001) reflecting plane is at 45° to the incident light which can only be exposed directly to the incoming light if the redundant spheres indicated by the yellow triangle are removed. These spheres in front of the selected reflecting plane decrease the reflection efficiency due to them scattering the light in different directions. Thus we truncate the photonic crystal structure at 45° to access the desired FCC plane as is shown in Figure 5-3(b). Truncated core-shell structures are simulated to calculate amount of optical power reflecting at 90° to the incident light. A cladding polymer is used as the background material instead of air for these calculations. The simulations show that a 500 nm TiO_2 core inside a 927 nm diameter silica sphere can result in 70 % reflection of incident light around 1550 nm wavelengths as shown by the plot in Figure 5-3(c). Reflection of light at right angles from the FCC (001) plane is shown in Figure 5-3(d). It should be noticed that the size of the sphere for reflections around 1550 nm has increased from 700 nm for FCC (111) to 927 nm for FCC (001) structures. This is due to the difference in distances between equivalent planes in the crystal. The size of the calculated core-shell spheres required for reflections around 1550 nm are summarised below.

Structure	**Materials**	**Core Diameter (nm)**	**Shell Diameter (nm)**	**Background**
FCC (111)	TiO_2/SiO_2	430	700	Air (n=1)
FCC (001)	TiO_2/SiO_2	500	927	Cladding polymer (n= 1.521)

Table 3: A comparison between different FCC structures.

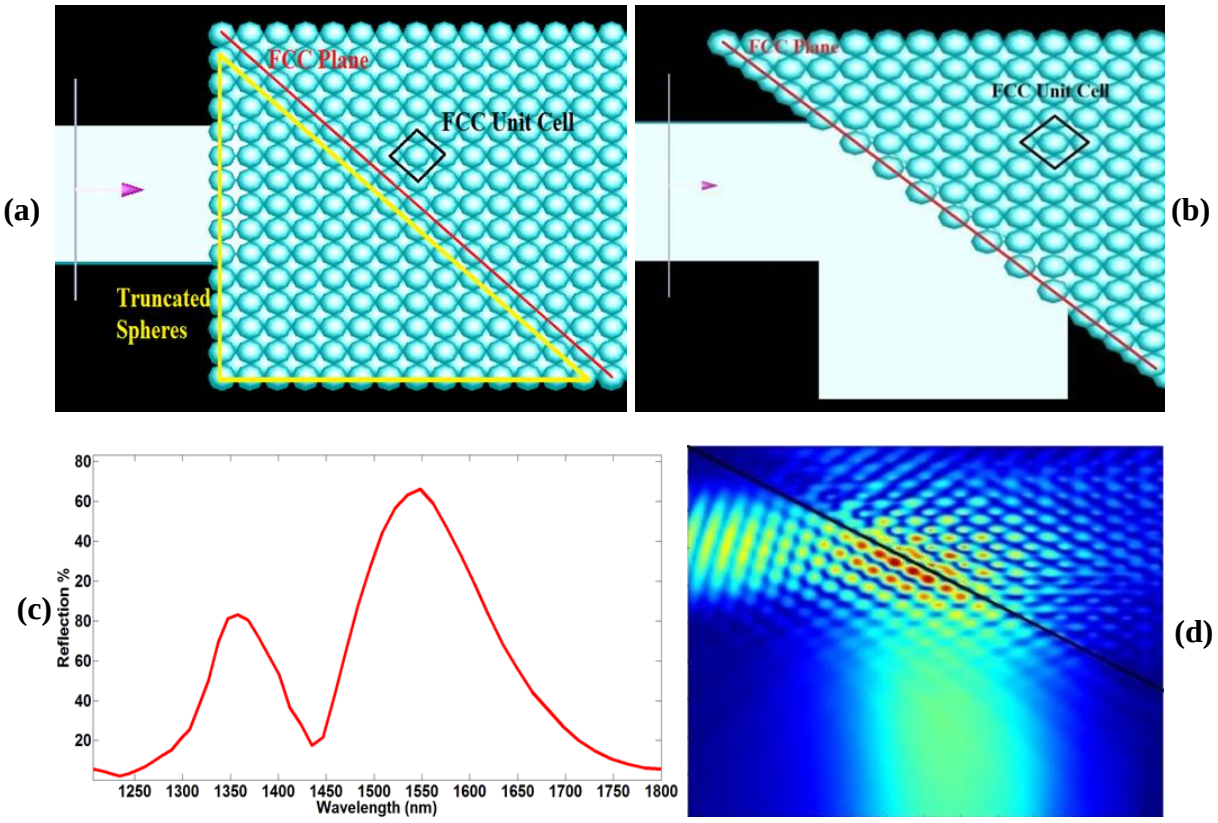

Figure 5-3: (a) Rectangular seed layer structure showing FCC unit cell (black rectangle), FCC reflecting plane (red line) and the excess spheres (yellow triangle) to be truncated. (b) Structure is truncated at 45° to expose appropriate FCC plane to the incident light. (c) Calculated reflection response from FCC (001) for right angle reflections. Red plot shows light reflecting at 90° to the incident light. (d) The image showing the bending of light at 90° to the input from the FCC (001) plane.

The relatively small peak next to the larger reflection peak in Figure 5-3(c) is due to the inter-crossing of bands. It is observed that the smaller peak just next to the initial peak gets stronger with increasing angle of incidence and depletes the initial peak.

5.1.2 Fabrication and Characterisation

Fabrication of FCC structures without any external field or force results in a hexagonal ground plane as shown in Figure 5-4(a). The presented hexagonal plane is the (111) plane of the FCC structure. The simulation results in the previous section have shown that the 45° truncated FCC (001) structures can be used as in-plane reflectors. So, a rectangular ground plane FCC (001) shown in Figure 5-4(c) is selected instead of FCC (111). The rectangular ground plane stacking FCC (001) has two major advantages over

the hexagonal ground layer FCC (111). Firstly, starting from a square ground plane, only one type of crystal is formed in the subsequent layers i.e. FCC. Secondly, all the stacked layers form reflection planes perpendicular to the substrate. It has been shown that application of external forces during spin coating or doctor blading can result in the formation of an FCC with different orientations than FCC (111) [1-3]. Unfortunately, the manufacturing of FCC (001) using only external forces is very difficult to control and crystal regions are formed in small domains only. The positioning of such crystals cannot be referenced accurately with respect to any optical features such as waveguides. In order to overcome this issue, a patterned substrate called as the 'seed layer' instead of a flat substrate was used. The seed layer had a square array of holes to force the colloid to crystallize in the (001) FCC layer [4], which should induce self-assembly of the subsequent layer into the FCC (001) crystals.

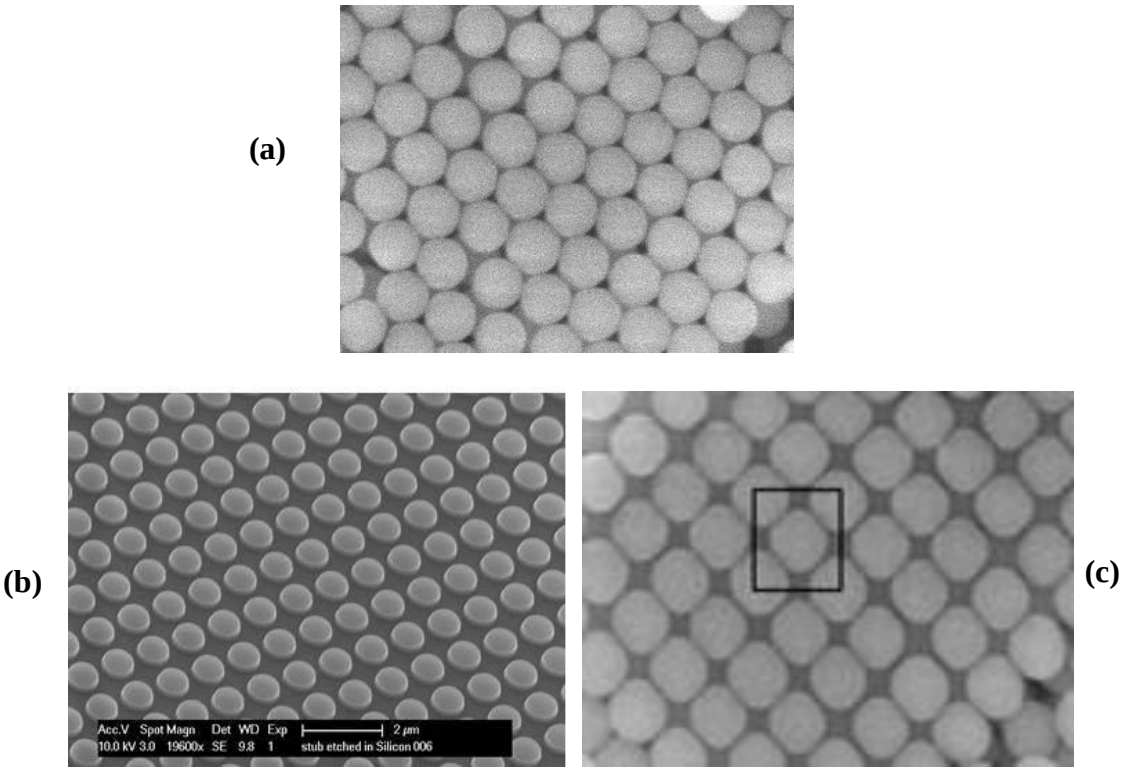

Figure 5-4: (a) SEM image of the FCC (111) plane deposited on a flat substrate. (b) SEM image of the imprinting stamp showing small pillars to fabricate a rectangular grid of holes on imprinting. (c) SEM image of the FCC (001) plane deposited on the seed layer region.

The seed layer pattern was formed by nano-imprint lithography on a flat substrate. The nano-imprint stamp had an array of rods which were marked on to a polymer substrate

to make array of holes on the substrate. During imprinting, the polymer was solidified around the rods using UV light. For these experiments, the patterns were made on an area of 1 mm^2 with holes pitch varying from 900 to 1100 nm. This variation was used in order to assess the influence of the pitch on the crystal formation. It was found that size of the particles should match the pitch size of the seed layer for a good stacking of the particles. Different pitch sizes compared with the size of the particles resulted in random stacking without any orientation.

Different methods of stacking can be used to fabricate square lattice structures over nano-imprinted seed layer regions. Different methods used for fabrication are explained below.

Sedimentation Process: Figure 5-5(a) shows the slow sedimentation process in which a diluted solution of the spheres is placed on top of the seed layer region for substantial amount of time to let the spheres sediment on the seed layer. The thickness of the sample depends on the concentration of the sample and the amount of time the spheres are allowed to sediment.

Capillary Printing: Figure 5-5(b) shows the capillary printing process in which spheres are spread over the seed layer region using a capillary containing the diluted solution.

Modified Doctor Blading: Figure 5-5(c) shows the modified doctor blading process in which spheres are spread over the seed layer region using doctor blade machine.

Spin Coating: Figure 5-5(d) shows the slow spin coating process in which a diluted solution of mono-disperse spheres is spun on the seed layer region at a desired rotation speed. The rotation speed of the spinner defines the thickness of the fabricated sample so a sample with larger number of layers can be fabricated using a lower number of rotations per minute.

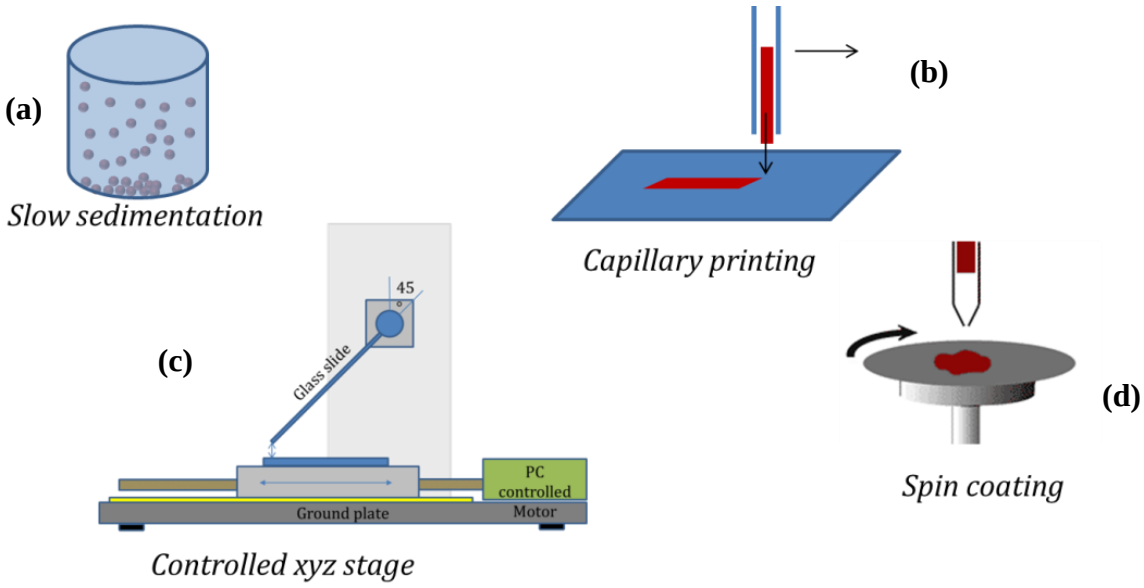

Figure 5-5: Sketches of the (a) slow sedimentation (b) capillary printing (c) modified doctor blading and (d) spin coating techniques used for the fabrication of the desired FCC (001) structures.

5.1.2.1 Silica Sphere Samples

Silica spheres, being easy to synthesise were used in the first stage to get better stacking of spheres. The spheres were stacked on a glass substrate having different pitch seed layer regions. The first multilayer (001) FCC stacking was achieved using the slow sedimentation process of 1000 nm silica spheres from a diluted (0.1 wt%) dispersion of particles in a mixture of water/ethanol (1:1). After 20 hours, a stack of approximate 7 to 8 layers was formed on the imprinted seed layers. A combination of both FCC (001) and FCC (111) orientations was observed on the top most layer. FCC (001) was observed only where seed layer was present underneath. FCC (111) was observed where seed layer was not present. It was observed that seed layers having pitch different than the diameter of the spheres had a mix of FCC (111) and FCC (001) lattice. Figure 5-6 below shows a combination of FCC (001) and FCC (111) lattice observed on such seed layer.

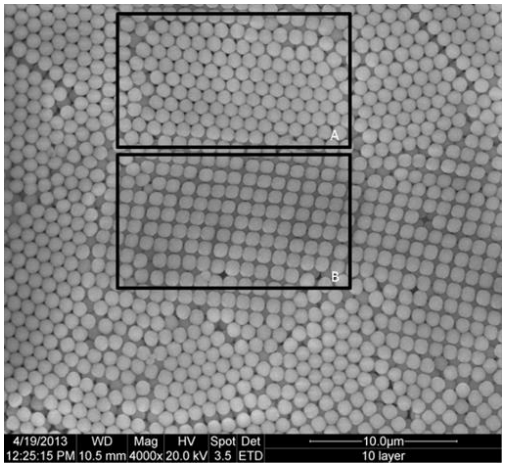

Figure 5-6: Sedimentation of 1000 nm silica spheres on square seed layer region having pitch different than the sphere diameters. The seed layer had a mix of both FCC (001) and FCC (111) lattices.

Diffraction patterns were measured for the fabricated samples to make sure that rectangular lattice FCC (001) was there throughout the deposited layers. Light was incident on the sample and the diffraction in the transmission was observed. The measurements at the regions without seed layer resulted in a hexagonal pattern on the screen as shown in Figure 5-7(a). This diffraction pattern was observed on a screen placed 10.6 cm from the sample. The pattern is defined by the horizontal planes of the spheres parallel to the substrate and the vertical thickness or the number of layers define the sharpness of the pattern. This measurement confirmed that the spheres stacked themselves in the lowest energy hexagonal FCC (111) planes on a flat surface. The diffraction pattern was marked on a paper and angles were calculated, Figure 5-7(b). A triangle can be formed by tracing the diffracted and the straight rays of the light as shown in Figure 5-7(c). The angle between the diffracted and straight rays of light was calculated to be 40°. The diameter of the sphere can be calculated using the equations below,

$$\boldsymbol{2dSin(\theta) = m\lambda} \qquad \textbf{5-1}$$

For m=1

$$\boldsymbol{2d = \frac{632\ nm}{Sin(40)} = 983\ nm} \qquad \textbf{5-2}$$

The calculated diameter was in good agreement with the measured diameters of the silica spheres. The measurements at the seed layer regions resulted in a cubical pattern with a spot at each corner of the cube, Figure 5-7(d). The measured diffraction pattern confirmed

that the spheres were stacked in the desired FCC (001) orientation. A circular pattern without any sharp spots was observed from the regions having no defined stacking e.g. on the edge of the sample where spheres were randomly stacked. So a sample without any defined orientation will result in a fused circular pattern.

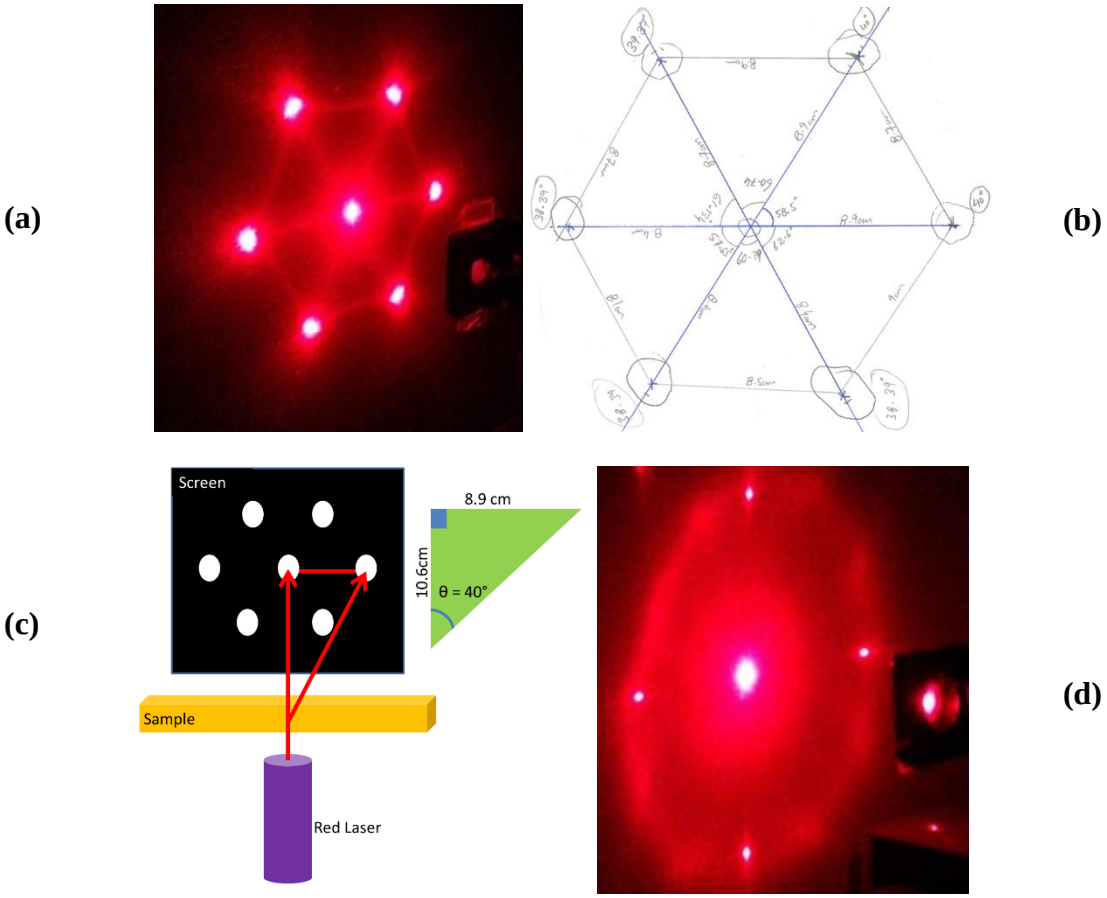

Figure 5-7: (a) The hexagonal diffraction pattern observed from the FCC (111) region deposited on the flat substrate. (b) The pattern was recorded on a paper and angles and distances calculated. (c) Sketch showing the measurement setup and the formed triangle by tracing the straight and diffracted rays from the sample. (d) A cubical diffraction pattern observed from the FCC (001) region deposited on the seed layer.

The sample with FCC (001) stacking was optically characterised to observe the back reflections. Light from a broadband white light source (Ocean Optics HL2000) was incident vertically on the sample and the back reflection measured. Light was incident using an optical circulator which coupled the back reflected light from the sample to an optical spectrometer (Ocean Optics USB 4000). The reflection from the sample was found to be position dependent. Careful investigations revealed that two different responses

were observed from the seed layer regions having FCC (001) and the flat substrate having FCC (111) as shown in Figure 5-8(b) below. The reflection with a peak around 1300 nm wavelengths was measured from the flat substrate regions (blue curve). The reflection with a peak around 1000 nm was measured from the seed layer regions (green curve). Simulations were performed to calculate the reflection response from the FCC (001) sample to be sure that this reflection peak around 1000 nm was actually from the rectangular FCC (001) region. The calculated reflection peak was found to be in agreement with the measurements (black curve). This measurement confirms that the seed layer indeed induces the formation of the FCC crystal in the desired orientation.

(a)

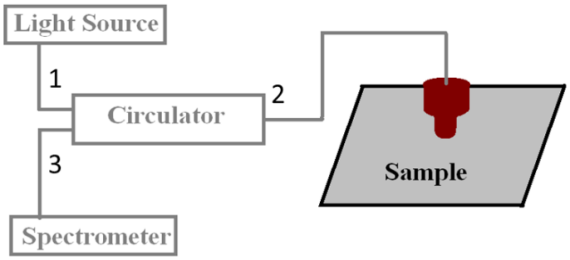

(b)

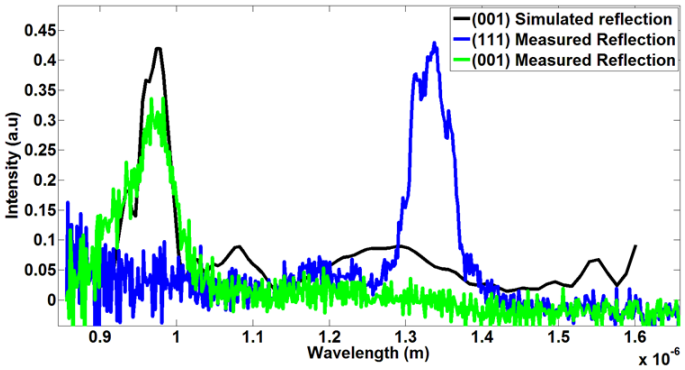

Figure 5-8: (a) Sketch of the used characterization setup. (b) Measured Reflection responses from different parts of the sedimentated sample.

Spin coating, capillary printing and modified doctor blading techniques were also used to make silica sphere samples. The fabrication techniques improved with time and the best FCC (001) stacking was obtained using the slow sedimentation process for seed layer with pitch distances equal to that of the sphere sizes. Core-shell samples were then fabricated.

5.1.2.2 Core-shell samples

The core-shell particles were synthesised using a multi-step procedure (at University of Utrecht, Netherlands). In the first step, titania (TiO_2) cores were prepared by a sol gel method. This method produced spherical particles with low (<5%) polydisperstity, density and refractive index. The spheres were heated to a temperature of 50°C to make them dense which resulted in shrinking of the diameter by 20%. At this point, the first thin silica layer was deposited on the particles. This silica layer protects the spheres from strong sintering during the crystallization phase. By heating the coated particles to 650 ˚C, the amorphous titania turned into its crystalline form called as 'anatase'. Anatase has a significantly higher refractive index (about 2.4) than amorphous titania. A second silica layer was grown on the particles. A continuous growth procedure was applied to obtain the desired particle size based on the method of Giesche et al. [5, 6]. The preparation process for core-shell particles is shown in Figure 5-9(a).

The synthesized core-shell particles were stacked on a rectangular seed layer with pitch size equal that of the sphere size (at TNO, Netherlands). Cladding polymer was infiltrated into the fabricated crystal to understand the effect of this infiltration on the stacking. The sample after the polymer infiltration was peeled off the seed layer and imaged, Figure 5-9(b). Focused Ion Beam (FIB) milling was performed on the polymer infiltrated sample to observe the stacking, Figure 5-9(c). It can be noticed that there are some dumbbell shaped spheres which are causing the stacking to move away from the desired FCC (001) at some places. So, core-shell particles of uniform size and shape are required to achieve a good multilayer FCC (001) crystal.

The reflection from the core-shell sample was measured at normal incidence using the setup shown in Figure 5-8(a). it was found to be position dependent as for the silica sphere sample. Two distinct peaks were observed for regions with FCC (001) and the region where the stacking was disturbed due to dumbbell shaped spheres resulting in FCC (111).

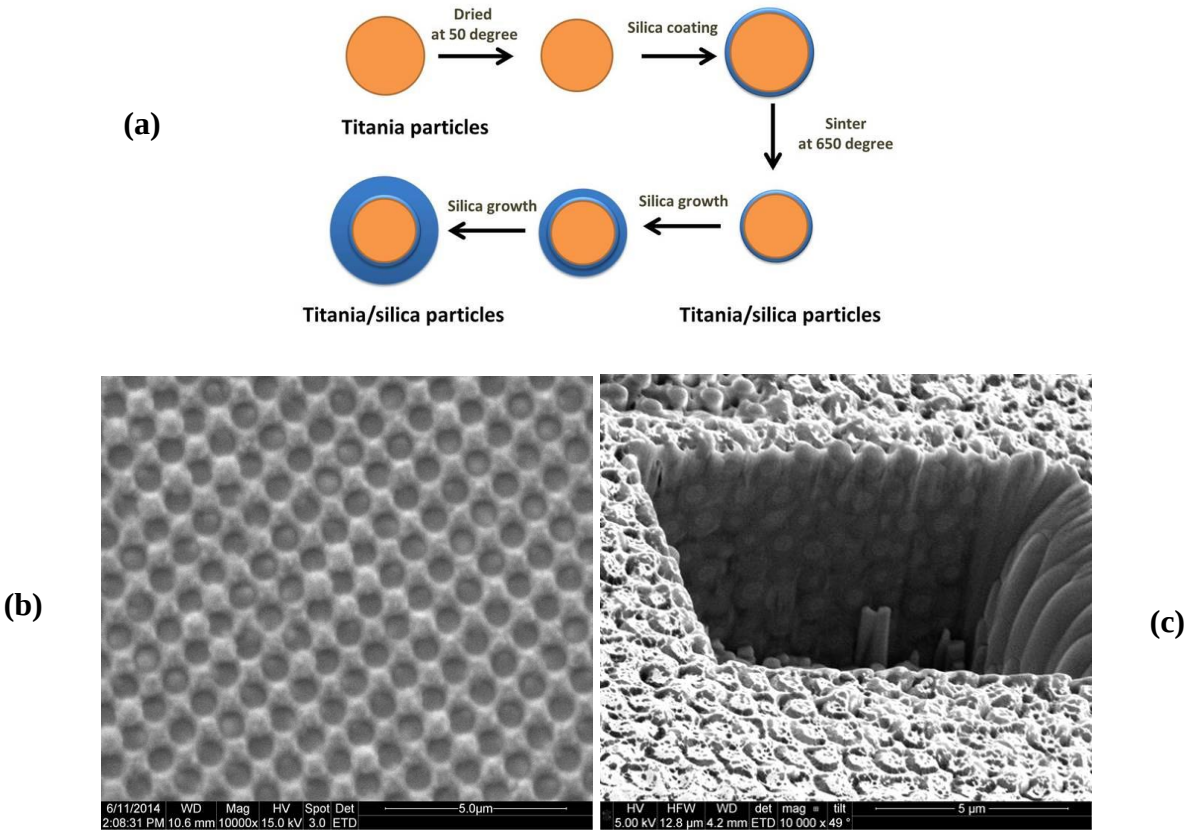

Figure 5-9: (a) Depiction of different steps for synthesis of core-shell particles. (b) SEM image of the core-shell sample after the infiltration of the cladding polymer. The sample was peeled off from the seed layer for further analysis. (c) SEM image of the FIB milled core-shell sample. Dumbbell shaped spheres cause disturbances resulting in RFCC.

This shows that good stacking can be achieved using core-shell spheres of uniform size and shape. The photonic crystal structures were integrated with the polymer waveguides in the next step.

5.1.2.3 Integrated Samples

A nano imprint lithography (NIL) mold was fabricated for the imprinting of seed layer, the flow channels and the optical waveguides, Figure 5-10. The seed layer was designed to have the FCC (001) reflecting plane at 45° to the input waveguide core. It can be noticed that the seed layer is truncated at 45° to make the light incident directly on the FCC (001) reflecting plane as explained in the design section. The flow channels were fabricated to facilitate the stacking of spheres.

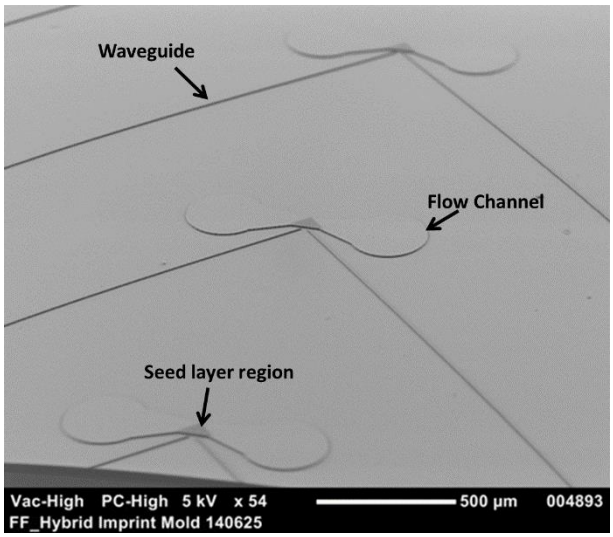

Figure 5-10: SEM image of the fabricated mold for nano-imprint lithography (NIL).

Integrated samples with colloidal crystals at 45° to the waveguides were fabricated at TNO Netherlands using these molds. Core polymer was deposited in the waveguide core regions after the imprinting. The core-shell spheres were delivered through the flow channels and were allowed to sediment in the seed layer region. The fabricated sample is shown in Figure 5-11. Polymer was infiltrated into the voids between the spheres after the stacking of the spheres. A polymer cladding was deposited to cover the complete sample after the infiltration. The sample was characterized using a lensed fibre fixed on a motorized XYZ stage to couple light from a tuneable laser into the input waveguide. An infrared (IR) camera was used to image the output waveguide at right angle to the input waveguide as photonic crystals were used to reflect the light at right angles.

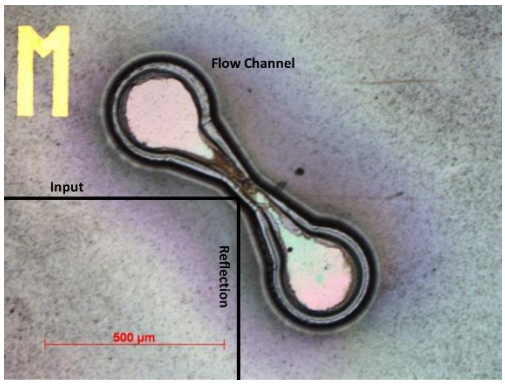

Figure 5-11: SEM image of the fabricated sample after the sphere deposition. It should be noticed that the waveguide is marked with black lines to make them prominent.

A polariser was used at the input to control the polarisation state of the incident light as the structures were designed to strongly reflect only TE polarised light. The camera was focused on the edge of the chip to observe the light coupling to the output waveguide. Wavelength of the tuneable laser was changed over the complete span (1460 nm – 1620 nm) of the tuneable laser with an increment of 10 nm and output spot was captured. The captured images for different input wavelengths are shown in Figure 5-12. It can be noticed that a spot emerges for a wavelength of 1480 nm at a position where the waveguide is terminating on the edge of the chip. This spot gets brighter with increasing wavelength up to 1580 nm. The intensity of the spot decreases after 1580 nm showing that the peak of the reflection is situated at 1580 nm wavelength. It should be mentioned here that intensity of the tuneable laser also follows the same trend i.e. low power at the edges and maximum power around 1550 nm. This cannot be concluded from these measurements that this change in intensity is due to the photonic crystals. The polarization of the incident light was changed to show that a relatively stronger spot was observed for one of the orthogonal polarizations only.

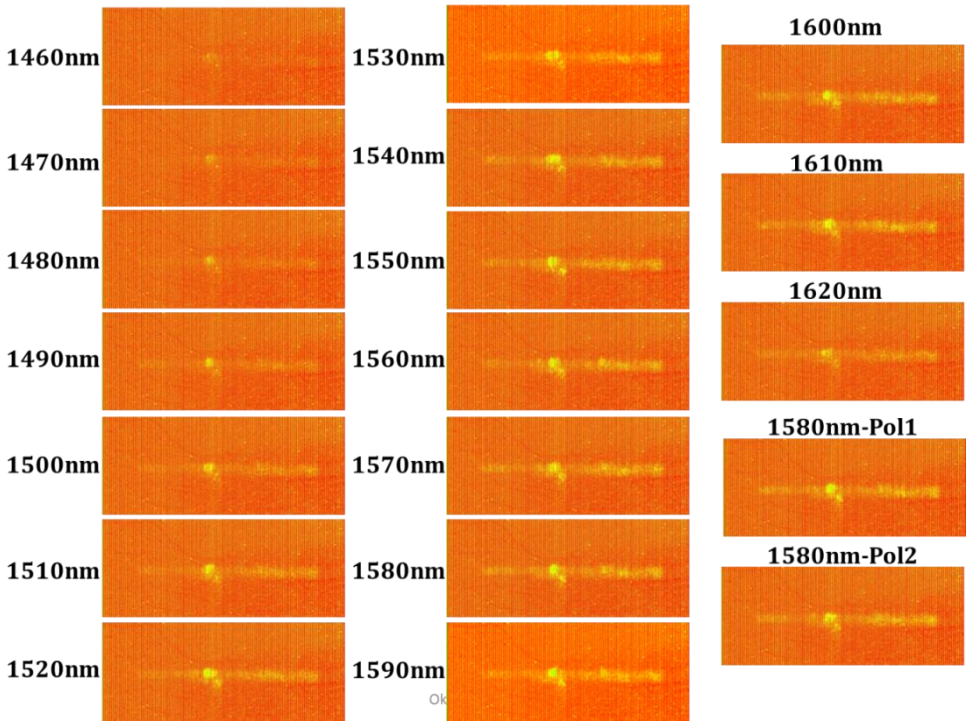

Figure 5-12: Images captured using the IR camera focused at the edge of an integrated sample. The spot in the middle of the chip shows the reflected light. It can be noticed that intensity of the spot decreases for one of the orthogonal polarisation confirming that photonic crystal is reflecting.

To conclude this section, sharp in-plane bends for polymer waveguides are experimentally demonstrated using TiO_2/SiO_2 core-shell FCC (001) structures. The efficiency of these bends is very low due to the variation in size and shape of core-shell particles which led to variation from FCC (001) orientation at some of the places. The performance can be improved by addressing the synthesis and stacking methods.

5.2 Inverted opal as low index substrate

The use of inverted-opal structures as low index under cladding for the polymer waveguide core is discussed in this section. As explained earlier, a substrate with refractive index value comparable to air is desired for air to act as upper cladding of a polymer waveguide. The fabrication and characterization of polymer waveguides on a honeycomb like structure is demonstrated here. The honeycomb like structure lying underneath the waveguide was fabricated by removing the PMMA spheres from a co-crystallised PMMA-SiO_2 structure. Fabricated waveguides were optically characterised to experimentally demonstrate an air cladded polymer waveguide.

Co-crystallised colloidal poly methyl methacrylate (PMMA) and silica thin opaline films were deposited onto silicon wafer substrates using 368 nm diameter PMMA spheres and hydrolysed silica from a tetraethyl orthosilicate (TEOS) precursor solution by a co-assembly method [7-10]. The fabricated samples are shown in Figure 5-13.

(a)

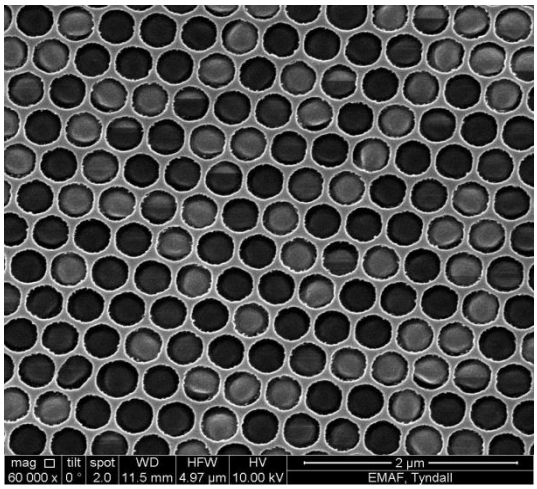

(b)

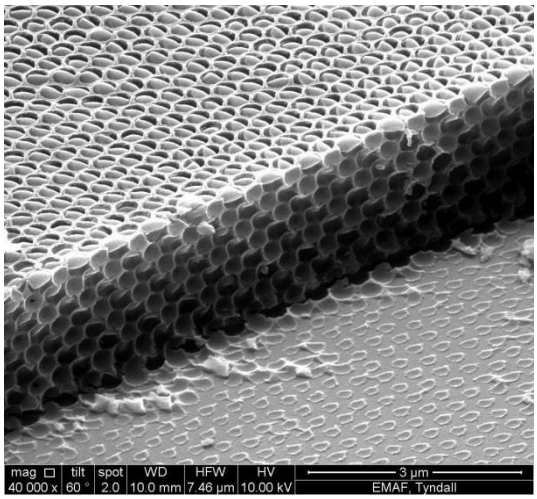

Figure 5-13: Scanning Electron Microscope (SEM) images of (a) co-crystallised PMMA-SiO2 film deposited on silicon substrate on which the polyimide was deposited for the waveguide, (b) the edge of the co-crystallised film. (It should be noted that the PMMA spheres are readily shrunk in the SEM beam).

The reflection response of the deposited 368 nm PMMA spheres co-crystallized structure was measured at an angle of 10° to the normal in order to observe the Bragg reflections. Light from a white light source (Ocean Optics HL2000) was collimated and incident on the co-crystallised region. The reflected light was collected and coupled to a spectrometer (Ocean Optics USB4000) in order to measure the reflecting wavelengths. A weak Bragg reflectance peak was measured at a wavelength of 809 nm, Figure 5-14. The effective refractive index of the sample was measured to be 1.44 by using angle resolved spectroscopy of the Bragg peak [11]. The low intensity of this reflection was due to the small refractive index contrast between PMMA spheres and the silica backbone. A

PMMA opal structure was also prepared using the 368 nm PMMA spheres in order to calculate the refractive index of the PMMA spheres. Reflection measurements from this PMMA opal structure displayed a Bragg peak at 811 nm. The effective refractive index of the PMMA opal was measured to be 1.34 from which the refractive index of the PMMA spheres was calculated to be 1.44, which is very similar to that of silica. The small refractive index contrast between the PMMA spheres and the silica backbone explains the weak Bragg peak at 809 nm observed for the co-crystallized sample.

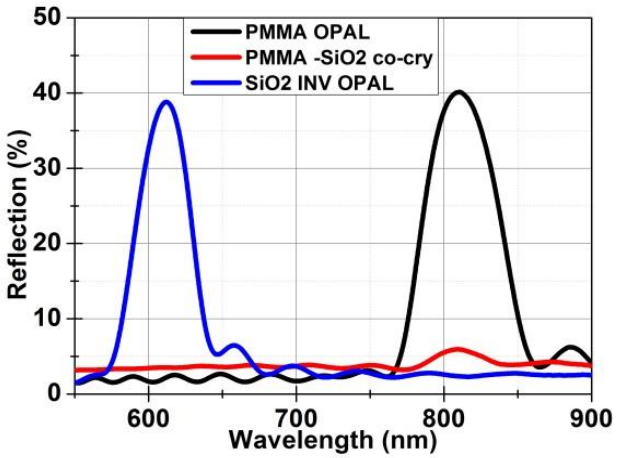

Figure 5-14: Measured reflection at 10° to the surface normal for PMMA opal, PMMA-SiO_2 co-crystallised and SiO_2 inverted opal structures.

A flexible micro-mold of poly-dimethylsiloxane (PDMS) was produced by replication of a master mold on a silicon wafer. The master mold had 10 µm wide and 4.7 µm deep waveguides at a spacing of 50 µm. The master mold was fabricated onto the silicon wafer by standard photolithography methods. The PDMS micro-molds were made from a PDMS elastomer kit (Dow Corning Sylgard 184). The base-to-catalyst mixing ratio from the PDMS kit was 10:1. The mixture was poured over the silicon master mold and degassed in a vacuum chamber for 20 minutes, and then cured at 60°C overnight. The PDMS micro-mold was then peeled from the master mold.

Prior to infiltration of the capillary lines in the micro-mold, the PDMS mold and the co-crystallised PMMA-silica film were cleaned in an air plasma for 5 minutes. A small droplet of Fuji Film polyimide adhesive having a refractive index of 1.8, Durimide 112A [12], was deposited onto the PMMA-silica film and pressure applied. The pressure was

maintained while the substrate and mold was placed into a vacuum chamber at 0.1 MPa for 1 hour. Upon removal from the vacuum the Durimide 112A was soft-baked at 135°C for approximately 90 seconds, according with the manufacturers' guidelines. After curing, chloroform was used, both to swell the PDMS mold to release it from the Durimide MIMIC lines, and secondly to remove the PMMA spheres, thus leaving behind Durimide capillary lines on top of an inverted silica opal structure, Figure 5-15.

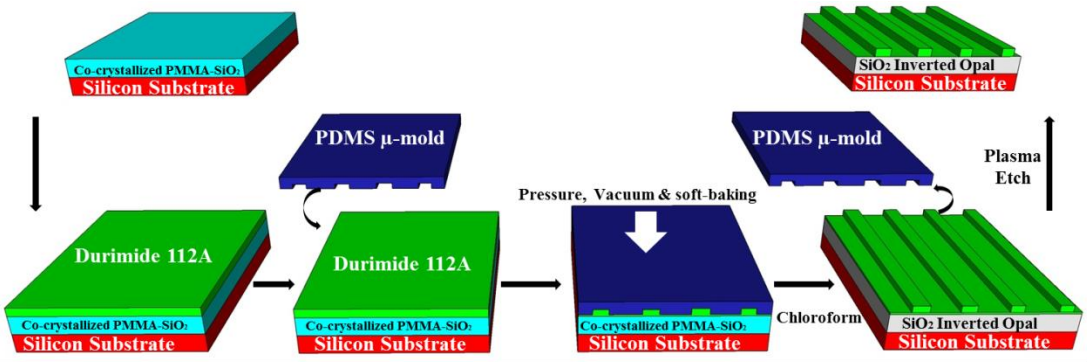

Figure 5-15: Schematic of the fabrication process: Firstly a co-crystallized PMMA-SiO_2 film is deposited on a silicon substrate to act as an under-cladding for the polyimide waveguides. The waveguides are made by depositing Durimide 112A and printing a prepared PDMS mold under vacuum. Chloroform is used after soft-baking the Durimide to swell and release the PDMS mold and also remove the PMMA spheres from the underlying co-crystallized film. This results in a low refractive index SiO_2 inverted opal beneath the Durimide waveguides. An oxygen plasma is used to thin the residual layer. The plasma also aids the removal of any retained PMMA spheres.

A residual layer (1.66 µm thick) of Duramide remained adjacent to the waveguides after the fabrication. This residual layer acts as a cover on the co-crystallized PMMA-silica film and can impede the complete removal of the PMMA spheres. Simulations were performed to find out the effect of this residual layer on the waveguide mode. The calculated fundamental mode for the fabricated waveguide is shown in Figure 5-16(a). Calculations show that the waveguide can accommodate a 2nd order transverse mode as shown in Figure 5-16(b). The height of the waveguide increased due to the residual layer leading to the excitation of the 2nd order mode. Calculations show that a global etch-back of the residual layer will result in a pure single mode waveguide. The calculated mode of the waveguide after etching of the residual layer is shown in Figure 5-16(c). An oxygen plasma was used to remove the residual layer. This global etch back also removed any

remaining PMMA spheres. The waveguide sample is shown in Figure 5-16(d, e) where the residual layer has been etched leaving a waveguide with a height of almost 3.7 µm.

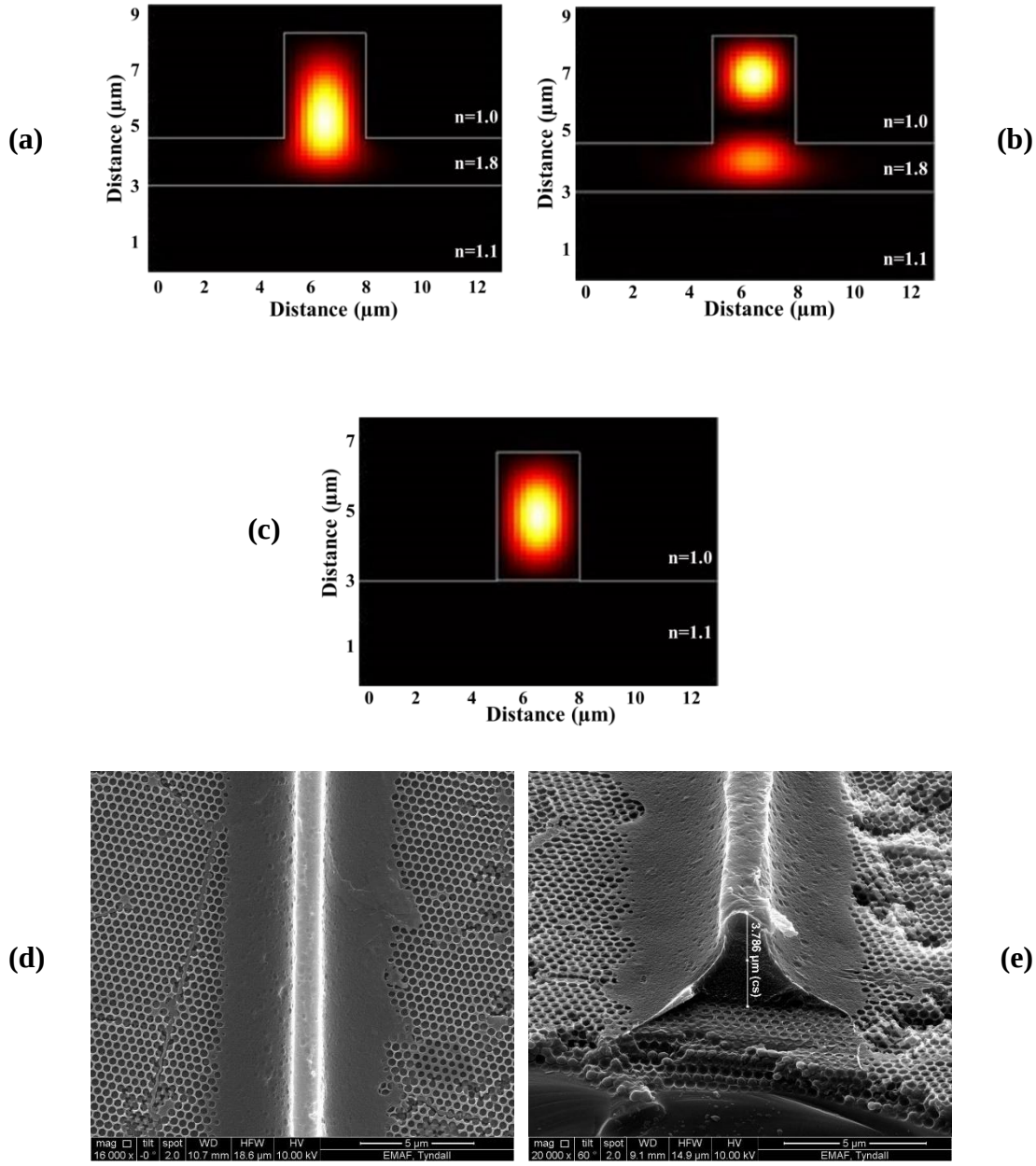

Figure 5-16: (a) Calculated fundamental mode for the waveguide with a residual layer. (b) The higher order mode that can be excited in the waveguide with a resiudal layer. (c) Calculations show that the waveguide is a single moded upon removal of the residual layer. (d) SEM image of top view of the waveguide after oxygen plasma treatment. (e) SEM image of edge of the waveguide of ~3.7 µm in height.

The inverted photonic crystal structure lying beneath the fabricated waveguides now acts as a low refractive index material. The resonance wavelength of the underlying PC was investigated by measuring the spectral reflection at an angle of 10° to the normal from the region where the waveguides were absent. Reflection measurements reveal a Bragg peak at 612 nm with a Full Width Half Maximum (FWHM) of 41 nm as shown in Figure 5-14. The refractive index of the inverted structure was calculated to be 1.01. The presence of a Bragg peak at around 600 nm shows that inverted crystal will act as a low refractive index substrate and will not affect the spectral propagation through the waveguide at telecommunications wavelengths.

The transmission responses of the plasma treated waveguides were measured using a fibre-coupled super continuum light source from Fianium covering the E, S, C and L bands of the communication wavelengths (1300-1600nm). Single mode lensed fibres were used to couple to the input and output waveguides of the fabricated waveguides and the power maximized in order to measure the transmitted powers. The output fibre was coupled to an Optical Spectrum Analyser (OSA) in order to measure the spectral response of the waveguide. Transmission spectra for both TE and TM polarizations of the incident light were measured Figure 5-17(a). A loss of 7 dB was measured for a waveguide of 1 mm length for both polarizations. This measured loss includes the facet coupling losses and the material losses. The Fabry-Perot resonances from the multiple passes through the waveguide due to the facet reflections are shown in Figure 5-17(b). The calculated cavity length associated with these resonances is in agreement with the 1 mm waveguide length. The mode profile of the waveguide was measured by scanning the output fiber in horizontal and vertical directions, Figure 5-17(c). This shows that waveguide was guiding with a single spatial mode as expected from the simulation.

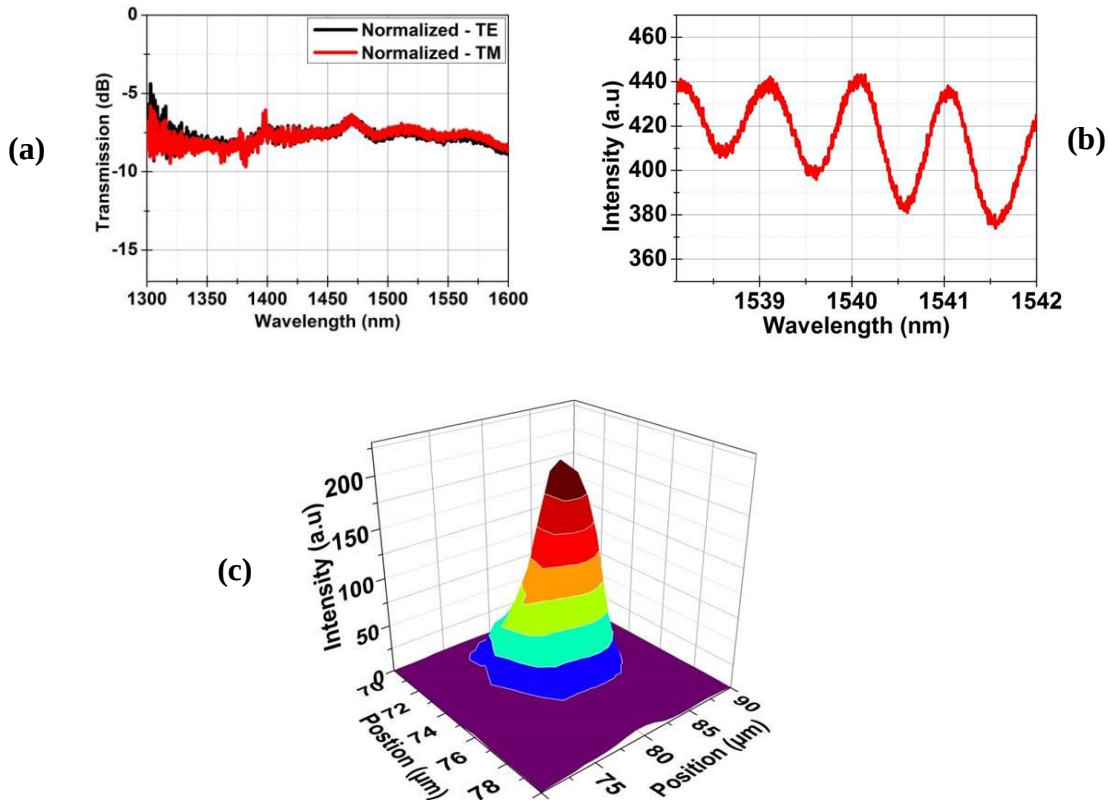

Figure 5-17: (a) Measured transmission responses for both TE and TM polarizations of light. Measurements show broadband transmission with a a loss of 7 dB/mm. This loss also includes the facet coupling losses. (b) Measured Fabry-Perot resonances for the fabricated waveguides. The calculated lengths corresponding to these resonances are in agreement with the actual waveguide lengths. (c) Measured output profile showing a fundamental spatial mode.

To conclude the inverted opal section, a functioning air-clad polymer based single mode waveguide fabricated on an inverted photonic crystal is experimentally demonstrated. The loss across the telecommunications wavelength band for this initial structure was measured to be 7 dB for 1 mm length including the facet losses. Wavelength dependent waveguides for sensing applications can be obtained by designing the underlying photonic crystal to be resonant at the operating wavelengths. This approach enables the fabrication of very compact polymer waveguide circuits.

5.3 Conclusions and discussion

To conclude, sharp bends for polymer waveguides and air cladded waveguides are experimentally demonstrated using three dimensional photonic crystals. It is found that FCC (001) stacking can be achieved by stacking of spheres on the seed layer. The spheres must have uniform size/shape and the pitch of the seed layer should match the diameter of the spheres for good stacking. As it is difficult to synthesise TiO_2/SiO_2 core shell spheres having uniform size and shape so demonstrated efficiencies of the right angle bends are poor. The integration of colloidal crystals with polymer waveguides is itself a difficult task as a small variation in stacking results in a drastic reduction in reflections. The efficiencies can be improved by addressing the synthesis and stacking of the core-shell particles. At the moment this way of achieving sharp bends is not so mature that it may be adopted for achieving of reliable sharp bends.

Functioning of the polymer waveguides on the inverted opal structure is demonstrated. The waveguides were fabricated by MIMIC using Durimide 112A as waveguide material. The material loss of Durimide 112A around telecom wavelengths was unknown and the material was never reported to be used for waveguiding. It was good to demonstrate the working of waveguides but I believe lithography on SU8 as explained in chapter 3 would have resulted in better waveguides. SU8 waveguide were planned as the next step but could not be fabricated due to the lack of time.

The underlying inverted opal structure was acting as a low index material only as the resonance of the crystals was designed to be at smaller wavelengths. The waveguide can be made resonant by designing the underlying structure for resonance around the waveguide operating wavelengths. This will result in a resonance in the transmission response similar to the one demonstrated for waveguide coupled BSW in the previous chapter. This photonic crystal based resonant waveguide can be used as a sensor for liquids and small analytes capable of infiltrating the pores. Designing of photonic crystal for resonance around 1500 nm wavelengths will require larger spheres which will result in a bumpy top surface of the crystal. This bumpy surface may enhance scattering losses through the waveguide as the bottom surface of the waveguide will not be flat. However, functioning waveguides fabricated on top of the inverted opal crystals are demonstrated

and can be used as size selective sensors if designed for resonance around the waveguide operating wavelengths.

5.4 References

[1] A. Mihi, M. Ocana, H. Miquez, “Oriented Colloidal-Crystal Thin Films by Spin-Coating Microspheres Dispersed in Volatile Media,” Adv. Materials 18, p.2244-2249 (2006).

[2] H. Yang and P. Jiang, “Large-Scale Colloidal Self-Assembly by Doctor Blade Coating,” Langmuir 26, p.13173-13182, (2010).

[3] Y. L. Wu, “Control over Colloidal Crystallization by Shear and Electric Fields,” PhD Thesis, UtrechtUniversity, (2007).

[4] A. van Blaaderen, R. Ruel, and P. Wilzius, “Template Directed Colloidal Crystallization,” Nature 385, 321-324(1997).

[5] H. Giesche, J. Eur. Ceram. Soc., 14(3), 189-204 (1994)

[6] H. Giesche, J. Eur. Ceram. Soc., 14(3), 205-214 (1994)

[7] Kassim S., Padmanabhan S., McGrath J., Pemble M., Applied Mechanics and Materials 2015, 699, 318-324

[8] S. C. Padmanabhan, K. Linehan, S. O'Brien, S. Kassim, H. Doyle, I. M. Poyey, M. Schmidt, M. E. Pemble, Journal of Materials Chemistry C 2014, 2, 1675-1682.

[9] B. Hatton, L. Mishchenko, S. Davis, K. H. Sandhage, J. Aizenberg, Proceedings of the National Academy of Sciences of the United States of America 2010, 107, 10354-10359.

[10] L. K. Wang and X. S. Zhao, J. Phys. Chem. C 2007, 111, 8538-8542.

[11] S. C. Padmanabhan, J. McGrath, M. Bardosova, M. E. Pemble, Journal of Materials Chemistry 2012, 22, 11978-11987.

[12] Durimide 112A by Fujifilm [Online] Available: https://www.fujifilmusa.com/shared/bin/Durimide%20100_US12.pdf

CHAPTER 6

Summary and Future Work

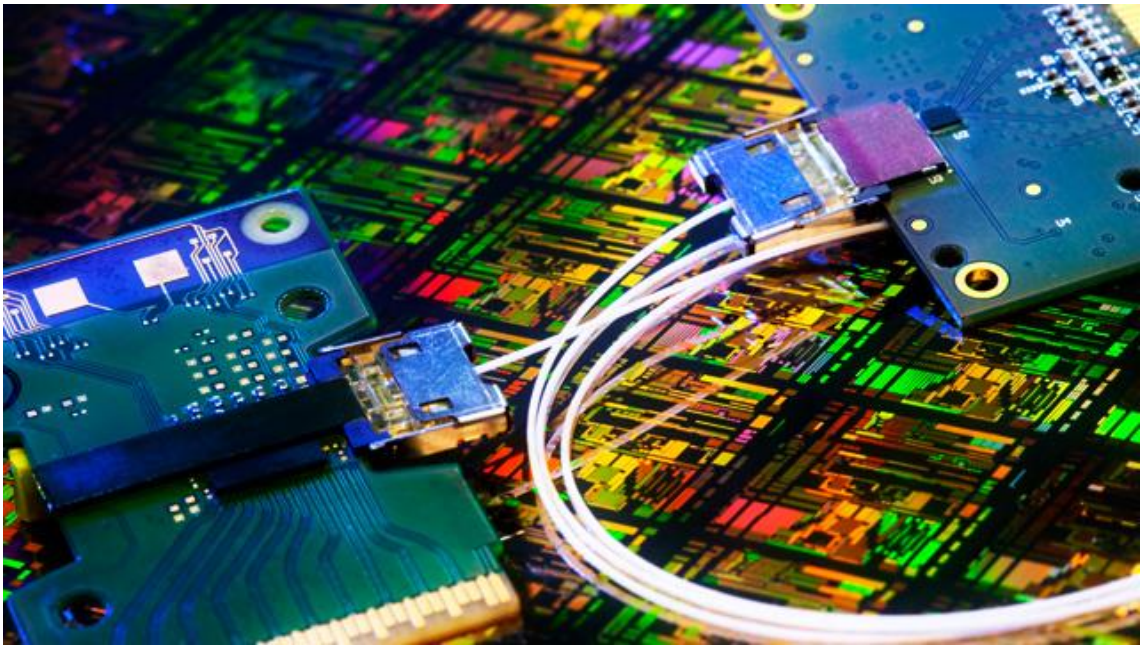

6 Summary and Future Work

In this chapter, the research work presented in this thesis is summarised and major conclusions are drawn. The future possibilities of the research work are also discussed.

6.1 Summary

The behaviour of light in a medium is dependent on the refractive index of that medium. An optical waveguide guiding light from one place to another is the simplest optical structure taking advantage of the refractive index contrast between the core and the cladding. The working principle of an optical waveguide and different guided modes were discussed in the introduction chapter. After discussing the waveguides, more complex structures using the periodic modulation of the refractive index inside a medium were discussed. The structures using the periodic modulation are called photonic crystals. The working principles of one, two and three dimensional photonic crystals were explained to provide the essential knowledge required to understand the work presented in the thesis.

In chapter 2, the modulation of refractive index in one dimension was used to introduce Bloch Surface Waves (BSW) based sensors. By presenting structures from the literature, it was shown that BSW sensors could be designed for both TE and TM polarised light in contrast to the SPR sensors which are only TM polarised. It was demonstrated that the number of dielectric layers could be reduced by increasing the refractive index contrast. A sensing surface using only a single pair of high index contrast layers was experimentally demonstrated. This was the first demonstration of a BSW-like sensor using only a single pair of high and low index layers. The measured sensitivity (900 nm/RIU) for the high index contrast sensor was compared to the earlier reported BSW sensors to show comparable sensitivities. The excited mode was compared with the modes of multilayer BSW, SPR and broadband SOI waveguide to show that the excited mode was BSW-like resonant mode. It was demonstrated using simulations that the concept could also be implemented on the silicon on insulator (SOI) platform at 1550 nm resulting into sharper resonances with better sensitivities (1950 nm/RIU). The implementation of the sensing surface on SOI can lead to tune ability of the surface waves by doping the

silicon. Furthermore, on-chip sensing can be achieved by depositing the designed dielectric layers on a polymer waveguide eliminating the prisms used for the Kretschmann-Raether (K-R) excitation.

In chapter 3, on-chip BSW resonances were experimentally demonstrated by depositing dielectric layers on SU8 based waveguides. Designed thicknesses of silicon (70 nm) and silica (676 nm) were deposited on the top surface of the SU8 waveguide only to demonstrate TM polarised resonance around 820 nm wavelengths. The shift in the resonance was measured to be 100 nm between water and air above the surface showing a sensitivity of 300 nm/RIU. The demonstrated sensitivity was one third of the earlier demonstrated sensitivity (900 nm/RIU) using K-R configuration. This was the first on-chip demonstration using waveguides and sensitivity will improve with optimisation of the design, fabrication and measurement methods. The resonance was then designed and fabricated for operation around telecom wavelengths. Dielectric layers were deposited on three sides of a SU8 waveguide to obtain resonances for both TE and TM polarised light. As expected, resonances were measured for both TE and TM polarised light. There are many possibilities for different designs that can be implemented using this waveguide coupled approach. For example, power splitters and MMI structures can be used to implement on-chip assays which can measure multiple samples at the same time.

In chapter 4, single and multilevel polymer waveguides were studied. ORMOCER based 5 µm x 5 µm waveguides with an index contrast of 0.6% between the core and the cladding were fabricated using nano-imprint lithography (NIL). It was experimentally demonstrated that the bending radius should at-least be 8 mm for negligible transmission losses because of the small refractive index contrast ($\Delta n = 0.009$) between the core and cladding. Sharper bends can be achieved by increasing the refractive index contrast. Passive optical components such as directional couplers, multimode interference devices (MMI) and power splitters were demonstrated. Directional couplers were found to be comparatively more sensitive to changes in refractive index contrast and side wall angles than MMI. For a directional coupler, an increase in side wall angle reduces the coupling gap between the waveguides resulting in shorter coupling lengths. On the other hand, an increase in the index contrast results in longer coupling lengths as the modes are tightly confined inside the cores. After the demonstration of the in-plane passive devices, novel

multilevel components were designed and implemented. An ‘optical via’ for vertical coupling of light from one optical to another was demonstrated for the first time using NIL patterning. The thickness of the cladding layer separating the optical planes in the vertical direction should be uniform as an increase/decrease in thickness results in larger/smaller coupling gaps. This variation in coupling gaps over a chip would lead to optical vias with different up-coupling efficiencies. A 1 x 4 2D optical port to spatially distribute the light over two optical planes was experimentally demonstrated for the first time using an in-plane splitter and multi-plane directional couplers. The 1 x 4 2D optical port was very sensitive to variations in thickness of cladding layer separating the optical planes. A variation in thickness results in power imbalance between the ports.

In chapter 5, the use of refractive index modulation in all three dimensions was investigated and applied to sharp bends in polymer waveguides and to demonstrate air cladded polymer waveguides. Opal photonic crystal structures were placed at 45° to the waveguide core to achieve bending of light at sharp angles. As the crystals were integrated with polymer waveguides having an upper cladding of polymer, it was necessary to use core-shell particles with high index TiO_2 cores inside SiO_2 shell to achieve an acceptable index contrast between the TiO_2 core and the background cladding polymer. Simulations showed that FCC (001) could result in better reflections at sharp angles than FCC (111). The underlying substrate was patterned to achieve the FCC (001) stacking of spheres. Core-shell particles were synthesised, stacked and integrated to the polymer waveguides to experimentally demonstrate sharp polymer waveguide bends. The reflection efficiencies were not good due to the variation in the size and shape of the core-shell particles. It was found that sharp bends using core-shell photonic crystals is not a feasible option. An inverted opal crystal was used as the underlying cladding to demonstrate air cladded polymer waveguide. Air cladding results in large index contrast ($\Delta n = 0.8$) and can be used to realise sharper bends. Waveguides were fabricated on the co-crystallised PMMA-SiO_2 crystals. PMMA spheres were removed after the fabrication of the waveguides to get a honey comb like inverted opal structure lying underneath the waveguide. The fabricated waveguides were experimentally demonstrated to show broadband transmission. These air suspended waveguides with inverted photonic crystal structures underneath can be used as sensors if the underlying structure is designed for

resonance around the operating wavelength. Small molecules or liquid will infiltrate the inverted opal structure and shift the resonance.

To conclude, the roles of the refractive index contrast and modulation were explored and used for sensing and guiding purposes. The key achievements in this work have been:

1. Design and implementation of the first single pair BSW-like sensing surface using silicon and silica.
2. Design and implementation of the waveguide coupled BSW sensors for the first time to achieve on-chip sensing using end-fire coupling. The on-chip resonances could be excited for both TE and TM polarised light for the same waveguide.
3. Implementation and detailed analysis of in-plane polymer waveguides and passive optical devices. An ‘optical via’ for vertical coupling of light from one optical plane to another was designed and implemented for the first time using NIL.
4. Design and implementation of a novel 1 x 4 2D port for spatial distribution of input light over multiple optical planes.
5. Understanding and mapping of different reflecting planes of a face centred cubic (FCC) crystal.
6. Demonstration of effectively air suspended polymer waveguides which can be used for sensing and compact waveguiding.

6.2 Future possible work

Excitation of waveguide coupled resonances using end-fire coupling opens up a new field of BSW based on-chip sensing. A range of different waveguide structures can be implemented. The performance of the first demonstrated waveguide coupled sensor can be enhanced by design optimisation. This will include investigation of the underlying waveguide modes and more careful design of the dielectric layers. The variation in thicknesses of the dielectric layers on the top and side surfaces will also be taken into consideration. Some initial measurements have shown that sensitivities around 900 nm/RIU can be achieved which are comparable to K-R coupled BSW sensors.

Structures capable of detecting multiple analytes at the same time can be designed and implemented using different waveguide based structures. As power splitters and multimode interference devices (MMI) were discussed in chapter 4 so I present two possibilities using these structures. The proposed structures are shown in Figure 6-1 below. The sensor with dielectric layers deposited on arms of the splitter can be used to detect two different analytes, Figure 6-1(a). The power from the source is divided into half and each arm of the splitter is used to detect a particular analyte. Different thicknesses of dielectric layers can also be deposited on the arm to have two different resonances. 1 x 3 MMI splitting the input power into three equal parts can be used to detect three different analytes. The dielectric layers will be deposited on all output waveguides. Different MMIs and splitters can be used for different applications.

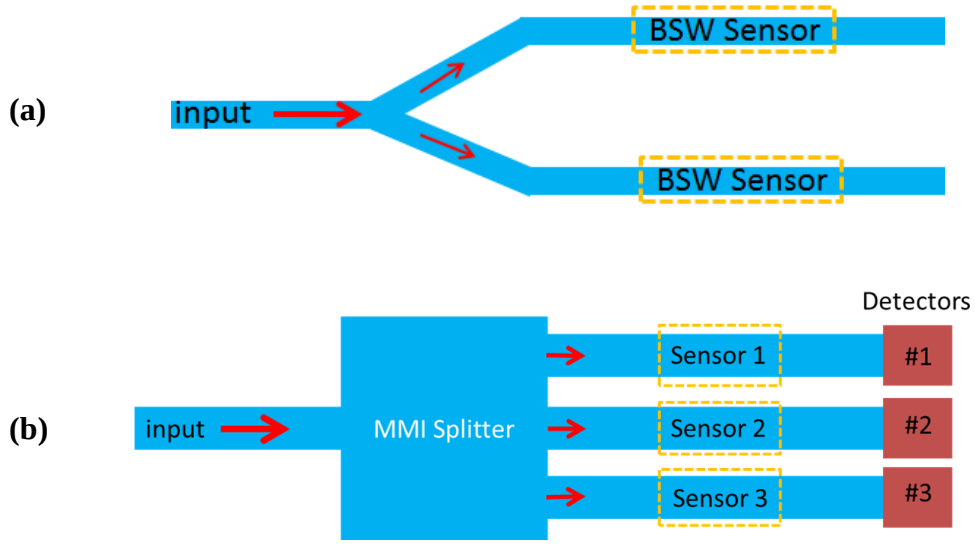

Figure 6-1: (a) Proposed sensor using Y-splitter for detection of two different analytes. Designed dielectric layers will be deposited on output waveguides. The resonance will be measured in the transmission using detectors. (b) Proposed sensor using 1 x 3 MMI for detection of three different analytes at the same time.

As discussed in chapter 3, designed dielectric layers can also be deposited on the glass substrate before the fabrication of waveguides to have a reference resonance in the transmission response. This resonance will not shift with change of environment and will help referencing the shift in resonance.

Polymer waveguide on inverted opal crystals explained in chapter 5 can be implemented for size selective sensing. The underlying photonic crystal can be designed

for resonance around the transmitting wavelengths of the waveguides. The resonance of the crystal will be reflected by a signature (dip/peak) in the transmission of the polymer waveguide. The analytes smaller than the inverted crystal pores will infiltrate the crystal and will shift the resonance of the underlying crystal. This shift in resonance will be reflected in the transmission of the waveguide. SU8 waveguides could be fabricated on the co-crystallised structures using lithography and spheres removed after the fabrication of waveguides. SU8 is more suitable for waveguiding applications than polyimide and better quality waveguides can be fabricated using lithography.

Appendix A

BSW Calculation code - Lumerical

```
########################################################################
# scriptfile: sp_film_resonance.lsf
# This file calculates the reflection spectrum for
# an SPR simulation using Bloch boundary conditions.
#
# Copyright 2010, Lumerical Solutions, Inc.
########################################################################
runsweep;
run;
theta = pinch(getsweepdata("sweep", "source_angle")*pi/180);
R = getsweepdata("sweep", "R");
T = getsweepdata("sweep", "T");
E2 = pinch(getsweepdata("sweep","E2"));
x = getsweepdata("sweep","x");

# find the frequency of the monitor
f = getsweepdata("sweep","f");
# find the frequency of the source
# fsim = getsweepdata("sweep","fsim");
fsim = getdata("source1","f");
lambda = c/f;
```

```
d = 50e-9;

# get the substrate index as run in the fdtd simulation

n1 = getfdtdindex("SiO2 (Glass) - Palik",f,min(fsim),max(fsim));

n2 = getfdtdindex("Ag (Silver) - Palik (0-2um) Copy 1",f,min(fsim),max(fsim));

n3 = 1;

# use stackrt script function to get theoretical reflection

theta1 = theta*180/pi;

n=[n1;n2;n3];

d=[0;d;0];

RT=stackrt(n,d,f,theta1);

Rtheory=RT.Rp;

########################################

# plot the results

plot(theta*180/pi, R, Rtheory,"angle of incidence (degrees)","Reflection","Reflection vs angle");

legend("FDTD","theory");

image(x*1e9,theta*180/pi,E2,"x (nm)","angle of incidence(deg)","|E|^2 at "+num2str(c/f*1e9)+" nm");
```

Appendix B

BSW Calculation Code– MATLAB – Angle scan

```
function []=Anglescan()
clear all
nlow=1.47+0.0005i;
nhigh=3.48+0.0005i;
thetai=50:0.001:67; %angle of incidence (degrees)
lambda=1550; %vacuum wavelength (nm)
hhigh=132;
hlow=1277;
h=[NaN, hlow, hhigh, NaN];
pol=1; %polarization, 1 for p and 0 for s
n=[1.7,nlow,nhigh,1.0]; %refractive index data, NaN for frequency dependence
ds=1.33:0.05:1.37; %film thicknesses
%%%%%%%%%%%%%%%%%%%%%%%%%%%%%%%
for b=1:length(ds)
 %n(13)=ds(b);
for a=1:length(thetai)
[FR(a,b),FT(a,b),FA(a,b)]=Fresnel(lambda,thetai(a),h,n,pol);
end
disp([num2str(b/length(ds)*100) '% done...'])
end
```

```
%plot results:
%figure
hold on
plot(thetai,FR,'c')
xlim([thetai(1),thetai(length(thetai))])
ylim([0 1])
xlabel('incident angle (degrees)')
ylabel('Fresnel coefficient')
title('Fresnel coefficients for transmission (blue), reflection (red) and absorption (green)')
lam=transpose(thetai);
dlmwrite('ref.txt',FR, ';');
dlmwrite('angle.txt',lam, ';');
%%%%%%%%%%%%%%%%%%%%%%
legend('-DynamicLegend',2);
xlabel('Angle (°)','FontSize',30);
ylabel('Reflection','FontSize',30);
title('BSW at 830nm','FontSize',30);
grid on;
box on;
end
%%%%%%%%%%%%%%%%%%%%%%%%
function [FR,FT,FA]=Fresnel(lambda,thetai,h,n,pol)

%Snell's law:
```

```
theta(1)=thetai*pi/180;

for a=1:length(n)-1

theta(a+1)=real(asin(n(a)/n(a+1)*sin(theta(a))))-
1i*abs(imag(asin(n(a)/n(a+1)*sin(theta(a)))));

theta*180/pi

end

%%%%%%%%%%%%%%%%%%%%%%%%%%

%Fresnel coefficients:

if pol==0 %formulas for s polarization

for a=1:length(n)-1

Fr(a)=(n(a)*cos(theta(a))-
n(a+1)*cos(theta(a+1)))/(n(a)*cos(theta(a))+n(a+1)*cos(theta(a+1)));

Ft(a)=2*n(a)*cos(theta(a))/(n(a)*cos(theta(a))+n(a+1)*cos(theta(a+1)));

end

elseif pol==1 %formulas for p polarization

for a=1:length(n)-1

Fr(a)=(n(a)*cos(theta(a+1))-
n(a+1)*cos(theta(a)))/(n(a)*cos(theta(a+1))+n(a+1)*cos(theta(a)));

Ft(a)=2*n(a)*cos(theta(a))/(n(a)*cos(theta(a+1))+n(a+1)*cos(theta(a)));

end

end

%phase shift factors:

for a=1:length(n)-2

delta(a)=2*pi*h(a+1)/lambda*n(a+1)*cos(theta(a+1));

end
```

```
%%%%%%%%%%%%%%%%%%%%%%%%%%%%%%%%
%build up transfer matrix:
M=[1,0;0,1]; %start with unity matrix
for a=1:length(n)-2
M=M*1/Ft(a)*[1,Fr(a);Fr(a),1]*[exp(-1i*delta(a)),0;0,exp(1i*delta(a))];
end
M=M*1/Ft(length(n)-1)*[1,Fr(length(n)-1);Fr(length(n)-1),1];
%%%%%%%%%%%%%%%%%%%%%%%%%%%%%%%%
%total Fresnel coefficients:
Frtot=M(2,1)/M(1,1);
Fttot=1/M(1,1);
%%%%%%%%%%%%%%%%%%%%%%%%%%%%%%%%
%special case of single interface:
if length(n)==2
Frtot=Fr(1);
Fttot=Ft(1);
end
%%%%%%%%%%%%%%%%%%%%%%%%%%%%%%%%
%total Fresnel coefficients in intensity:
FR=(abs(Frtot))^2;
FT=(abs(Fttot))^2*real(n(length(n))*cos(theta(length(n))))/real(n(1)*cos(theta(1)));
FA=1-FR-FT;
end
%%%%%%%%%%%%%%%%%%%%%%%%%%%%%%%%
```

```
function epsilon=Au(lambda)
%analytical formula for gold based on wavelength in nm, fits J&C data:
epsiloninf=1.54;
lambdap=143;
gammap=14500;
A1=1.27;
lambda1=470;
phi1=-pi/4;
gamma1=1900;
A2=1.1;
lambda2=325;
phi2=-pi/4;
gamma2=1060;
%%%%%%%%%%%%%%%%%%%%
%other parameters, worse fit to J&C but seems more accurate often:
%epsiloninf=1.53;
%lambdap=155;
%gammap=17000;
%A1=0.94;
%lambda1=468;
%phi1=-pi/4;
%gamma1=2300;
%A2=1.36;
%lambda2=331;
```

```
%phi2=-pi/4;
%gamma2=940;
%%%%%%%%%%%%%%%%%%%%%%
for a=1:length(lambda)
epsilon(a)=epsiloninf-1/(lambdap^2*(1/lambda(a)^2+1i/(gammap*lambda(a))))...
+A1/lambda1*(exp(phi1*1i)/(1/lambda1-1/lambda(a)-1i/gamma1)+exp(-
phi1*1i)/(1/lambda1+1/lambda(a)+1i/gamma1))...
+A2/lambda2*(exp(phi2*1i)/(1/lambda2-1/lambda(a)-1i/gamma2)+exp(-
phi2*1i)/(1/lambda2+1/lambda(a)+1i/gamma2));
end
end
```

Appendix C

BSW Calculation Code– MATLAB – Wavelength scan

```
function []=wavelengthscan()
%clear all
%close all
%global theta;
%for thickness=1:10:100
nlow=1.47;
nhigh=3.48+0.0586i;
theta=55; %angle of incidence (degrees)
lambdai=1520:0.1:1600; %vacuum wavelength (nm)
%hhigh=thickness;
hhigh=70;
hlow=676;
%hlow=thick;
%hhigh=lambda/(cos(30*pi/180)*4*nhigh)
%hlow=lambda/(cos(79*pi/180)*4*nlow)
%h=[NaN,205,282,205,282,205,282,205,282,205,400,150,NaN]; %film thicknesses in nm, equal in length to n, start and end with NaN
%h=[NaN,121,339,121,339,121,339,121,339,121,339,121,339,121,500,NaN];
h=[NaN,hlow,hhigh,NaN];
pol=1; %polarization, 1 for p and 0 for s
n=[nhigh,nlow,nhigh,1.0]; %refractive index data, NaN for frequency dependence
ds=1.33:0.07:1.373; %film thicknesses
```

```
%%%%%%%%%%%%%%%%%%%%%%%%
for b=1:length(ds)
 %n(4)=ds(b);
for a=1:length(lambdai)
[FR(a,b),FT(a,b),FA(a,b)]=Fresnel(lambdai(a),theta,h,n,pol);
end
disp([num2str(b/length(ds)*100) '% done...'])
end
%%%%%%%%%%%%%%%%%%%%%%%%
lam=transpose(lambdai);
dlmwrite('refBrianwavelengthIPA.txt',FR, ';');
dlmwrite('angleBrianwavelengthIPA.txt',lam, ';');
%%%%%%%%%%%%%%%%%%%%%%%%%%%%
%plot results:
figure
%hold on
%plot(thetai,FT,'c')
%str=sprintf('thickness = %d', thick);
%plot(lambdai,FR,'color',rand(1,3),'DisplayName',str,'linewidth',3)
plot(lambdai,FR,'c','DisplayName','61.19°','linewidth',3)
%plot(thetai,FA,'g')
xlim([lambdai(1),lambdai(length(lambdai))])
ylim([0 1])
legend('-DynamicLegend',2);
```

```
xlabel('Angle (°)','FontSize',40);
ylabel('Reflection','FontSize',40);
%title('BSW at 820nm','FontSize',40);
%title(str)
grid on;
box on;
%end
end
%%%%%%%%%%%%%%%%%%%%%%%%
function [FR,FT,FA]=Fresnel(lambda,thetai,h,n,pol)
%Snell's law:
theta(1)=thetai*pi/180;
for a=1:length(n)-1
theta(a+1)=real(asin(n(a)/n(a+1)*sin(theta(a))))-
1i*abs(imag(asin(n(a)/n(a+1)*sin(theta(a)))));
theta*180/pi
end
%%%%%%%%%%%%%%%%%%%%%%%%
%Fresnel coefficients:
if pol==0 %formulas for s polarization
for a=1:length(n)-1
Fr(a)=(n(a)*cos(theta(a))-
n(a+1)*cos(theta(a+1)))/(n(a)*cos(theta(a))+n(a+1)*cos(theta(a+1)));
Ft(a)=2*n(a)*cos(theta(a))/(n(a)*cos(theta(a))+n(a+1)*cos(theta(a+1)));
end
```

```
elseif pol==1 %formulas for p polarization
for a=1:length(n)-1
Fr(a)=(n(a)*cos(theta(a+1))-
n(a+1)*cos(theta(a)))/(n(a)*cos(theta(a+1))+n(a+1)*cos(theta(a)));
Ft(a)=2*n(a)*cos(theta(a))/(n(a)*cos(theta(a+1))+n(a+1)*cos(theta(a)));
end
end
%%%%%%%%%%%%%%%%%%%%%%%%%%%%%%%%%%%%
%phase shift factors:
for a=1:length(n)-2
delta(a)=2*pi*h(a+1)/lambda*n(a+1)*cos(theta(a+1));
end
%%%%%%%%%%%%%%%%%%%%%%%%%%%%%%%%%%%%
%build up transfer matrix:
M=[1,0;0,1]; %start with unity matrix
for a=1:length(n)-2
M=M*1/Ft(a)*[1,Fr(a);Fr(a),1]*[exp(-1i*delta(a)),0;0,exp(1i*delta(a))];
end
M=M*1/Ft(length(n)-1)*[1,Fr(length(n)-1);Fr(length(n)-1),1];
%%%%%%%%%%%%%%%%%%%%%%%%%%%%%%%%%%%%
%total Fresnel coefficients:
Frtot=M(2,1)/M(1,1);
Fttot=1/M(1,1);
%%%%%%%%%%%%%%%%%%%%%%%%%%%%%%%%%%%%
```

```
%special case of single interface:
if length(n)==2
Frtot=Fr(1);
Fttot=Ft(1);
end
%%%%%%%%%%%%%%%%%%%%%%%%%%
%total Fresnel coefficients in intensity:
FR=(abs(Frtot))^2;
FT=(abs(Fttot))^2*real(n(length(n))*cos(theta(length(n))))/real(n(1)*cos(theta(1)));
FA=1-FR-FT;
end
%%%%%%%%%%%%%%%%%%%%%%%%%%
function epsilon=Au(lambda)
%analytical formula for gold based on wavelength in nm, fits J&C data:
epsiloninf=1.54;
lambdap=143;
gammap=14500;
A1=1.27;
lambda1=470;
phi1=-pi/4;
gamma1=1900;
A2=1.1;
lambda2=325;
phi2=-pi/4;
```

```
gamma2=1060;
%%%%%%%%%%%%%%%%%%%%%%%%%%
for a=1:length(lambda)
epsilon(a)=epsiloninf-1/(lambdap^2*(1/lambda(a)^2+1i/(gammap*lambda(a))))...
+A1/lambda1*(exp(phi1*1i)/(1/lambda1-1/lambda(a)-1i/gamma1)+exp(-
phi1*1i)/(1/lambda1+1/lambda(a)+1i/gamma1))...
+A2/lambda2*(exp(phi2*1i)/(1/lambda2-1/lambda(a)-1i/gamma2)+exp(-
phi2*1i)/(1/lambda2+1/lambda(a)+1i/gamma2));
end
end
```

Appendix D

Multilayer Bragg Reflector Code– MATLAB

```
clear;
angle=0; % Angle in degrees
%%%%%%%%%%%%%%%%%%%%%%%%%%%%%%%%%%%%
for r=1:2:80 % Step r from 1 to 14 in steps of 2
  n(r)=1.5; % Refractive index of high index layer
        h(r)=850/(4*n(r)); % Thickness of high refr. index layer
        %h(r)=500;
   n(r+1)=1.9; % Refractive index of low index layer
        h(r+1)=850/(4*n(r+1)); % Thickness of low refr. index layer
end
h(40)=200;
lambdamin=600;
lambdamax=1200;
lambdastep=0.1;
out=0; %Output option. Reflection for out=1, transmission for out=0.
%********************
nclad=1.0;
neff=nclad*sin((pi/180)*angle);
max=length(n);
for m=1:((lambdamax-lambdamin)/lambdastep)
        lambda=lambdamin+lambdastep*m;
```

```
        lam(m)=lambda;
        k0=2*pi/lambda;
        M0=[1 0;0 1];
        for k=1:max
            test=n(k)*n(k)-neff*neff;
            kappa=k0*sqrt(test);
            arg=kappa*h(k);
            M=[cos(arg) sin(arg)/kappa*i;sin(arg)*kappa*i cos(arg)];
            M1=M0*M;
            M0=M1;
        end
%%%%%%%%%%%%%%%%%%%%%%%%%%%%%%%%%%%%%%%%%%%%%%%%%%%%%%%%%%%%%%%%
        kc=k0*sqrt(nclad*nclad-neff*neff);
        ks=k0*sqrt(nclad*nclad-neff*neff);
        t=2*ks/(ks*M0(1,1)+kc*M0(2,2)+ks*kc*M0(1,2)+M0(2,1));
        r=(ks*M0(1,1)-kc*M0(2,2)+ks*kc*M0(1,2)-M0(2,1))*t/(2*ks);
        T(m)=t*conj(t);
        R(m)=r*conj(r);
end
figure;
if out==0
  plot(lam, T);
  title('Transmission spectrum')
  xlabel('wavelength')
```

```
end
if out==1
   plot(lam, R);
   title('Reflection spectrum')
   xlabel('wavelength')
end
lam=transpose(lam);
R=transpose(R);
T=transpose(T);
axis tight;
```

Appendix E

Truncated FCC Code– Lumerical

```
deleteall;
##########################################################
# Rectangular lattice PC array
# A periodic array of photonic crystals in a rectangular lattice.
#
# Input properties
# z span: height of crystals
# nx, ny: the number of columns and rows
# ax: lattice constant in the x-dir
# ay: lattice constant in the y-dir
# radius: radius of the crystals
# index: index of refraction
# material
#
# Tags: square rectangular lattice pc photonic crystal array
#
# Copyright 2012 Lumerical Solutions Inc
##########################################################

# simplify variable names by removing spaces
z_span = %z span%;

n_rows = ny-1;
n_rows2 = ny-2;
n_cols = nx-1;
n_cols2 = nx-2;
even_flag = 0;
for(k=0:2:nz) {
```

```
for(i=-n_rows/2:n_rows/2) {
for(j=-n_cols/2:n_cols/2) {
if(i<=j){
addsphere;
set("radius",radius);
set("x",(j)*a);
set("y",(i)*a);
set("z",(k)*(sqrt(2)/2)*a);
#set("z span",z_span);
set("material",material);
if(get("material")=="<Object defined dielectric>")
{ set("index",index); }
}}
}
}
for(k=1:2:nz) {
for(i=-n_rows2/2:n_rows2/2) {
for(j=-n_cols2/2:n_cols2/2) {
if(i<=j){
addsphere;
set("radius",radius);
set("x",(j)*a);
set("y",(i)*a);
set("z",(k)*(sqrt(2)/2)*a);
#set("z span",z_span);
set("material",material);
if(get("material")=="<Object defined dielectric>")
{ set("index",index); }
}}
}
}
```

```
selectall;
set("detail",0);
```

Appendix F

Bandstructure calculation code – Lumerical

```
runsweep; # run all sweeps

# get a from model
a = getnamed("::model","a");

# get fs data from the sweeps
sweepname="Gamma-M";
spectrum=getsweepresult(sweepname,"spectrum");
f=c/spectrum.lambda;
fs_all=matrix(length(f),30); # initialize matrix to store fs data in
fs_all(1:length(f),1:10)=spectrum.fs;

sweepname="M-K";
spectrum=getsweepresult(sweepname,"spectrum");
fs_all(1:length(f),11:20)=spectrum.fs;

sweepname="K-Gamma";
spectrum=getsweepresult(sweepname,"spectrum");
fs_all(1:length(f),21:30)=spectrum.fs;

# simple imaging of fs vs k
image(1:30,f,transpose(fs_all),"k (Gamma-M-K-Gamma)","f (Hz)","bandstructure,
logscale","logplot");
image(1:30,f,transpose(fs_all),"k (Gamma-M-K-Gamma)","f (Hz)","bandstructure,
linearscale");
setplot("colorbar min",0);
setplot("colorbar max",max(fs_all)*1e-4);

# plot bandstructure
bandstructure=matrix(num_band,30); # initialize matrix in which to store band
frequency information

# loop over sweep results
for (i=1:30){
#use findpeaks to find num_band number of peaks
temp = findpeaks(fs_all(1:length(f),i),num_band);

#collect data for any peaks that are more than 'tolerance' of the maximum peak (to avoid
minor peaks like sidelobes)
minvalue = fs_all(temp(1),i)*tolerance;
f_band=matrix(num_band);
```

```
for(bandcount = 1:num_band) {
if( fs_all(temp(bandcount),i) > minvalue) {
f_band(bandcount) = f(temp(bandcount));
}
}

f_band_norm = f_band*a/c; # normalize the frequency vector
bandstructure(1:num_band,i)=f_band_norm;
}

bandstructure=transpose(bandstructure);
plot(1:30,bandstructure,"k   (Gamma-M-K-Gamma)","f   (Hz*a/c)","bandstructure","plot
points");
```